

## Letter to the Editor of “Ocean Sciences” regarding manuscript os-2019-77

Dear Professor Huthnance,  
please find attached a revised version of our manuscript “os-2019-77”, which we hope takes into account the remarks formulated by the referees in the previous round of review.

With respect to the previous version, we have made the following changes:

- The title has been slightly amended.
- Dr Peter Sutherland, who contributed during the field work and in the drafting of this second version, has been added as a coauthor.
- The body of the text has been corrected for typos and homogenized, as had been requested by the referees. In this process, most of the text has been amended, but the result is in our opinion much easier to follow.
- The abstract has been rewritten to reflect changes undergone by the rest of the text. We have striven to make our claims and main findings more clearly apparent.
- Section 1 (introduction) has been amended in minor ways.
- Section 2 (theory) has been homogenized and rewritten, with the aim to make it more focused on the particular challenges of near-nadir radar Doppler observations. A subsection pertaining to the overall error budget of the technique, as requested by Ernesto Rodriguez as a referee, has been added.
- Section 3 (description of the field experiment) has been homogenized and rewritten, but did not change substantially.
- Section 4 (results) has been thoroughly rewritten. The text has been clarified in many places. We have re-analysed our data, and managed to explain the major difference observed in the first version between the Ka-band and Ku-band radar measurements. The major instrumental bias present in the Ku-band data in the first version has been corrected in a much better way, and the Ku-band results can now be accounted for by our theory. One finding is also that the directional spread of the sea state seems to bear a stronger influence on the waves-induced contribution to the observed Doppler Frequency Shift than on previous quantities of remote sensing interest (normalized backscattering cross-section). Improving the results of this measurement technique may require developing a better understanding of higher-order statistics of the sea state than previously available and necessary.
- Section 5 (implication for SKIM) and 6 (conclusion and perspectives) have been rewritten accordingly.

One remark we have clearly failed to implement was the request from the Anonymous Referee that the text be substantially shortened. As the text is now more homogeneous in style, clearer and, we hope, much easier to follow, we hope the Referee will forgive this.

Yours sincerely, and on behalf of all the coauthors of manuscript "os-2019-77"

Dr Louis Marié, PhD.

## Point-by-point reply to the report from Reviewer 1

### 1 Summary evaluation.

The SKIM mission is based on the concept of measuring total surface velocity using near-nadir Doppler scatterometry. One of the critical factors in the feasibility of this concept is demonstrating the ability to remove the velocity signature of gravity waves, which, following previous work by Nouguier et al. (2018), can be 20 to 30 times the value of the Stokes drift. This can result in wave induced signatures on the order of 2 m/s to 3 m/s, which are more than an order of magnitude greater than the desired current accuracy.

The main purpose of this paper is to demonstrate that this is feasible using the current model. To show this, the team has deployed two Doppler scatterometers (at Ku and Ka-bands) together with significant in situ resources, including a buoy to obtain surface wave spectra, HF-radar, and two kinds of drifters drogued at different depths. The final results of the paper show a good agreement between the theory of Nouguier et al. at Ka-band (although see detailed comments below), the band proposed for SKIM, but poor agreement at Ku-band and a different frequency dependence between Ka and Ku than predicted by the theory.

The experiment was carefully and thoughtfully designed and the team has made a significant effort to characterize the instruments, especially as regards the mean behavior of the signal. Some discussion has been devoted to the effects of antenna beamwidth at Ku-band leading to contamination of the Doppler signal due to the variation of the radar cross section within the radar footprint. However, given the qualitative discrepancy between theory and observations, additional effort should be devoted to quantifying the measurement errors to show that the Ku-band observations could be compatible with the theory, given feasible measurement uncertainties. Alternatively, physical sources for the discrepancy should be identified for future avenues of study. A more detailed suggestion is given below.

We thank Dr Rodríguez for his thorough reading of our manuscript, for his many insightful suggestions, which we have done our best to implement, and for waiving his anonymity.

We share Dr Rodríguez's opinion that the paper was not clear enough regarding the reasons for the large discrepancies observed between the Ku-band radar measurements and the drifter-derived TSCV estimates. We have tried to address this issue in two ways:

- a first step has been to do a fresh analysis of the Ku-band data, and to correct very carefully the Azimuth Gradient Doppler contribution to the observed Doppler Velocity. This has reduced very significantly the discrepancy between the drifters data and the Ku-band Total Surface Current Velocity vector retrievals, which can now be considered reasonable.
- A second step has been to implement Dr Rodríguez's suggestion of reorganizing some of the material into a formal error budget (restricted to its geometrical factors), which is now contained in the new section 2.3. This error budget clearly shows that the azimuth pointing accuracy required to keep the error on the TSCV retrieval to reasonable levels is far out of reach of KuROS without the special compensation procedure mentioned above (recalling again that this instrument was not originally designed for this type of measurements).

**Overall, the paper has a logical outline. However integration of the different sections into a consistent style and level of detail has not been as successful, leading to some repetition and confusion, at times. The paper would benefit by a final integration to sharpen the presentation into a more uniform manuscript.**

We have thoroughly rewritten the text in order to make it more uniform and easier to follow. As also requested by an Anonymous Referee, we have done our best to remove repetitions to reduce the length of the manuscript.

**In spite of these reservations, I think that the data collected are an important data set that should be in the open literature and recommend its publication, hopefully after some of the more detailed comments below have been addressed. I recommend that the authors consider putting the data in the public domain, so that it can serve to lay the groundwork for work that will strengthen the case for the SKIM mission.**

We thank Dr Rodríguez for this appraisal of our work. Ensuring an open access to the Drift4SKIM dataset will be performed in the course of the IASCO project, funded by ESA.

## **2 Error Quantification**

**Although there is a numerical discussion of various error sources (especially biases due to the antenna pattern and azimuthal variations of backscatter cross section), there is no attempt at deriving an error budget for either of the instruments. This would not be important if the observed measurement scatter were small. However, it is far from small, as can be seen in Figures 12, 13 and 16, where measurement standard deviations varying from 1 m/s to 2 m/s can be observed. Figure 12 is very enlightening about the variation characteristics of the Ka-band measurements, and an equivalent version would have been very useful for Ku-band. For SKIM, it is important to show that not only the**

model predicting the mean behavior is understood, but also that the error performance is understood. Currently, this information is not contained in the paper, but all the data are available to produce this validation.

The error budget should contain, at least:

1) Expected measurement random velocity errors, which can be calculated in a straightforward fashion from the pulse pair correlation.

2) Contributions from pointing errors. For KuROS, the incidence angle is very well constrained by the high range resolution (although platform elevation couples in at shallow angles, as noted by the authors), but this is not the case for KaRADOc, where a single footprint is used. Typical aircraft roll (and, to a lesser extent, pitch) variations will lead to variations in the local incidence angle of up to a few degrees (leading to large errors, if uncorrected) , and it is not clear in the description of the processing how these effects are mitigated.

3) Error bounds on the possible Doppler effects due to uncertainties in the antenna pattern.

4) Error bounds on the expected effects of the  $\sigma_0$  azimuth modulation errors as a function of azimuth, which can be obtained using the wavelength of the resolved waves, shown in Figure 9.

5) Modeling assumptions(see below).

As stated above, we have done our best to implement this suggestion. We have not provided such a fine analysis of the different contributions mentioned, but have at least delineated them, and given their geometrical weighting factors. Clearly, much work remains for further contributions.

**Both radar systems have high PRF to properly sampling the Doppler. Is the contamination due to range ambiguities significant? Has it been considered as a source of error?**

Due to the near-nadir viewing geometry and low flight altitude of KuROS with respect to DopplerScatt, each KuROS pulse can be received and processed before the following pulse is transmitted. Processing the KuROS data is thus comparably easier, and the instrument is not affected by the range ambiguity problem.

Examination of Figure 12 shows passes in the east-west direction have lower levels of variations than those going north-south. In addition, the frequency of variation is higher on the 22nd than on the 24th, but the amplitude of variability is larger on the 24th. What is the reason for this? It does not seem to align with wind or wave directions. In any case, the characteristics of the variations seem

**to be long-wavelength, leading one to suspect either attitude errors or errors due to the changes in the surface field characteristics. Examining the equivalent noise characteristics of the Ku-band data would potentially help in understanding the differences between the two frequencies.**

The data shown in figure 12 have been low-pass filtered to remove the large fast variations due to individual waves. This has now been stated explicitly in the caption. We have checked the long-wavelength variations are not linked in a straightforward way to the plane attitude, and our current opinion is that they are caused by changes in surface-field characteristics. Which can only be briefly mentioned in this already very long article, but will be the subject of further contributions by the Drift4SKIM team.

As regards the difference between the Ka-band and Ku-band Doppler Velocity data, as stated above, our conclusion is that it is caused by a systematic mispointing effect caused by the KuROS antenna radiation diagram.

**One observation is that, comparing the variations in Figure 16 and 13, the level of within track variability is smaller for Ku band than for Ka-band. Thus the lack of agreement with the model is not due to higher random noise (as could be expected from wave  $\sigma_0$  contamination), but through some systematic azimuth dependent effect. One potentially useful exercise is to assume that the azimuth brightness gradient contains additional harmonics to the ones estimated in going from Fig. 16a to 16b. Is it possible to account for the divergence from the model with these higher harmonics? If so, are these excluded by the  $\sigma_0$  observations? Can they be ascribed to systematic coupling that might happen between the antenna pointing and the attitude? If these explanations are not feasible, does this indicate that additional physics needs to be incorporated into the model (at least at Ku-band)?**

Indeed, we agree with Dr Rodríguez that the discrepancy between the Ku-band and Ka-band data was caused by a systematic azimuth-dependent effect. We hope Dr Rodríguez is satisfied with the explanation we propose in the revised version of the text.

### **3 Modeling and retrieval issues**

There seems to be some mixed messages regarding the modeling assumptions. In Nouguier et al. (2018), a Gaussian assumption is made throughout. On the other hand, the authors quote the asymmetry and skewness of the slope distribution (with references to Munk (2008) and Chapron et al. (2002)) in order to explain the upwind/downwind asymmetry in the Ku-band backscatter cross-section (Figure 10), which is not insignificant. In equation 16, the isotropic backscatter curves of Nouguier et al. (2016) are used, but they are multiplied by an azimuthal modulation factor  $F(\phi)$ , which is

**not in the original paper and which does not seem to show up again in the analysis. Was such a factor used? If so, is it related to the azimuthal modulation factor quoted in the azimuth modulation fits quoted (but whose values are never given) in the second paragraph in page 21? If not, where is it coming from? Backscatter data are collected at Ku-band and presented in Figure 10A. Do these backscatter data fit the model in equation 16? If so, are the azimuthal modulations derived from these data for both Ku and Ka? If not, is there a justification for using equation 16 when it does not match the data?**

We agree the original manuscript was definitely obscure on these subjects. We have made a significant effort to clarify all these issues in section 2.2.

**In the Nouguier et al. (2018) paper, there are two models presented: one for range resolved or not range resolved Dopplers. Since KaRADOC is not resolving the waves, I assume that the second model is used. This model contains two parts (equation 15, Nouguier et al. (2018)), one which dominates along the wave direction, and another one which has contributions at other azimuths. In this paper, only one term seems to have been kept (i.e., equation 15, Nouguier et al. (2018)). What is the justification for neglecting the second contribution at other azimuths?**

We have clarified all these issues in section 2.2. As it turned out, the analysis was in practice not based on the equations mentioned by Dr Rodríguez. We confirm we have not attempted to apply the range-resolved formalism of the Nouguier et al (2018) paper to the Drift4SKIM observations. Again, though probably desirable, this probably would have required a lengthy discussion, which would have made the text even more unreasonably long.

**It is well known that non-Gaussian effects will lead to a correlation between the modulation of the slope rms and the location along the wave phase. This effect leads to the EM bias in altimetry, for example. Will the level of modulation consistent with EM bias results lead to a change in the predictions made by the model? Will it lead to an upwind-downwind asymmetry in the Doppler? Can it partially account for the 10-percent adjustment that had to be made to make the model predictions fit the data?**

Though we share Dr Rodríguez's interest in these issues, we have not yet been able to analyze the Drift4SKIM dataset in sufficient depth to identify how we could contribute answers to all these questions.

It is definitely in our plans for the forthcoming years to clarify these issues and assess the impact of non-Gaussian behaviour of the sea state on potential SKIM current retrievals, but this was not feasible in the scope of this necessarily limited first analysis of the dataset.

At present, as stated in the text, our position on this point is that uncertainties on the

directional spread of the sea state are sufficient to explain the 10% discrepancy between the modeled Wave Doppler contribution and the observations.

**In the retrieval of the surface currents, it was assumed that the current in the scene remained constant. However, as shown in Table 2 and Figure 7, there was significant change in the currents due to tidal variations measured by the Trefle buoy. How was this accounted for during the fitting? The HF-radar imager linked to in the paper also show some current gradients in the region: were they observable by the radars? Table 2 also shows significant disagreement between the Trefle buoy velocities and those from the other in situ data. Could you comment on the source of discrepancy?**

Once again, these effects, though interesting, were not sufficiently well resolved during the experiment to lend themselves to a thorough analysis. Our approach has thus been to compare time and space averages of the surface current estimates obtained using the different instruments. This unfortunately tends to degrade the agreement, by leaving as “unexplained discrepancies” effects which could be reduced into “resolved variability” by a more careful analysis. We felt this was however still out of the scope of this first account of the Drift4SKIM experiment.

Regarding the disagreement between the Trèfle and other in-situ velocities in Table 2, we suspect a misunderstanding: the data reported as “buoy ( $U_s$ ,  $V_s$ )” in the table are the Stokes drift components at the center of the “Offshore” area, estimated from the Trèfle buoy IMU data on November 22<sup>nd</sup> and from the closest Spotter buoy on November 24<sup>th</sup>. The figures are indeed markedly different from the drifter velocity data, but are in reasonable agreement with the Stokes drift estimates provided by the WaveWatch3 model.

#### **4 Miscellaneous comments**

**Figure 5 appears with insufficient attribution or description. Part of it comes from Nouguier et al. (2016), but there are additional subpanels whose provenance should be clarified.**

Details for each panel have now been added to the caption:

**The term  $mss_{shape}$  is introduced with just a reference to Nouguier et al 2016. To make things easier for the reader, it should be clarified that it is the apparent rms slope obtained by fitting the backscatter curves.**

Indeed, the  $mss_{shape}$  is a parameter that is a function of the radar wavelength and is obtained from the variation of backscatter with azimuth. This is now clarified in the discussion of equations (16) and (17).



**In page 32, there is a statement made about the equivalent depth of the measurements from near-nadir Doppler scatterometry. However, no such derivation is presented in the papers referenced. It would be useful to the community if this statement were backed with a calculation for the two wind speeds (perhaps as an appendix)**

We appreciate the importance of this comment. However, given the length and complexity of the present paper we have removed the discussion of this point.

We are working on a short note giving the details of the theoretical and expected current measurements in the presence of a vertical shear (Nouguier et al., in prep).

## Point-by-point reply to the report from Reviewer 2

**Review on the paper “Measuring ocean surface velocities with the KuROS and KaRADOC airborne near-nadir Doppler radars: a multi-scale analysis in preparation of the SKIM mission” by L. Marié et al.**

This paper presents the technique and examples of current velocity measurements from an airborne platform carrying two radars. The data acquisition was performed at a site located off the western coast of France where the surface currents are continuously monitored by two HF radars. Surface drifters were deployed for validation of airborne velocity measurements. The paper provides a detailed discussion of the experimental setup, measurement technique, errors, and comparison of the velocity data from different sensors.

**I find the paper very deep, well worth publishing, providing very valuable information for developers of radars for velocity measurements from space. All figures are of excellent quality. Congratulations to the authors on a good paper, but an even more impressive field campaign.**

We thank the referee for his/her careful reading of our manuscript, and for taking the time to contribute this positive appraisal of our work to the interactive discussion of the article. We have revised the article to address the issue he/she and the other reviewer had raised. In the following we detail what modifications we have performed in response to his comments.

**However, the paper would benefit from the following changes (not only minor):**

**– The text needs a substantial reduction: 33 pages and 15 pages in Appendix, this is too much. Please make sure authors are happy with this?**

We understand (and share) the concern expressed by the reviewer.

We have done our best to streamline the flow of the paper and tried to make it as easy to read as possible.

The field of Doppler radar oceanography is however fairly new. Presenting the results of the Drift4SKIM campaign in fact also requires presenting a number of concepts that had to be developed during the analysis. We have not been able to reach this dual goal of presenting the data with sufficient background in a pedagogical **and** terse way.

In fact, only section 2.2 can be considered as very strongly inspired by the previous work of Nougquier and collaborators, the rest being fully original. Including this section makes the article a self-contained introduction to the technique for workers from

other fields.

Also, we have kept long appendixes, which make the article a self-contained reference for future work. Some of this work, which would not deserve publication by itself, would otherwise probably be lost.

We hope the reviewer will forgive us for this.

**Many formulas and demonstrations come from the paper of Nouguier et al., 2018 and Rodríguez et al., 2018. The saving is worth it.**

As mentioned above, though the cited articles have been an important source of inspiration, we had to adapt significantly the concepts they developed to the near-nadir observations performed during Drift4SKIM. We have done our best to remove any duplication of these articles and to shorten our text, which admittedly remains long.

**–The text needs a closer proof reading. There are some typos (altitude/attitude in page 39, 40; are/is following the word data within the whole paper, Appendixes/appendices in page 16, ...**

We have thoroughly searched the text for such issues.

**–The main body of the paper requires a number of changes to the text where it appears confused while Appendixes are well written and very clear.**

The main text has been clarified.

**Specific points.**

**Abstract: what is the major finding in this study? Only an estimate of  $C_0$ ? The description of the experiment should be shortened giving the place to the main results.**

In our opinion, there are several findings in this study:

- we have developed a number of concepts necessary for the analysis of Doppler Velocity data collected from a fast-moving platform.
- we provide an experimental check of the fact that the Kirchhoff Approximation electromagnetic model provides good estimates of the wave-induced component of the Doppler Frequency Shift.
- this allows us to provide confirmation of the fact that the norm of this component is weakly variable with respect to environmental variables, and that the direction follows quite closely that of the wind.
- we demonstrate the feasibility of retrieving the Total Surface Current Velocity vector from radar Doppler observations of the sea surface.

**P3 L15 something is wrong with the English of this sentence? The contribution ... of contributions**

The main text has been thoroughly searched for such issues.

**P4 L2 measurement equation. Maybe measurement is not necessary?**

This sentence has been corrected.

**P9 Figure 4 caption: contribute to or contribution to. “to” is missed.**

This sentence has been corrected.

**P10 Some problems with the English in many places.**

**L1-2: the sentence seems not finished.**

**L7: U is the current speed ...**

**L8 wave slope variability? spectrum.**

**L16 While the incidence angle increases ... the backscatter becomes dominated**

**L27,30. eq. 14 contains phi or phi\_s? it is confusing.**

On the basis of the comments from both referees, we have thoroughly rearranged the text of section 2. We have done our best to make that important section clear, easy to read, and syntactically correct.

**P11 L24: something gone wrong in this sentence. ... work was focused in two boxes. Perhaps, work performed in locations matching by two boxes in Figure 6 ...**

We have removed references to “boxes”, and used the word “area” instead in the text.

**P13-P14. The text is very confusing and should be re-written.**

We have done our best to clarify the text of sections 3.1 and 3.2.

**P16 L8. Please check for frequency and remove band if only one frequency is used.**

This sentence has been corrected.

**L12 How to understand the ambiguity of 126 m/s ?**

We have been more explicit in our discussion of ambiguity in section A1.4.

126 m/s is equal to the upper bound of the unambiguous velocity interval at the KuROS wavelength and PRI.

**P17 L8 Consider: observations corresponding to  $\Phi=12^\circ$  are reported.**

This sentence has been corrected.

**P19 L1-4. Please remove repetition in this sentence: 30 seconds**

This sentence has been corrected.

**P21 L12: Consider: Due to the narrower radar beam, the data from Karadoc are easier to interpret than the data from Kuros.**

We have implemented the referee's suggestion.

**P21 L14 and P22 L1-2: something is wrong with the English in these lines.**

This paragraph has been rephrased.

**P23 Figure 13 caption: remove one "blue" and complete the sentence.**

The caption of Figure 13 has been corrected.

**P26 L1 Consider ... spectra estimated from measurements on November 2 ...**

This sentence has been corrected.

**P26 L4 energy is much lower than**

This sentence has been corrected.

**P31 L7 Perhaps: Regarding the radar measurements, ...**

This sentence has been corrected.

**P33 L19-21. This conclusion is confusing and should be re-written**

We have rephrased the conclusion in our revised version, taking into account the comments from the referee as well as the evolution of the text.

## List of changes made to the manuscript

As requested by both referees, the manuscript has been thoroughly rewritten to make it more uniform and easier to read. A point-by-point list of all the modifications would probably fail to convey the intended information. We thus only provide here a list of “macro-changes” performed in response to the referee comments. With respect to the previous version, we have made the following changes:

- The title has been slightly amended.
- Dr Peter Sutherland, who contributed during the field work and in the drafting of this second version, has been added as a coauthor.
- The body of the text has been corrected for typos and homogenized, as had been requested by the referees. In this process, most of the text has been amended, but the result is in our opinion much easier to follow.
- The abstract has been rewritten to reflect changes undergone by the rest of the text. We have striven to make our claims and main findings more clearly apparent.
- Section 1 (introduction) has been amended in minor ways.
- Section 2 (theory) has been homogenized and rewritten, with the aim to make it more focused on the particular challenges of near-nadir radar Doppler observations. A subsection pertaining to the overall error budget of the technique, as requested by Ernesto Rodriguez as a referee, has been added.
- Section 3 (description of the field experiment) has been homogenized and rewritten, but did not change substantially.
- Section 4 (results) has been thoroughly rewritten. The text has been clarified in many places. We have re-analyzed our data, and managed to explain the major difference observed in the first version between the Ka-band and Ku-band radar measurements. The major instrumental bias present in the Ku-band data in the first version has been corrected in a much better way, and the Ku-band results can now be accounted for by the theory. One finding is also that the directional spread of the sea state seems to bear a stronger influence on the waves-induced contribution to the observed Doppler Frequency Shift than on previous quantities of remote sensing interest (such as normalized backscattering cross-section). Improving the results of this measurement technique may require developing a better understanding of higher-order statistics of the sea state than previously available and necessary. The discussion of KuROS data collected at 18° incidence angle, which did not bring in new information, has been removed to shorten the text.
- Sections 5 (implication for SKIM) and 6 (conclusion and perspectives) have been rewritten accordingly.

# Measuring ~~ocean surface velocities~~ Ocean Total Surface Current Velocity with the KuROS and KaRADOC airborne near-nadir Doppler radars: a multi-scale analysis in preparation of the SKIM mission

Louis Marié<sup>1</sup>, Fabrice Collard<sup>2</sup>, Frédéric Nouguier<sup>1</sup>, Lucia Pineau-Guillou<sup>1</sup>, Danièle Hauser<sup>3</sup>, François Boy<sup>4</sup>, Stéphane Méric<sup>5</sup>, Peter Sutherland<sup>1</sup>, Charles Peureux<sup>1</sup>, Goulven Monnier<sup>6</sup>, Bertrand Chapron<sup>1</sup>, Adrien Martin<sup>7</sup>, Pierre Dubois<sup>8</sup>, Craig Donlon<sup>9</sup>, Tania Casal<sup>9</sup>, and Fabrice Ardhuin<sup>1</sup>

<sup>1</sup>Laboratoire d'Océanographie Physique et Spatiale (LOPS), UMR 6523, Univ. Brest, CNRS, Ifremer, IRD, Brest, France

<sup>2</sup>OceanDataLab, Locmaria Plouzané, France

<sup>3</sup>CNRS, Univ. Versailles St Quentin, Sorbonne Université, LATMOS, France

<sup>4</sup>CNES, Toulouse, France

<sup>5</sup>Institut d'Électronique et de Télécommunication de Rennes (IETR), UMR CNRS 6164, Rennes, France

<sup>6</sup>SCALIAN, Rennes, France

<sup>7</sup>NOC, Southampton, UK

<sup>8</sup>CLS, Ramonville St Agne, France

<sup>9</sup>ESA, Noordwijk, The Netherlands

*Correspondence to:* Fabrice Ardhuin (fabrice.ardhuin@univ-brest.fr)

**Abstract.** Surface currents are poorly known over most of the world's oceans. Satellite-borne Doppler Waves and Current Scatterometers (~~DWCS~~) can be used DWaCS are one of the proposed techniques to fill this observation gap. The Sea surface KINematics Multiscale (SKIM) proposal ~~is~~ is the first satellite concept built on a DWCS DWaCS design at near-nadir angles, and ~~now one of the two candidates to become the 9th mission~~ was demonstrated to be technically feasible as part of the European Space Agency Earth Explorer program. ~~As~~ This article describes preliminary results from a field experiment performed in November 2018 off the French Atlantic coast, with sea states representative of the open ocean and a well known tide-dominated current regime, as part of the detailed design and feasibility studies (phase A) ~~funded by ESA, airborne measurements were carried out with both a Ku-Band and a Ka-Band for SKIM. This experiment comprised airborne measurements performed using Ku-band and Ka-band~~ Doppler radars looking at the sea surface at ~~near-nadir incidence~~ near-nadir incidence in a real-aperture mode, i.e. in a geometry and mode similar to that of SKIM. ~~The airborne radar KuROS was deployed to provide, as well as an extensive set of in-situ instruments. The KuROS airborne radar provided~~ simultaneous measurements of the radar backscatter and Doppler velocity, in a side-looking configuration, with an a horizontal resolution of about 5 to 10 m along the line of sight and integrated in the perpendicular direction over the real-aperture 3-dB footprint diameter (about 580 m). The KaRADOC system ~~has, also operating in the side-looking configuration, had~~ a much narrower beam, with a circular footprint only 45 m in diameter.

~~The experiment took place in November~~ Results are reported for two days with contrasting conditions, a strong breeze on 2018 off the French Atlantic coast, with sea states representative of the open ocean and a well known tide-dominated current

regime. The data set is analyzed to explore the contribution of non-geophysical velocities to the measurement and how the geophysical part of the measured velocity combines wave-resolved and wave-averaged scales. We find that the measured Doppler velocity contains a characteristic wave phase speed, called here  $C_0$  that is analogous to the Bragg phase speed of coastal High-Frequency radars that use a grazing measurement geometry, with little variations  $\Delta C$  associated to changes in sea state.

The Ka-band measurements at an incidence of  $12^\circ$  are 10% lower than the theoretical estimate  $C_0 \simeq 2.4$  m/s for typical oceanic conditions defined by a wind speed of 7 m/s and a significant wave height of 2 m. For Ku-band the measured data is 30% lower than the theoretical estimate 2.8 m/s.  $\Delta C$  is of the order of 0.2 m/s (wind speed 11.5 m.s<sup>-1</sup>, Hs 2.6 m), and gentle breeze on 2018/s for a 1 m change in wave height, and cannot be confused with a 1 m/s change in tidal current. The actual measurement of the current velocity from an aircraft at 4 to 18° incidence angle is, however, made difficult by uncertainties on the measurement geometry, which are much reduced in satellite measurements. (wind speed 5.5 m.s<sup>-1</sup>, Hs 1.7 m). The measured line-of-sight velocity signal is analysed to separate a non-geophysical contribution, linked to the aircraft velocity, a geophysical contribution due to the intrinsic motion of surface waves, and the desired surface current contribution. The surface waves contribution is found to be well predicted by Kirchhoff scattering theory using as input parameters in-situ measurements of the directional spectrum of long waves, complemented by the short-waves spectrum of (?). It is found to be closely aligned with the wind direction, with small corrections due to the presence of swell. Its norm is found to be weakly variable with wind speed and sea state, quite stable and close to  $C_0 = 2.0$  m.s<sup>-1</sup> at Ka-band, more variable and close to  $C_0 = 2.4$  m.s<sup>-1</sup> at Ku-band. These values are 10-20% smaller than previous theoretical estimates. The directional spread of the short gravity waves is found to have a marked influence on this surface waves contribution. Overall, the results of this study support the feasibility of near-nadir radar Doppler remote sensing of the ocean TSCV.

*Copyright statement.* The article is distributed under the Creative Commons Attribution 4.0 License.

## 1 Introduction

The ~~total ocean surface current velocity~~ ocean Total Surface Current Velocity (TSCV) is defined as the Lagrangian mean velocity ~~right at the~~ at the instantaneous sea surface, corresponding to an effective mass transport velocity at the surface. The TSCV is currently only reliably measured by High-Frequency (HF) radars ~~for,~~ deployed in some coastal regions. Elsewhere, ~~its available~~ estimates depend on numerical ~~models~~ model outputs, sea level and wind measurements ~~using,~~ and on assumptions such as a balance between surface pressure gradient and the Coriolis force. ~~Similar weaknesses affect the estimates of directional wave statistics. Such~~ The situation is similar regarding Directional wave statistics, which are currently mainly estimated through numerical modeling.



30 ~~These~~ estimates of the TSCV ~~and wave spectrum~~ are not reliable at small scales, particularly so in the tropical ocean ~~(e.g. ??). This limits our understanding of (e.g. ??), and these limitations hamper current efforts to observe and understand the~~ fluxes of heat, freshwater, carbon, plastics, and the coastal impacts of sea states.

Whereas new data on ocean waves ~~is are~~ becoming available with the ~~SWIM instrument on~~ Surface Waves Investigation and Monitoring (SWIM) instrument carried by the China France Ocean ~~Satellite (?), the direct measurement~~ SATellite (CFOSAT)  
5 ~~(??), direct spaceborne measurements~~ of surface current ~~has have~~ been limited to a few regions and ~~a single component single~~ projections of the current vector ~~(???)~~. Several concepts based on SAR interferometry ~~(??)~~ or Doppler scatterometry ~~(??)~~ have been proposed for satellite missions aimed at mapping the ocean surface current ~~vectors~~ vector (see review by ?). Airborne demonstrators have also been developed in that context ~~(??)~~, and are now becoming operational tools for oceanographic research.

10 ~~Direct Doppler measurements contain a geophysical Doppler ( $U_{GD}$ )~~ The Doppler frequency shift (DFS) signal provided by these phase-resolving radar instruments is complex: it contains a geophysical contribution due to waves ( $U_{WD}$ ) and currents ( $U_{CD}$ ) and a ~~and currents, as well as a large non-geophysical Doppler ( $U_{NG}$ ) contribution due to the platform velocity and acquisition geometry~~ motion. The platform velocity in space being of the order of 7 km/s for low Earth orbit ~~it is~~, it is obviously critical to have an accurate ~~estimation knowledge~~ of the measurement geometry to correctly estimate ~~this the~~ non-  
15 ~~geophysical Doppler component. The contribution due to ocean waves is however also an order of magnitude larger than the expected TSCV contribution (?), and must also be precisely estimated, using an accurate sea state description.~~

~~As reviewed by ?, two main satellite concepts have emerged. One is a kilometer-scale resolution instrument based on InSAR (?). For this type of instruments, global coverage is not feasible today due to power and downlink capacity constraints. The other, based on Doppler satellite scatterometry, allows for a global monitoring of mesoscale currents at lower, but still~~  
20 ~~unprecedented resolution, including the associated divergence field and ageostrophic motions. In that second category, the proposition of a~~ The Sea surface KInematics Multiscale monitoring (SKIM) satellite mission has been designed to address all these requirements and provide direct global-coverage measurements of TSCV. It is based on a the combination of two instruments, the SKIM Ka-band Radar (SKaR), a phase-resolved SWIM-like conically scanning radar, with a Doppler processing that allows to measure the surface current vector by combining different viewing azimuths across the satellite swath (?). SKIM  
25 ~~is built around a providing simultaneous Ka-band pulsed radar with a specific processing chain using the phase difference of consecutive pulse returns to measure the line-of sight velocity of ocean surface targets, together with the more usual Radar Backscattering Cross-Section (NRCS). Both NRCS and velocity are resolved in range. In azimuth the resolution is 6 km for Doppler and 300m using unfocused SAR processing for NRCS. The instrument also includes a nadir altimeter that is necessary for tracking the ocean surface and set the timing of radar pulses, but can be used for sea level, geostrophic currents, and other~~  
30 ~~nadir altimetry applications. In summary SKIM is a microwave Doppler Wave and Current Scatterometer, and these capabilities to measure sea level and directional wave spectra are used to improve on the retrieval of the surface current vector~~ observations of sea state and DFS, and a state-of-the-art nadir altimeter, providing the sea surface elevation observations necessary to control the SKaR acquisition geometry with sufficient accuracy, but also significant wave height and wind speed observations.

SKIM ~~is was pre-selected as~~ one of the two candidate missions for the European Space Agency (ESA) 9th Earth Explorer.

35 As part of the detailed design ~~an feasibility studies and feasibility~~ (phase A) ~~studies~~, ESA funded a dedicated ~~measurement campaign, measurements campaign, Drift4SKIM,~~ which was organized from November ~~21 to 27~~ ~~21st to 27th~~, 2018, off the French Atlantic coast, ~~in an area~~ with sea states characteristic of the open ocean and a well known tide-dominated current regime ~~that is,~~ monitored by a ~~two-sites~~ 12 MHz High-Frequency radar ~~system~~ (?). A range of in-situ instruments (surface current drifters, drifting and moored wave-measuring buoys), as well as two airborne Doppler radars operating in ~~the~~ Ku-

5 (KuROS) and Ka- (KaRADOC) bands ~~were operated, were deployed.~~ The campaign goals were to:

- ~~demonstrate~~ ~~Demonstrate~~ how the non-geophysical ~~Doppler~~  $U_{NG}$  ~~contribution~~  $V_{NG}$  ~~to the DFS~~ can be estimated from the motion of the platform carrying the radar, the antenna ~~pattern diagram~~ properties and the ~~azimuthal and incidence dependence~~ ~~azimuth and incidence-angle dependencies~~ of the radar cross section.
- ~~further explore the contribution to~~  $U_{GD}$  ~~of~~ ~~Explore the geophysical component~~  $V_{GD}$  ~~and its decomposition as a sum of contributions due to~~ currents and waves ~~contributions, respectively~~  $U_{CD}$  ~~and~~  $U_{WD}$ , ~~and illustrate how~~  $U_{GD}$  ~~can be split into these two contributions~~ (?),

10 
$$U_{GD} = U_{CD} + U_{WD},$$

~~where the wave Doppler velocity plays the same role as the Bragg velocity in High-Frequency radar measurements~~ (?).

15  $V_{CD}$  ~~and~~  $V_{WD}$  (?).

- ~~validate~~ ~~Validate~~ the Radar Sensing Satellite Simulator (?) and its capability to ~~adapt to simulate~~ airborne configurations.

---

**Figure 1.** (A) Schematic of ATR-42 and KuROS instrument and definition of viewing angles, azimuth  $\varphi$  and incidence ~~angle~~  $\theta$ , and (B) comparison with the SKIM viewing geometry. ~~A~~ ~~The unit vector~~  $e_\varphi$  ~~is the projection on the horizontal of the line of sight direction vector.~~ ~~The~~ variation of surface backscatter across the footprint and as a function of azimuth  $\varphi$ , ~~which causes the effective mispointing~~  $\delta\varphi$ , is represented ~~by the as a~~ grey shading, ~~and gives an effective mispointing~~  $\delta$ . In ~~the~~ KuROS data, each measurement is integrated in azimuth across the antenna lobe. In the case of SKIM, the use of unfocused SAR ~~processing~~ allows the separation of echoes in the azimuth direction with a resolution  $dDop \simeq 300$  m.

As highlighted in Figure 1, ~~the viewing geometry of~~ an airborne system ~~differs from a satellite by its viewing geometry is~~ ~~vastly different from that of a satellite system~~, with a much smaller footprint and ~~spatially varying incidence angles~~ ~~incidence angle variations~~ at scales comparable to the wavelength of the dominant ocean waves. ~~The other~~ ~~Another~~ obvious difference

20 is the stability of the platform and its velocity, 7 km/s for low Earth orbit, and around 120 m/s for the ATR-42 aircraft used here. As a result, ~~transposing~~ the performance of ~~the airborne system requires a detailed simulator to be transposed an airborne system~~ to a satellite system ~~. Still, airborne campaigns are useful to test effects that also occur in orbit, but with different~~

magnitudes. The requires a thorough analysis, supplemented by carefully designed and validated simulation tools. Performing this analysis is however worthwhile, as it leads one to develop valuable insight into the instrument imaging principle and design trade-offs.

This article is intended to provide an overview of the Drift4SKIM campaign data and a first discussion of their implications for the emerging field of near-nadir Doppler radar observations of TSCV. It is structured as follows: the principle of the pulse-pair measurements and the non-geophysical contributions different contributions to the observed DFS are detailed in section 2 and Appendix A. Section 3 presents the set up of the campaign and 2 and Appendix ???. Section ??? gives a brief account of the field work performed and conditions encountered during the campaign. The results of the airborne measurements are exposed in section 4.???. Results and implications for SKIM are then discussed in section 5.???. Conclusions and perspectives follow in section 6.???

## 2 Radar Near-nadir radar Doppler measurements of ocean velocities at different scales: theory

Details of how the phase difference in pulse pairs is related to the relative motion of a target, in our case surface gravity waves, and the radar are given in Appendix ???. In Ship-borne Doppler measurements of ocean currents are routinely performed using so-called “Vessel-Mounted Acoustic Doppler Current Profilers” (VMADCPs, see for instance ?). Some of the end-data processing concepts transpose directly to the space-borne context: the raw DFS signal contains a large non-geophysical contribution due to the platform motion, which must be estimated from ancillary sensors and compensated. The accuracy of the final geophysical product is practically set by the accuracy of the non-geophysical velocity estimation and correction procedure. In the VMADCP context, however, the backscattering elements responsible for the production of the acoustic return signal (particulate suspended matter, zooplanktonic organisms) are passive and follow accurately the water mass. This does not carry over in the electromagnetic case: here, the return signal is produced by the interaction of the transmitted signal with the roughness elements of the sea surface, which move with respect to the water mass with an intrinsic phase velocity that is an order of magnitude larger than typical ocean currents. This effect is for instance well known in the line-of-sight ground-based HF-radar currents measurement context (?), and must also be compensated.

In our case, the measurement geometry is represented in figure 1, and the line-of-sight Doppler velocity  $V_{LOS}$  looking at looking towards incidence angle  $\theta$  and azimuth  $\varphi$  (in this paper, line-of-sight DV contributions are denoted by “V”, and the corresponding horizontal velocity contributions are denoted by “U”) is the sum of the projection of a horizontal current contribution  $U_{CD}(\varphi)$ , a horizontal geophysical Doppler velocity contribution  $U_{GD}(\varphi)$ , wave-induced contribution  $V_{WD}(\theta, \varphi)$  and a non-geophysical velocity  $V_{NG}$ . The following measurement equation is given by projections of the target and sensor velocity vectors onto the line of sight as shown in figure 1, contribution  $V_{NG}(\theta, \varphi)$ . The equation that permits the retrieval of the TSCV contribution  $U_{CD}(\varphi)$  from the raw measured  $V_{LOS}$  can be written as

$$U_{GD}(\varphi) = \frac{V_{LOS}(\theta, \varphi) - V_{NG}(\theta, \varphi) - V_{WD}(\theta, \varphi)}{\sin \theta} \quad (1)$$

The aim of this section is to provide a detailed analysis of the different terms of this expression. The non-geophysical contribution  $V_{\text{NG}}$  is discussed in subsection ?? and Appendix ?. The wave Doppler contribution is discussed in subsection ???. A brief summary of the measurement error budget is finally provided in subsection ??.

## 2.1 Non-geophysical velocity $V_{\text{NG}}$

In practice,  $V_{\text{NG}}$  is the radar velocity projected onto the effective look direction, that includes an apparent azimuth mispointing  $\delta$  due to the finite antenna beamwidth combined with the variations of NRCS in the radar footprint. This NRCS variability includes both spatial gradients and azimuthal gradients. As a result, the beamwidth is a very important parameter of the radar, and the values for KuROS and KaRADOC are given in Table 1. For KuROS they have been determined following the procedure detailed in Appendix B. For KaRADOC, they are the result of anechoic chamber measurements (Appendix ??).

The KuROS azimuth beamwidth and boresight are slightly variable with elevation. The details of the antenna pattern depend on the aircraft attitude and ~~As mentioned above, the accuracy of ship-borne acoustic Doppler current measurements is affected in a dominant way by the platform motion compensation process. In the space-borne context, the orientation-platform velocity is almost three orders of magnitude larger ( $7000 \text{ m.s}^{-1}$  vs.  $10 \text{ m.s}^{-1}$ ). The accuracy requirements are thus tremendously exacerbated, and attention must in particular be paid to the detailed effects of the antenna relative to the aircraft. In radiation diagram and sea-surface Normalized Radar Cross Section (NRCS) variations with space and observation azimuth. A detailed discussion of these effects is given in Appendix ??.~~

In summary, in the case of level flight and for low incidence observations, one can approximate the antenna pattern as a Gaussian 1-way antenna pattern with a parameter  $\sigma_\alpha$ . Using usual radar conventions the beamwidth is given by a 1-way full antenna width  $\alpha_{-3\text{dB}}$ , that is the angle between the two directions for which the transmitted power is reduced by 3 dB compared to the maximum radiated power in the boresight direction. With the usual approximation  $10\log(0.5)/\log(10) \simeq -3$ , we have

$$\sigma_\alpha = \alpha_{-3\text{dB}} / \sqrt{8 \log(2)}.$$

a sufficiently narrow radiation diagram,  $V_{\text{NG}}$  can be approximated as the radar carrier velocity projected on an effective look direction. This effective look direction differs from the geometric boresight direction by an effective azimuthal mispointing  $\delta\varphi$  due to the finite antenna beamwidth combined with the variations of NRCS within the radar footprint, and by an effective incidence angle mispointing  $\delta\theta$  due to radar timing or surface-tracking errors.

For KuROS this beamwidth varies slightly with the incidence angle, with a minimum  $\alpha_{-3\text{dB}} = 15.0^\circ$  (corresponding to  $\sigma_\alpha = 6.36^\circ$ ) for a boresight incidence angle of  $11.8^\circ$  (As detailed in Appendix ??) and increases for other angles.

More important for our measurements is the ground-projected azimuthal aperture. This is given by equating the length of the segment FE between the footprint center and the footprint edge in the triangle RFE of figure 1. B and the segment FE in the triangle NFE in figure 1. C. Namely  $FE/FR = \tan(\sigma_\alpha/2)$ ,  $FE/(2 \text{ FN}) = \tan(\sigma_\phi/4)$ . The beamwidth at the working incidence angle is thus a very important parameter of a radar intended for TSCV measurements. Table 1 summarizes the parameters of the KuROS and KaRADOC antennas. For KuROS they have been determined following the procedure detailed in Appendix

**Table 1.** KuROS and KaRADOC antenna radiation diagrams characteristics. All angles are in degrees. [See Appendix ?? for the definitions of  \$\alpha\$  and  \$\beta\$](#)

Instrument	KuROS	KaRADOC
Polarization	HH	HH
Azimuth 1-way beamwidth ( $\alpha_{-3\text{dB}}$ )	15.0	1.85
Elevation 1-way beamwidth ( $\beta_{-3\text{dB}}$ )	22.6	1.20
Boresight elevation ( $\beta^0$ )	11.8	12.1
Boresight azimuth (deg)	$\sim 0$	-0.05

For KaRADOC, they are the result of anechoic chamber measurements (Appendix ??). As discussed in Appendix ??, these parameters describe the antenna radiation diagrams when expressed as functions of variables,  $\alpha$  and  $\beta$ . Note that the point E is the point on the footprint edge that is at the same distance from the radar R (same range gate) as the footprint center F. This gives,

$$\sigma_\varphi = 4 \arctan [\tan(\sigma_\alpha/2)/(2 \sin \theta)].$$

As shown in Figure 1.C, when  $\beta$ , which do not coincide with azimuth and incidence angle. In the case of constant altitude flight and near-nadir observations with the antenna looking towards azimuth  $\varphi_b$ , one can however obtain a Gaussian approximation to the 1-way radiation diagram as:

$$G \simeq \exp \left[ -\frac{(\varphi - \varphi_b)^2}{2} \left[ \frac{\sin^2(\theta)}{\sigma_\alpha^2} + \frac{(\beta_0 - \tan(\theta)) \tan(\theta)}{\sigma_\beta^2} \right] \right], \quad (2)$$

where  $\sigma_\alpha = \alpha_{-3\text{dB}}/\sqrt{8 \log(2)}$  and  $\sigma_\beta = \beta_{-3\text{dB}}/\sqrt{8 \log(2)}$ . For  $12^\circ$  observations the second term in the exponential can safely be neglected, and the effective azimuthal beamwidth can be estimated as:

$$\varphi_{-3\text{dB}} = \frac{\alpha_{-3\text{dB}}}{\sin(\theta)}. \quad (3)$$

When projected on the ground, the angle  $\varphi_{-3\text{dB}}$  is much thus larger than  $\alpha_{-3\text{dB}}$ . In the case of a narrow beam, the 1-way antenna pattern  $G$  remains Gaussian as a function of  $\varphi$  as given by a factor  $1/\sin(\theta)$ , equal to 4.8 for  $12^\circ$  measurements. Provided that the beam is not too wide, the Gaussian approximation eq. (??) with a of  $G$  as a function of  $\varphi$  can then be used, with parameter

$$\sigma_\varphi \simeq \alpha_{-3\text{dB}} / \left[ \sin \theta \sqrt{8 \log(2)} \right]. \quad (4)$$

When the sea surface NRCS is variable, this finite radar aperture gives an apparent mispointing that is the difference between the apparent Due to the width of the azimuthal aperture, the NRCS-weighted line-of-sight azimuth  $\varphi_a$  and can differ from the boresight azimuth  $\varphi_b$ , as detailed in Appendix A-

$$\delta = \varphi_a - \varphi_b = \frac{1}{2} \frac{\sigma_\alpha^2}{\sin^2 \theta} \frac{1}{\sigma^0} \frac{\partial \sigma^0}{\partial \varphi}.$$

If not corrected for, this apparent mispointing gives a spurious velocity that is the projection of the platform velocity onto the apparent line of sight

$$25 \quad U_{AGD} = \delta \sin \theta \sin \varphi_b V_p.$$

where  $V_p$  is the by a mispointing angle  $\delta\varphi$ . Expressions for  $\delta\varphi$  are obtained in Appendix ?? in the two limiting cases of slow linear and fast sinusoidal variations of the ocean surface NRCS with respect to azimuth. In the slow variation case,  $\delta\varphi$  is obtained as

$$\delta\varphi = \varphi_a - \varphi_b = \frac{1}{2} \frac{\sigma_\alpha^2}{\sin^2 \theta} \frac{1}{\sigma^0} \frac{\partial \sigma^0}{\partial \varphi}. \quad (5)$$

Denoting by  $\varphi_t$  the flight track azimuth and  $V_p$  the along-track velocity of the platform carrying the radar in the frame of reference of the solid Earth-

For our experimental KuROS configuration  $\sigma_\alpha \simeq 6.36^\circ = 0.11$  rad at  $\theta = 12^\circ$ . As shown in section 3,  $\partial_\varphi \sigma^0 / \sigma^0$  is of the order of  $0.10 \text{ rad}^{-1}$  for a uniform wind speed of 11 m/s. This gives an apparent mispointing of the order of  $\delta = 0.8^\circ = 14 \times 10^{-3}$  rad, which would correspond to a 1.7 m/s error on  $U_{GD}$ -

As detailed in Appendix A, eq. (6) only applies for a narrow beam when projected on the ground, which is not a very good approximation for the KuROS case, even at an incidence of  $12^\circ$ . As shown in figure 2, the Gaussian approximation for the antenna pattern as a function of  $\varphi$  gives a too narrow distribution and does not take properly into account the azimuthal integration, leading to an overestimation of  $U_{AGD}$ -

flight velocity, the spurious ‘‘Azimuth Gradient Doppler’’ contribution to the DV caused by the mispointing reads

$$U_{AGD} = \sin(\varphi_b - \varphi_t) \frac{V_p}{2} \frac{\sigma_\alpha^2}{\sin^2 \theta} \frac{1}{\sigma^0} \frac{\partial \sigma^0}{\partial \varphi}. \quad (6)$$

As an example, figure 2 shows the variations of the two-way antenna radiation diagram  $G^2$ , of its Gaussian approximation, and of the  $G^2 \widetilde{\sigma^0}$  (see eq. ??) product as a function of azimuth at  $12^\circ$  incidence angle, for a northward-looking KuROS antenna ( $\varphi_b = 0^\circ$ ), using  $\sigma^0$  data from the Drift4SKIM campaign on 22 November 2018, with a wind speed of  $11 \text{ m}\cdot\text{s}^{-1}$  from azimuth  $140^\circ$  /11/22. The effect of the wind-induced azimuthal gradient of  $\sigma^0$  is to shift the effective radiation pattern diagram towards the brighter upwind/downwind directions, with an apparent pointing azimuth  $\varphi_a$ . The shift induced in this case is  $\delta = \varphi_a - \varphi_b = -0.81^\circ = -15 \times 10^{-3}$  rad, a very large number compared to the 85 microradians  $\delta\varphi = \varphi_a - \varphi_b = -0.81^\circ = -15 \times 10^{-3}$  r. For comparison (see section ?? and table ??), the pointing accuracy required to meet the 1 achieve a 15 cm/s horizontal current accuracy goal error on the horizontal current in the airborne configuration is 1.2 milliradians.

Here, it is important to note that KuROS was not specifically designed for this experiment, but primarily as a Calibration/Validation instrument for the CFOSAT mission, which required a broad radiation diagram. Though the analysis of the KuROS data helped uncover many interesting effects relevant to Doppler observations of the sea surface, its design was not fully appropriate to validate the inversion of the geophysical velocities, for which the pencil-beam antenna diagram of KaRADOC was better suited.

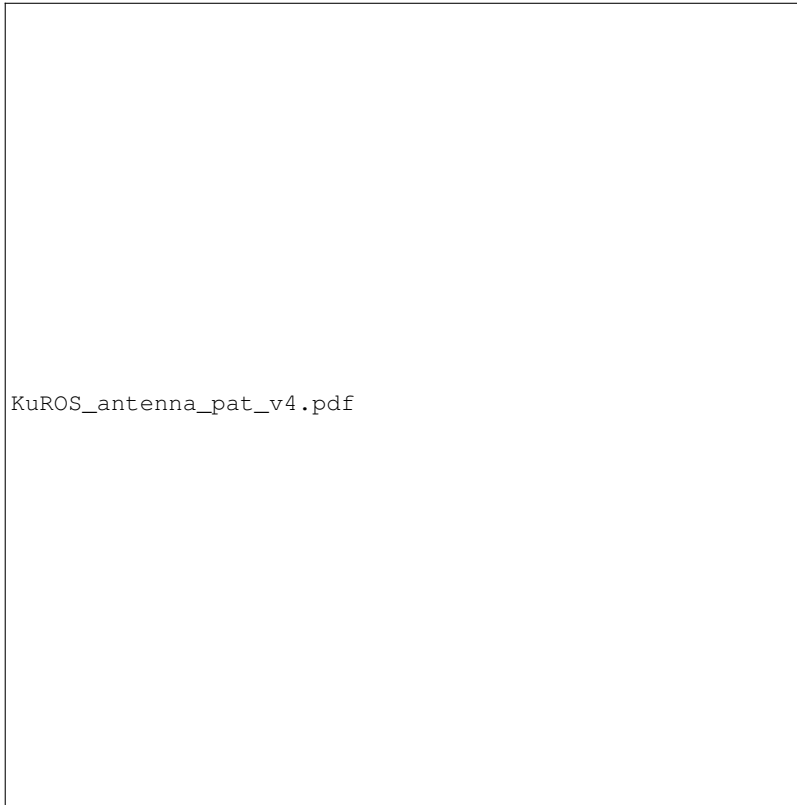


**Figure 2.** KuROS azimuth integral weight at  $\theta = 12^\circ$  for a north-facing ( $\varphi_b = 0^\circ$ ) antenna (black), Gaussian approximation (eq. ??) (green) and variation of  $\tilde{\sigma}^0$  for a typical  $11 \text{ m.s}^{-1}$  wind from  $140^\circ$  (dashed black). The peak of the  $\tilde{\sigma}^0 G^2$  product (red) is shifted with respect to the peak of  $G^2$  by  $\delta \simeq -0.63^\circ$   $\delta\varphi \simeq -0.81^\circ$ .

Figure 3.A shows a typical example of the azimuthal variation of  $\tilde{\sigma}^0$  for an incidence of at  $12^\circ$  using a incidence angle for Ku-band radar. As expected for near-nadir measurements (??)(???), the NRCS is largest in the downwind look direction ( $\varphi = -40^\circ$   $\varphi = 320^\circ$ ), has a secondary peak in the upwind direction, and is weakest in the crosswind look directions. Figure 3.B shows the expected spurious contribution corresponding  $U_{AGD}$  to the geophysical velocity  $U_{GD}$ , if the apparent mispointing  $\delta$  is not corrected for. This uses contribution for the KuROS and KaRADOc cases, using an aircraft velocity  $V_p = 120 \text{ m s}^{-1}$  for the KuROS and KaRADOc cases. The and the Ku-band NRCS fit has been used for the Ka-band instrument as well. This for both instruments (this is a reasonable assumption for order-of-magnitude estimates). As detailed in Appendix ??, equations (6) and (7) only apply for a narrow beam when projected on the ground, which is not a very good approximation for the KuROS case, even at  $12^\circ$  incidence angle. As shown in figure 2, the Gaussian approximation for the antenna diagram as a function of  $\varphi$  gives a too narrow distribution and does not take properly into account the azimuthal integration, leading to an overestimation of  $U_{AGD}$ . It is clear however that even the more exact equation ?? gives very large correction magnitudes, in excess of  $1.2 \text{ m.s}^{-1}$  in some azimuth ranges.

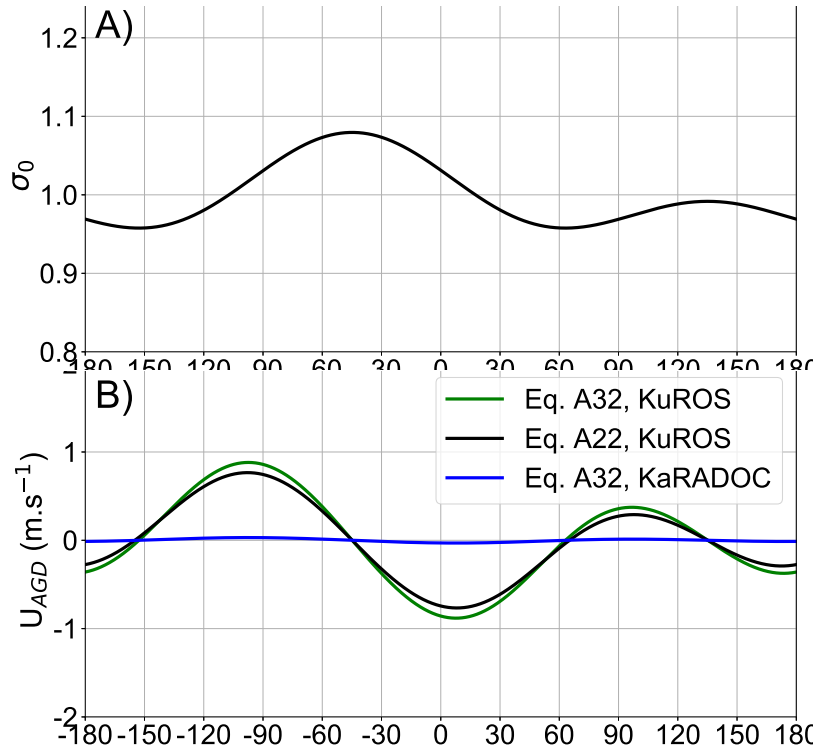


**Figure 3.** A) Example of azimuthal variation of  $\widetilde{\sigma}^0$  at  $12^\circ$  incidence angle, corresponding to the November 22-22nd case (11 m/s wind from  $140^\circ$ ) discussed in section 3??, and B) associated spurious velocity  $U_{AGD}$  as a function of look azimuth  $\varphi_b$  in the case of a port-looking antenna mounted on a platform in level-constant altitude flight at 120 m/s. For the KuROS case, the green lines show the result of the approximate eq. (??) and the black lines show the result of the full azimuthal integration eq. (??). The blue line represents the result of eq. (??) for the KaRADOC, using the Ku-band same  $\widetilde{\sigma}^0$  as in the Ku-band case.

5 Because both the azimuth gradient Doppler  $U_{AGD}$  and the spatial gradient Doppler  $U_{SGD}$  are contribution to the observed DV is proportional to  $V_p \sigma_\varphi^2$  it is clear that the broad KuROS antenna pattern requires a very accurate estimation to correct for  $U_{AGD}$ , which is almost negligible, this effect is much larger (and correcting it is correspondingly more demanding in terms of antenna characterization) for KuROS, than for KaRADOC or DopplerScatt (?), thanks to their narrow azimuthal beam aperture. Another remark is that the approximate expression eq. (??), though it gives the appropriate dependency of  $U_{AGD}$  with respect to look azimuth, tends to over-predict its magnitude, as the widening associated to the ground projection saturates for broad beams.

240 In particular at small scales, spatial gradients add to the azimuthal gradient and also induce a spurious velocity with the same expression as a function of  $\widetilde{\sigma}^0$ . Using the simple case of a single Fourier component  $\widetilde{\sigma}^0 = \varepsilon \sin[\nu(\varphi - \varphi_b)]$  allows one to



evaluate the importance of different scales. The azimuthal shift can be obtained as

$$\delta = \varepsilon \exp\left(-\frac{(\nu^2 + 1)\sigma_\varphi^2}{4}\right) \sinh\left(\frac{\nu\sigma_\varphi^2}{2}\right).$$

245 In the slow-variation limit  $\nu, \sigma_\varphi \rightarrow 0$ , and eq. (??) this expression coincides with eq. (??). For faster variations, one sees that the largest disturbance is obtained when  $\nu \sim \sqrt{2}/\sigma_\varphi$ . This azimuthal wavenumber is such that the footprint can host a bright and a dark patch, one on either side of the look direction. This configuration creates the largest disturbance for a given value of the brightness contrast  $\varepsilon$ .  $\delta$  in this case is given by

$$\delta_{\max} = \varepsilon \sigma_\varphi e^{-1/2} / \sqrt{2}.$$

250 Although the relative variations  $\partial\sigma^0(\varphi)/\partial\varphi/\sigma^0$   $\partial_\varphi\sigma^0/\sigma^0$  are larger for larger incidence angles, this is more than compensated by the  $1/\sin^2\theta$  reduction in azimuthal diversity across the footprint. This ~~is why this effect can~~ effect can thus be neglected for much higher incidence angles (?).

— Although the relative variations  $\partial\sigma^0(\varphi)/\partial\varphi/\sigma^0$  are larger for larger incidence angles, this is more than compensated by the  $1/\sin^2\theta$  reduction in azimuthal diversity across the footprint. This is why this effect can be neglected for much higher incidence angles (?).

255 When  $\sigma^0$  varies at scales comparable to the footprint, e.g.  $\sigma^0 = a^0[1 + \varepsilon \sin(\nu\varphi)]$ , then

260 This mispointing is maximum for  $\nu = \sin\theta/\sigma_\alpha$ , and the smaller scales, those with higher values of  $\nu$ , average out. The larger scales only give a small variation across the antenna pattern. This will be further discussed in section 5 in the context of SKIM. For large scale variations,  $\nu \rightarrow 0$  and  $\varepsilon\nu \rightarrow \partial\sigma^0/\partial\varphi/\sigma^0$ , so that we recover eq. (6).

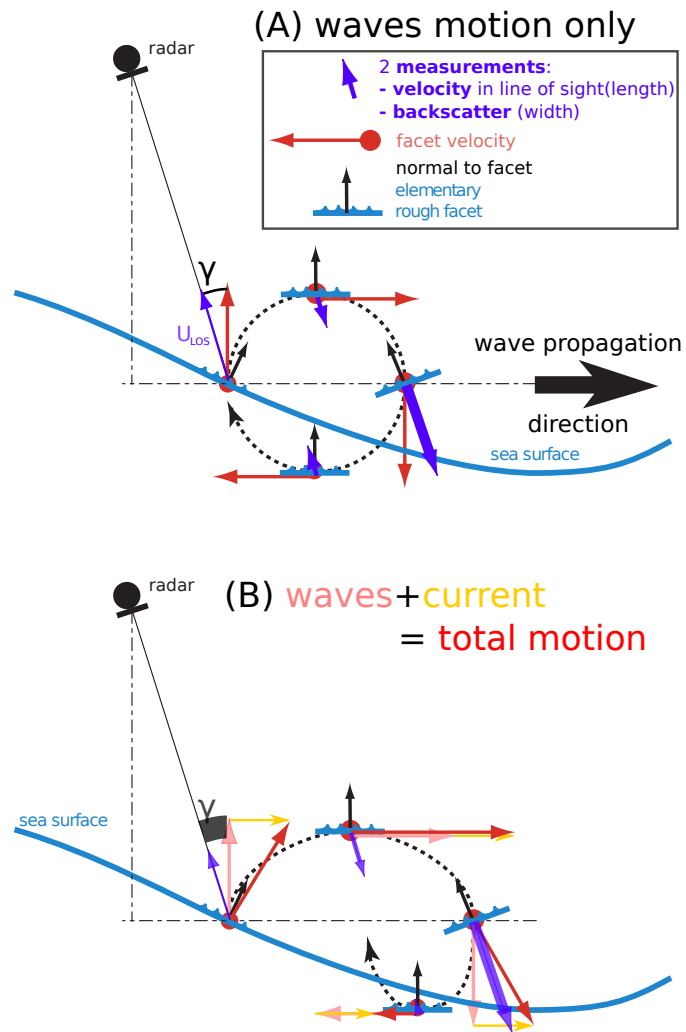
## 2.2 Geophysical velocity $U_{\text{GD}}$ : Waves and Current Doppler velocities

265 The geophysical part of the Doppler shift DFS measured by a microwave radar over the ocean, using both Along-Track-Interferometry and Doppler centroid techniques ~~is caused by the backscatter-weighted average of the surface velocities along the emerges from the average over the instrument field of view (FOV) of the backscatter-weighted~~ line of sight projection of the surface velocity, as illustrated in figure ??.

For a perfect sine wave of period  $T$  propagating over deep water, the phase speed of the wave is

$$C = \frac{gT}{2\pi} + U \cos(\varphi_w - \varphi_U)$$

where  $U$  is the current speed,  $\varphi_w$  is In the well-understood case of decametric electromagnetic waves interacting with the sea surface at grazing incidence, the interaction is dominated by the Bragg coherent backscattering mechanism (?), in which the



Schematic of (A) wave and (B) wave and current contributions to Doppler velocities at the scale of elementary facets. These are averaged into a radar pixel, so that sub-pixel waves contribute a mean velocity due to the correlation of surface slopes and velocities in the wave field. HF radars operationally used to measure the ocean TSCV in coastal areas (??).

280 ~~In the case~~ In the case of the near-nadir interaction of microwaves with the sea surface, which is the configuration considered for SKIM and used by the AirSWOT, KuROS and KaRADOC airborne instruments, this mental picture must be adapted: the Bragg scattering mechanism is not dominant, and the main contribution comes from quasi-specular reflections on those facets of KuROS, SKIM, or other systems for which the backscattering mechanism is not selective, a superposition of waves contributes. We get a compound mixture of  $C$ 's, and the different terms become (??),

$$\begin{aligned} \underline{C} &\rightarrow \underline{U_{GD}} \\ 285 \quad \frac{gT}{2\pi} &\rightarrow \underline{U_{WD}} \\ \underline{U} &\rightarrow \underline{U_{CD}} \end{aligned}$$

290 where the current  $U$  sampled at depth  $k/4\pi$  (?) for a monochromatic sine wave, is now a weighted average  $U_{CD}$  of the currents at different depths, where the weighting function sea surface which are normal to the Ewald vector. The backscattering cross-section of the sea surface and DFS in this case do not depend on the properties of a single Fourier component of the sea state, but on the probability density function of the sea surface slope, which is determined by the wave slope spectrum. Indeed, the velocity  $U_{CD}$  integrates the velocity of the tilted facets on the ocean surface. Within facets, quasi-specular and specular points are selected, further modulated by the local directional tilts  $\nabla\eta$ , leading to a modulated averaged intensity and a weighted velocity as

$$\begin{aligned} \underline{\sigma^0} &\equiv \underline{\int \sigma(\nabla\eta)P(\nabla\eta)d\nabla\eta} \\ 295 \quad \underline{\sigma^0 * V_{LOS}} &\equiv \underline{\int V_{LOS}(\nabla\eta)\sigma(\nabla\eta)P(\nabla\eta)d\nabla\eta} \end{aligned}$$

with  $\sigma(\nabla\eta)$  an individual local radar cross section, corresponding to a tilted facet, with a local line-of-sight velocity  $V_{LOS}$ , and  $P(\nabla\eta)$  the facet-tilt probability distribution, complex functional of its entire directional spectrum.

300 As the incidence angle is increased beyond  $25^\circ$ , As discussed by (?), who applied it to the analysis of AirSWOT NRCS and DFS data collected during the Gulf of Mexico LASER experiment of 2016, the backscatter is dominated by Bragg scattering and theoretical framework appropriate to this configuration is the Kirchoff Approximation (?). In this approximation, the geophysical DFS  $\omega_{GD}$  can be expressed as:

$$\omega_{GD} = -i \left. \frac{\partial_\tau C}{C(\tau)} \right|_{\tau=0}, \quad (7)$$

where  $C(\tau)$  is the temporal covariance function of the ensemble averaged electromagnetic field backscattered in the direction of the radar.

305 Assuming Gaussian statistics for the sea surface, introducing  $\rho(\boldsymbol{\xi}, \tau) = \langle \eta(\mathbf{x} + \boldsymbol{\xi}, t + \tau) \eta(\mathbf{x}, t) \rangle$  the space-time covariance function of the sea surface elevation, and  $\mathbf{Q}_H$  and  $Q_z$  the horizontal and vertical components of the Ewald vector, one obtains  $C(\tau)$  and  $\partial_\tau C$  as

$$C(\tau) = \int e^{i\mathbf{Q}_H \cdot \boldsymbol{\xi}} \left[ e^{Q_z^2(\rho(\boldsymbol{\xi}, \tau) - \rho(\mathbf{0}, 0))} - e^{-Q_z^2 \rho(\mathbf{0}, 0)} \right] d\boldsymbol{\xi} \quad (8)$$

$$\partial_\tau C(\tau) = Q_z^2 \int \partial_\tau \rho(\boldsymbol{\xi}, \tau) e^{i\mathbf{Q}_H \cdot \boldsymbol{\xi}} e^{Q_z^2(\rho(\boldsymbol{\xi}, \tau) - \rho(\mathbf{0}, 0))} d\boldsymbol{\xi}. \quad (9)$$

310 The clear upwind-downwind asymmetry of  $\sigma^0$  observed in the Drift4SKIM radar observations (see figure ??) shows that the Gaussian assumption, which is unable to describe such skewness-related effects, is clearly questionable. It is however the only practical option, as going further would require prescriptions for the higher-order statistics of the sea surface which are at present not available.

The occurrence of  $\rho$  as the argument of an exponential in these integrals renders further analytical progress difficult (see however ?)

315 Approximate expressions can however be obtained by performing a Taylor-expansion of  $\rho$  in the neighborhood of the origin. This results in a Gaussian approximation of the integrand. The integrals can be readily evaluated, yielding:

$$\omega_{GD} \simeq -\mathbf{Q}_H^T \times [\nabla_{\boldsymbol{\xi}\boldsymbol{\xi}} \rho]^{-1} \times \partial_\tau \nabla_{\boldsymbol{\xi}} \rho. \quad (10)$$

The derivatives of  $\rho$  are taken at  $\boldsymbol{\xi} = \mathbf{0}, \tau = 0$ , and can be expressed as moments of the directional sea state spectrum  $S_d(\mathbf{k})$  as:

$$320 \partial_\tau \nabla_{\boldsymbol{\xi}} \rho = \mathbf{msv}, \quad \nabla_{\boldsymbol{\xi}\boldsymbol{\xi}} \rho = -\mathbf{Mss}, \quad (11)$$

where, in the notations of (?),  $\mathbf{msv}$  stands for the “mean slope velocity” and  $\mathbf{Mss}$  for the mean square slope matrix,

$$\mathbf{msv} = \begin{bmatrix} \text{mss}_{xt} \\ \text{mss}_{yt} \end{bmatrix}, \quad \mathbf{Mss} = \begin{bmatrix} \text{mss}_{xx} & \text{mss}_{xy} \\ \text{mss}_{yx} & \text{mss}_{yy} \end{bmatrix}, \quad (12)$$

with

$$\text{mss}_{x^\alpha y^\beta t^\gamma} = 2 \int_{\mathbb{R}^2} k_x^\alpha k_y^\beta \omega^\gamma S_d(\mathbf{k}) d\mathbf{k}. \quad (13)$$

325 The surface current enters through its effect on the dispersion relation of surface waves  $\omega(\mathbf{k})$ . In the presence of a vertically homogeneous current  $\mathbf{U}$  (a detailed discussion of the effect of shear can be found in ?),

$$\omega(\mathbf{k}) = \mathbf{k} \cdot \mathbf{U} + \omega_0(|\mathbf{k}|), \quad (14)$$

where

$$\omega_0(|\mathbf{k}|) = \sqrt{g|\mathbf{k}|(1 + |\mathbf{k}|^2/\kappa_M^2)}, \quad (15)$$

330 is the dispersion relation of gravity-capillary waves in deep water, with  $\mathbf{k}$  the wavevector and  $k_M = 363.2 \text{ rad.m}^{-1}$  the wave number corresponding to the gravity-capillary regime transition. Introducing this expression in equation (??), and defining  $\mathbf{msv}_0$  as the spectral moment obtained using the dispersion relation (??) in equation (??), one obtains the approximate DFS as

$$\omega_{GD} = \mathbf{Q}_H^T \cdot [\mathbf{M}_{ss}^{-1} \times \mathbf{msv}_0 + \mathbf{U}], \quad (16)$$

335 and the corresponding  $V_{GD}$  as

$$V_{GD} = -\sin(\theta) \mathbf{e}_\varphi \cdot [\mathbf{M}_{ss}^{-1} \times \mathbf{msv}_0 + \mathbf{U}]. \quad (17)$$

While clearly over-simplified (it is for instance independent of the electromagnetic wavelength, which is known to have a significant influence on  $\sigma^0$ ), this expression has a definite pedagogical interest, as it allows one to distinguish a number of interesting features:

- 340 – The raw velocity projection  $V_{GD}$  accessible to Doppler radar instruments is composed of a “genuine” current component  $V_{CD}$ , equal to the projection of the TSCV along the radar line of sight, plus a “Wave Doppler” component  $V_{WD}$  induced by the natural motion of the sea surface.
- This  $V_{WD}$  component involves sea surface statistics of two different natures: the mean slope velocity vector  $\mathbf{msv}_0$  and the phase speeds that contribute are the Doppler-shifted Bragg waves (?). In our case, Bragg scattering is generally negligible except for the lowest wind speeds.
- 345 mean squared slopes matrix  $\mathbf{M}_{ss}$ . To this order of approximation it can be seen as the projection along the radar line of sight of the constant vector  $\mathbf{M}_{ss}^{-1} \times \mathbf{msv}_0$ . In the rest of this article,  $M_{WD}$  denotes the norm of this vector.
- As noted in (?),  $\mathbf{msv}_0$  is equal to one half the surface Stokes drift velocity of deep water waves  $\mathbf{U}_S^\infty$ . As noted in (?), the effective mean squared slopes matrix  $\mathbf{M}_{ss}$  components ( $m_{ss\_shape}$ ), accounting for the electro-magnetic filtering effect and part of the non-gaussianity of the sea surface statistics can be obtained from the derivatives of  $\sigma^0$  as a function of incidence angle for different azimuths.
- 350 – In simple cases such as those represented by parametric spectral forms such as the (?) spectrum used in this work,  $\mathbf{msv}_0$  and the eigenvectors of  $\mathbf{M}_{ss}$  are aligned with the downwind direction, and the Ka-band resonant Bragg scattering scale at  $12^\circ$  is about 2 cm, around the capillary-gravity wave transition, corresponding to  $V_{WD} = G_D \mathbf{Q}_H \cdot \mathbf{U}_S^\infty$  relation proposed in (?) is recovered, with  $G_D = \frac{1}{m_{ss\_slope}}$ .
- 355 – Both these statistics are however known to be influenced by waves at all scales. The asymptotic behaviours of the weighting factors as functions of the surface wave wavenumber in the gravity-waves range are  $k^{3/2}$  and  $k^2$  for the  $\mathbf{msv}_0$  and  $\mathbf{M}_{ss}$  terms, respectively, while the parametric spectrum of (?), used in this work, decays as  $k^{-3}$ , leading to a logarithmic divergence for the  $\mathbf{M}_{ss}$  components, and a slow convergence of the minimum phase velocity of about 23

360 em/s. A general analysis valid for all incidence angles is presented by ?. Here we focus on incidence angles from 4 to 20° where the backscatter modulation is dominated by tilt effects (?).

The correlation of surface slope and line-of-sight velocity defines  $msv_0$  components at high wavenumbers.

- The  $M_{ss}$  components are sensitive to the detailed shape of the spectrum up until the short capillary-waves roll-off or to the electromagnetic cut-off, whichever is reached first.
- 365 – Estimating these terms requires knowledge on all the components of the sea state: the long gravity wave range can be measured (either in-situ, as during the Drift4SKIM campaign, or using the radar measurements themselves as intended in the SKIM context), but the high-wavenumber range can not be neglected, and its effect must be accounted for, for instance through the use of a parametric spectral form.
- The  $msv_0$  vector appears as a multiplicative factor, to which the inverse of the  $M_{ss}$  matrix is applied. These terms  
370 thus have opposing influences on the final result: modifications of the sea spectrum which tend to increase the weight of small-scale components increase the mean slope velocity in direction  $\varphi$ ,  $msv(\varphi)$  (?). For linear ocean waves, this equals the correlation of vertical velocity gradients and displacements, equal to half the Stokes drift in direction  $\varphi$ ,  $U_S \cos(\varphi - \varphi_S)$ . The surface Stokes drift magnitude  $U_S$  and direction  $\varphi_S$  can be computed from wave buoy measurements (??), but also, and rather more, the mean squared slope by which it is divided. A certain degree of stability of the end  
375 result is thus likely.
- On a similarly reassuring note, whereas the low-wavenumber part of the spectrum is affected by swell systems of remote origin, which have arbitrary orientations, the short waves represented by the parametric tail of the spectrum are known to be aligned with the wind direction, and to depend on local variables only (wind strength and direction, fetch).

Figure ?? gives orders of magnitude for the natural range of variability of the different factors thus isolated. Figure ??a shows  
380 the variability of the Stokes drift velocity estimated (following ??) using wind and directional wave measurements collected from 2010 to 2017 at Ocean Station Papa. Even though  $U_S$  is highly correlated with the wind speed, with a Pearson's linear correlation coefficient of 0.85 or so, it has a strong variability with the sea state as illustrated in Fig. ??a.

Using a Kirchoff approximation, the variation of wave Doppler with observation direction  $\varphi$  can be computed from the wave spectrum (eq. 16 in ?, see also Appendix C),

385 
$$U_{WD}(\varphi) = G_D U_S \cos(\varphi - \varphi_{WD})$$

where  $U_S$  is the magnitude of the surface Stokes drift vector, which has a direction  $\varphi_S$ , and the direction  $\varphi_{WD}$  is found to be within a few degrees of  $\varphi_S$ . The Doppler imaging factor  $G_D$  is a weakly varying function of the radar frequency and incidence angle, but also of sea state

$$G_D = \frac{-1}{2\sigma^0 \cos^4 \theta \tan \theta} \frac{\partial \cos^4 \theta \sigma^0}{\partial \tan \theta}.$$

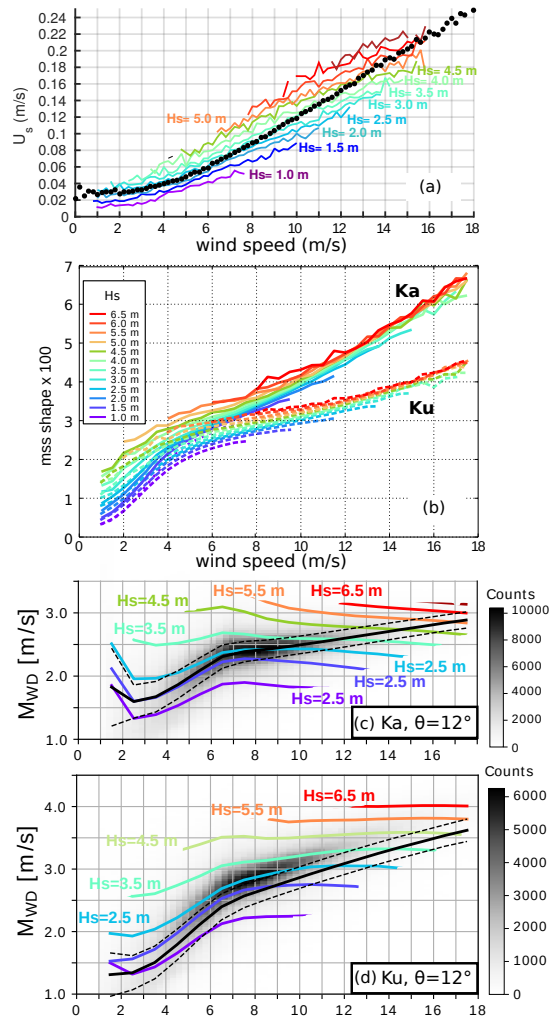


**Figure 5.** Computed variability of the Stokes drift velocity, the diffraction-effective mean square slope  $mss_{\text{shape}}$  and the Wave Doppler velocity magnitude  $M_{\text{WD}}$ . (a) 2010-2017 statistics of Stokes drift magnitude at Ocean Station Papa, computed using the buoy wind speed data and wave data from the nearby WMO buoy 46246, maintained by the University of Washington (?). (b)  $mss_{\text{shape}}$  estimated from GPM satellite back-scatter using modeled co-located wind speed and wave height, reproduced from ?. (c) and (d): Statistics of the Ka- and Ku-band  $M_{\text{WD}}$ , computed using the theoretical model of ? for ocean wave spectra modeled over the global ocean using the WAVEWATCH III model (?), and plotted as a function of the wind speed. The colored curves show the median value for different classes of wave height for a given wind speed, each curve is separated by 0.5 m in (a) and (b) or 1 m in (c) and (d). In (c) and (d), the grey shading represents the histogram of the computed  $M_{\text{WD}}$  values in the global simulation.

390 For Ka-band, we may use a typical variation of  $\sigma^0$  of the form, (??)-

$$\sigma^0 \simeq \frac{\sigma_{\text{max}}^0}{\cos^4 \theta} \exp[-A \tan^2 \theta + B \tan^4 \theta] F(\varphi)$$

where non-Gaussian corrections are,  $B \simeq 0.5676A^{1.332}$  and a strong dependence on the long-wavelength part of the modification of  $\sigma_{\max}^0$  related to the  $mss_{\text{shape}}$  of (?), and  $A = 1/mss_{\text{shape}}$

$$G_D \simeq \frac{2A \tan \theta - 4B \tan^3 \theta}{2 \tan \theta} \simeq \frac{1 - 1.1mss_{\text{shape}}^{-0.33} \tan^2 \theta}{mss_{\text{shape}}}$$

395 For Ku-band the  $mss_{\text{shape}}$  is generally smaller than the Ka-band value, in particular for wind speeds over 5 m/s, as shown in ??b. Computed variability of the wave slope velocity, the  $mss$  and the Doppler magnitude  $M_{WD}$  that is close to the ratio of these two quantities.  $M_{WD}$  was computed for a wide range of modeled ocean wave spectra, plotted here as a function of the wind speed. The colored curves show the median value for different classes of wave height for a given wind speed, each curve is separated by 0.5 m in (a) and (b) or 1 m in (c) and (d). spectrum, of which  $H_s$  is a proxy, definitely has to be accounted for.

400 Average values of the  $mss_{\text{shape}}$  give typical values  $G_D \simeq 25$ , slowly decreasing with increasing  $\theta$ . Therefore, both Stokes drift magnitude and  $G_D$  grow with windspeed. It may thus be more practical to express  $U_{WD}$  in Figure ??b, taken from (?), instead shows the dependence on wind speed and  $H_s$  of Ku- and Ka-bands effective mean squared slopes  $mss_{\text{shape}}$  retrieved from the GPM satellite measurements. The variability is even more strongly dominated by the dependence on wind speed, the variability due to the long wavelength part of the spectrum being much smaller. These measurements show very clearly the

405 filtering effect of the electromagnetic wavelength, and are a clear warning that equation (?), suggestive though it is, should be considered with caution.

Finally, figures ??c and ??d show the magnitude of the following form-

$$\begin{aligned} U_{WD}(\varphi) &\equiv \frac{M_{WD} \cos(\varphi - \varphi_{WD})}{\cos(\varphi - \varphi_S - \delta_\varphi)} \\ &\equiv \frac{(C_0 + \Delta_C) \cos(\varphi - \varphi_S - \delta_\varphi)}{\cos(\varphi - \varphi_S - \delta_\varphi)} \end{aligned}$$

410 where  $M_{WD}$  varies very little for most of the sea-state conditions, around  $C_0 = 2.2$  m/s in Ka-band and  $C_0 = 2.4$  m/s in Ku band horizontal  $U_{WD}$  component as a function of wind speed and  $H_s$ , estimated by numerically evaluating the integrals of equations (??) and (??) for  $C(\tau)$  and  $\partial_\tau C$  using the numerical tools of (?), on the basis of long-wavelength spectra extracted from global runs of the WAVEWATCH III model (?), completed in the high-wavenumber range by (?) spectral tails. The shading in the background represents the histogram of the different (wind speed,  $M_{WD}$ ) pairs. As could be hoped for, the

415 opposing influences of the wind speed on  $mss_{\text{shape}}$  and  $M_{WD}$  tend to counteract each others, greatly reducing the range of variability of  $M_{WD}$  with wind. This effect appears stronger in Ka- rather than Ku-band, possibly due to the saturation of the Ku-band  $mss_{\text{shape}}$  at high winds. These figures show a strong remaining impact of the long-wavelength waves, which clearly must be accounted for. As wind speed and significant height are highly correlated variables, the frequently encountered situations however fall in a quite narrow interval  $M_{WD} \simeq C_0$ , with  $C_0 \simeq 2.6 \text{ m.s}^{-1}$  and  $C_0 \simeq 2.2 \text{ m.s}^{-1}$  in Ku- and Ka-band,

420 respectively. In other words, most of the variability of  $U_{WD}$  is controlled by the directionality effect and the magnitude  $M_{WD}$  is a weakly varying function of the wave age and wind, of the wave age, and the presence of swell (see also ??).

A final remark is that, though these general patterns can probably be assumed robust, the precise numerical values depend on the parametric spectral shapes which have been used to fill the high-wavenumber range of the spectra. Changing for instance



the high-wavenumber azimuthal spreading functions, which are for the moment not very well constrained observationally, has different impacts on the  $m_s v_0$  and  $M_{ss}$  terms, and can thus be expected to marginally change the numbers.

### 2.3 Error Budget

Considering the errors on the different terms as independent, developing equation (1) allows one to derive the error variance of Doppler radar measurements of the TSCV as:

$$\text{Var}(\delta U_{CD}) = \left( \frac{U_{CD}}{\tan \theta} \right)^2 \text{Var}(\delta \theta) + \frac{\text{Var}(\delta V_{LOS})}{\sin^2 \theta} + \frac{\text{Var}(\delta V_{NG})}{\sin^2 \theta} + \text{Var}(\delta U_{WD}) \quad (18)$$

As a first step, four contributions to the uncertainty on  $U_{CD}$  can thus be isolated, with different origins:

- A first part corresponds merely to the error caused by the imperfect knowledge of the projection angle between the TSCV and the line of sight. Its order of magnitude is controlled by the TSCV, and it is thus negligible with respect to similar terms that involve the platform velocity.
- The second term corresponds to the random error in the DFS measurements, and subsumes the dependence on Signal-to-Noise Ratio, antenna beamwidth, orientation of the boresight with respect to the platform velocity vector and algorithmic choices. A very thorough analysis of this term can be found in (?). The standard deviation on the raw DV signal carries over to the end result, multiplied by a  $1/\sin \theta$  factor, of the order of 5 for  $\theta = 12^\circ$ .
- The third term corresponds to the error caused by mismatches between the actual platform motion contribution to  $V_{LOS}$  and the estimate computed from the ancillary sensors. The order of magnitude of this term is set by the (very large) platform velocity. It is by far the largest.
- The fourth and final term corresponds to the uncertainty on the Wave Doppler removal stage. Errors in the  $U_{WD}$  model carry directly over to the  $U_{CD}$  estimates.

The third term dominates the overall error budget, and must be further analyzed. It is convenient for that purpose to start from equation (??), which gives the expression of the beam direction vector, and use the platform velocity components in the local (North/East/Down) frame at the observation point. Neglecting terms involving the vertical velocity of the platform, and introducing the difference between the boresight and flight track azimuths  $\psi = \varphi_b - \varphi_t$ , one obtains the consolidated error budget as

$$\begin{aligned} \text{Var}(\delta U_{CD}) = & \frac{\text{Var}(\delta V_{LOS})}{\sin^2 \theta} + \text{Var}(\delta U_{WD}) + \frac{\text{Var}(\delta V_D)}{\tan^2(\theta)} \\ & + \text{Var}(\delta V_N) \cos^2(\phi_b) + \text{Var}(\delta V_E) \sin^2(\phi_b) \\ & + V_P^2 \left[ \frac{\cos^2(\psi)}{\tan^2(\theta)} \text{Var}(\delta \theta) + \sin^2(\psi) \text{Var}(\delta \varphi) \right]. \end{aligned} \quad (19)$$

This equation summarizes the dependence of the overall  $U_{CD}$  error on the errors introduced by the Doppler measurements, the  $U_{WD}$  model, the individual platform velocity components, and the incidence angle and azimuth mispointing errors.

**Table 2.** Standard deviations of the different error terms in equation (??) necessary to achieve a  $0.40\text{m}\cdot\text{s}^{-1}$  standard deviation for  $U_{CD}$ .

	KuROS 12°	KaRADOc 12°	SKIM 12°	SKIM 6°
$\delta V_{LOS}$ (m/s)	$3.1 \cdot 10^{-2}$	$3.1 \cdot 10^{-2}$	$3.1 \cdot 10^{-2}$	$1.6 \cdot 10^{-2}$
$\delta U_{WD}$ (m/s)	$15 \cdot 10^{-2}$	$15 \cdot 10^{-2}$	$15 \cdot 10^{-2}$	$15 \cdot 10^{-2}$
$\delta V_{NE}$ (m/s)	$15 \cdot 10^{-2}$	$15 \cdot 10^{-2}$	$15 \cdot 10^{-2}$	$15 \cdot 10^{-3}$
$\delta V_D$ (m/s)	$3.2 \cdot 10^{-2}$	$3.2 \cdot 10^{-2}$	$3.2 \cdot 10^{-2}$	$1.6 \cdot 10^{-2}$
$\delta\theta$ , up/down track (rad)	$0.26 \cdot 10^{-3}$	—	$4.5 \cdot 10^{-6}$	$2.3 \cdot 10^{-6}$
$\delta h$ , up/down track (m)	$17 \cdot 10^{-2}$	—	$80 \cdot 10^{-2}$	$20 \cdot 10^{-2}$
$\delta\phi$ , cross track (rad)	$1.2 \cdot 10^{-3}$	$1.2 \cdot 10^{-3}$	$21 \cdot 10^{-6}$	$21 \cdot 10^{-6}$

As an illustration, table (??) summarizes the requirements that have to be met to keep the standard deviation of each of the seven terms below  $0.15 \text{ m}\cdot\text{s}^{-1}$ , ensuring a  $0.4 \text{ m}\cdot\text{s}^{-1}$  standard deviation for  $U_{CD}$ . The requirement on  $\theta$  is translated to the corresponding altitude tracking accuracy requirement for the KuROS and SKIM configurations. The requirements on linear velocity components are stringent, but can be reached using current-day technology. The requirement on altitude accuracy is easily within the specifications of the SKIM nadir altimeter payload, but definitely out of reach of KuROS. The KuROS data could however be analysed in the cross-track looking configurations, where this requirement does not apply. The requirement on azimuthal pointing accuracy is by far the most stringent. In the airborne case, it is met for the antenna boresight by the plane IMU, allowing a straightforward analysis of the KaRADOc data. In the KuROS case, however, it is exceeded by a factor of ten by the mispointing induced by the azimuthal gradients of sea surface, which required the development of a specific data correction procedure. Finally, in the spaceborne case, it seems only achievable using a combination of high-end inertial measurements and data-driven analysis techniques.

### 3 Campaign overview

#### 3.1 Organization of the campaign

Given our objectives of demonstrating the sensitivity of airborne Doppler measurements to the geophysical contributions of currents and waves, it was important to have commonly accepted reference measurements for these parameters. Also, This section provides a general overview of the campaign. The location, timing and overall organization are described in section ??, the environmental conditions encountered during the campaign are described in section ??, and the two main instruments, the KuROS and KaRADOc airborne radars, are described in sections ?? and ??, respectively.

#### 3.1 Campaign organization

The Drift4SKIM experiment differs from previous airborne Doppler radar campaigns (??) in two important respects: in order to verify the limited-observe the effect of wave development on the geophysical Doppler velocity  $U_{GD}$ , we decided to go to an  $U_{GD}$ , it was performed in a midlatitude, eastern basin oceanic environment, open to offshore swells, which makes our experiment different from previous Doppler airborne campaigns (??). Also, given the campaign objectives of demonstrating the sensitivity of airborne radar Doppler measurements to the geophysical contributions of currents and waves, it comprised an extensive in-situ component designed to have commonly accepted reference measurements for these parameters.

Field work was focused in two "boxes" (performed in two areas (denoted by square boxes in Figure ??) named the "off-shore box", around area, centered on the "Trefle Trèfle" buoy (see below), and the "Keller race box" area, to the north of the Ushant island. Both boxes island of Ushant. Both locations are in the range of coverage of a WERA-type two-sites WERA (?) High-Frequency radar (??) system, operated by Service Hydrographique et Oceanographique de la Marine (Shom) and already used for several studies, in particular related to wave-current interactions (??).

The "Keller race box" is an area with very strong horizontal gradients of the current. Although it is easy to show a strong effect of the current on a measured Doppler the measured DFS, the spatial variability of the sea state is difficult to measure in situ, introducing uncertainties when combining  $U_{CD} + U_{WD}$  in a forward model or using  $U_{WD}$  estimates when retrieving  $U_{CD}$  from the measured  $U_{GD}$ .

The "offshore box" area, on the other hand, was chosen for its spatial uniformity, being located far enough from the islands and with a near-uniform depth of 110 m. Only airborne data acquired over the "offshore box" offshore area are presented in this paper.

The week around spring tides of November 2018 was targeted selected, in order to allow for a wide range of current speeds (Fig. ??a), as well as to accommodate plane availability constraints.

---

**Figure 6.** Location of the measurement campaign and in situ assets, including a map of the KaRADOC measurements of the Geophysical Doppler velocity  $U_{GD}$  acquired on November 22nd, 2018.

The KuROS and KaRADOC radars were installed on an ATR-42 plane operated by the French institutional scientific flight facility, SAFIRE, which is equipped with an AIRINS™ GNSS-FOG INS providing position, pitch, roll, heading information with stated tolerances of a few centimeters,  $0.005^\circ$ ,  $0.005^\circ$  and  $0.01^\circ$ , respectively.

Ground truth measurements comprised two permanent operational systems: the 12-MHz WERA-type HF radar HF radar system mentioned previously, with expected depth of measurement around 1 m (?), and a the "Pierres Noires" (WMO #62069) wave-measuring buoy 'Pierres Noires', also known by its World Meteorological Organization number 62069. Location of measurement campaign and in situ assets, including a map of KaRADOC measurements of the Doppler velocity acquired on 22 November 2019.

buoy. Dedicated instrumentation was also deployed for the campaign: -the "Trefle"-

- The “Trèfle” buoy was moored at 5°25'15" W, 48°25'15" N, in the middle of the offshore box at the center of the “offshore” area. This buoy monitored the surface motion current (?) and provided directional wave spectra (Fig. ??). ~~–two types of drifters-~~
- Several types of drifting buoys including CARTE drifters (?), drogued around 40 cm, and SVP drifters (?), drogued at 15 m, and “Spotter” wave-measuring buoys (?) were deployed in the measurement areas. ~~–the-~~
- The R/V Thalia worked in the offshore box, provided area, providing continuous underway measurements of meteorological parameters using a Météo-France “BATOS” operational system comprising a Vaisala WXT-series sonic anemometer located approximately 10 m above sea surface. The ship also carries-carried a SBE21 thermosalinograph.

In the summer, the so-called “Ushant tidal front” (?) has a strong influence on the current and surface currents, hydrographic (?) and atmospheric (?) conditions in the offshore box-area. This seasonal feature typically disappears in October, and CTD casts were performed from R/V Thalia during the campaign, that showed the water column to confirm that it had indeed vanished when the campaign took place. The water column was found to be very well mixed, with surface-to-bottom potential density anomalies being smaller than  $0.002 \text{ kg}\cdot\text{m}^{-3}$ . The spatial homogeneity was also checked using the ship thermosalinograph and an infrared camera mounted on a second plane (a Piper PA-23 also operated by SAFIRE) plane which surveyed the offshore box in a “lawn mowing” “offshore” area in a “lawn mowing” pattern, flying under the clouds from at an altitude of 500 m to 1000 m. Interesting-While small-scale surface signatures could be features were observed on calm days, but it is clear that no density-associated mesoscale structure was structures were present.

The aircraft measurement airborne radar measurements geometry over the “offshore box” consists “offshore” area consisted of relatively long (12 km) and straight tracks with different aircraft headings, forming a star pattern, with examples shown in Figures ??-as for the 2018/11/22 flight shown in figure ??. Tracks were flown every 12, 22.5 or 45° in azimuth, depending on flight duration constraints. Regarding the radar instruments, KaRADOC had its antenna-The KaRADOC antenna was fixed relative to the aircraft and looking to port, while the KuROS antenna could either be fixed in the uptrack or port cross-track directions, or rotate in the clock-wise clockwise sense relative to the flight line. Only the port-looking Doppler KuROS data are track. The KuROS Doppler data presented in this paper ~~–Tracks heading was every 12, 22.5 or 45° in azimuth  $\varphi$ , depending on flight duration constraints were acquired in the port-looking configuration.~~

### 3.2 Geophysical conditions

A wide range of geophysical conditions were encountered during the one-week-long campaign. The aircraft flew four times over the “offshore box”-one-week-long campaign. Four flights were performed over the “offshore” area, on 11/21 from 13:50 to 15:50, on 11/22 from 12:15 to 15:00, on 11/24 from 11:20 to 13:20, and finally on 11/26 from 09:40 to 11:00. In this paper, we focus on data acquired on 11/22 and 11/24 as the geophysical conditions were interesting and complementary (see below) and data were acquired with the largest azimuth diversity on these two days.

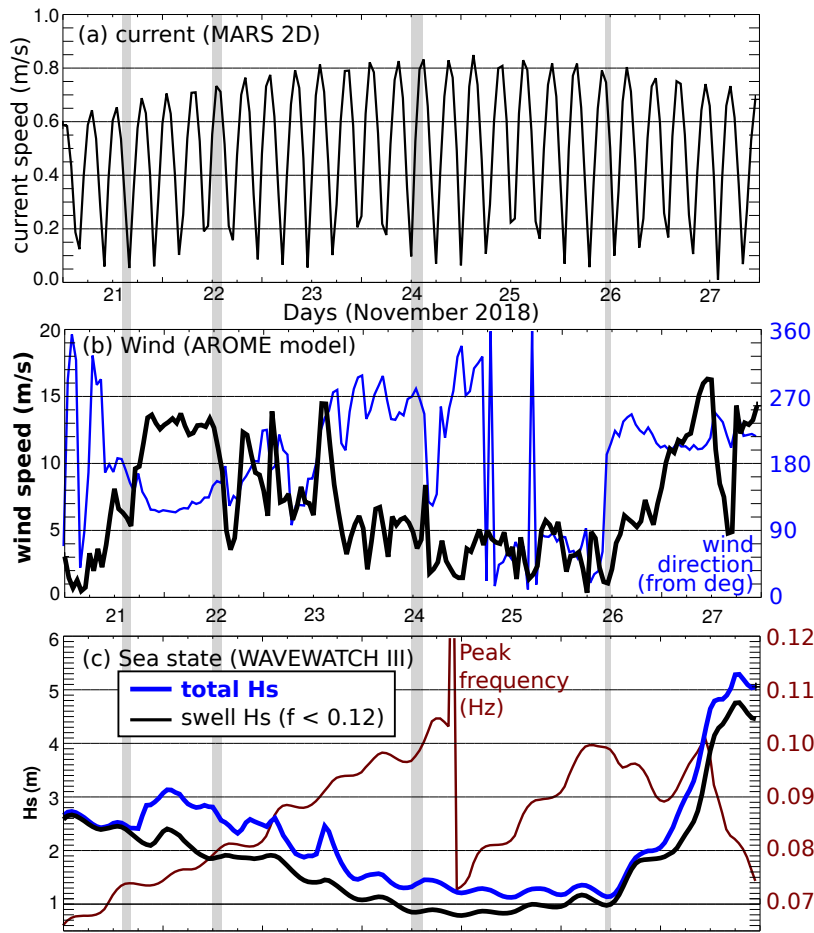


**Figure 7.** Time series at the location of the **Trefle-Trèfle** buoy ( $5^{\circ}15' \text{ W}$ ,  $48^{\circ}25'15' \text{ N}$ ) in the offshore **box-zone** of (a) ocean surface current speed **output** from the **MARS2D** numerical model **MARS2D-run at LOPS** (?); (b) wind speed (black) and direction (blue) from the **AROME** regional operational model **of-run by** MeteoFrance, **AROME** and (c) **Total-total** (blue) and swell (black) significant wave height and wave peak frequency (red) from the **WAVEWATCH III** numerical wave model **WAVEWATCH-III-run at LOPS** (?). The four time **frames-periods** shaded in grey correspond to the times of **fixed-antenna** KuROS measurements **with-fixed-antenna, with**. **The corresponding** observed environmental parameters **are** detailed in table ??.

The November **22-22nd** flight took place at the end of **an-interesting-a** steady southeasterly wind episode (13 m/s from  $140^{\circ}$ ). The November **24-24th** flight in contrast took place during a steady weak south-westerly wind period (5 m/s from  $270$ **225** $^{\circ}$ ) (Fig. ??b).

535 The wave height during the campaign was dominated by the presence of two swell systems from North Atlantic remote storms. The swell height decreased from 2.5 m on November 21st to 0.9 m **from-the-21-to-24-November-on-the-24th**, with a peak frequency increasing from 0.07 Hz to 0.1 Hz, and a mean direction gradually veering from **west-to-north-west** to **west**.

This swell ~~contributes little~~ has a small contribution to the Stokes drift (~~about~~, of the order of 10% of the windsea contribution on ~~22/11~~ November 22nd).

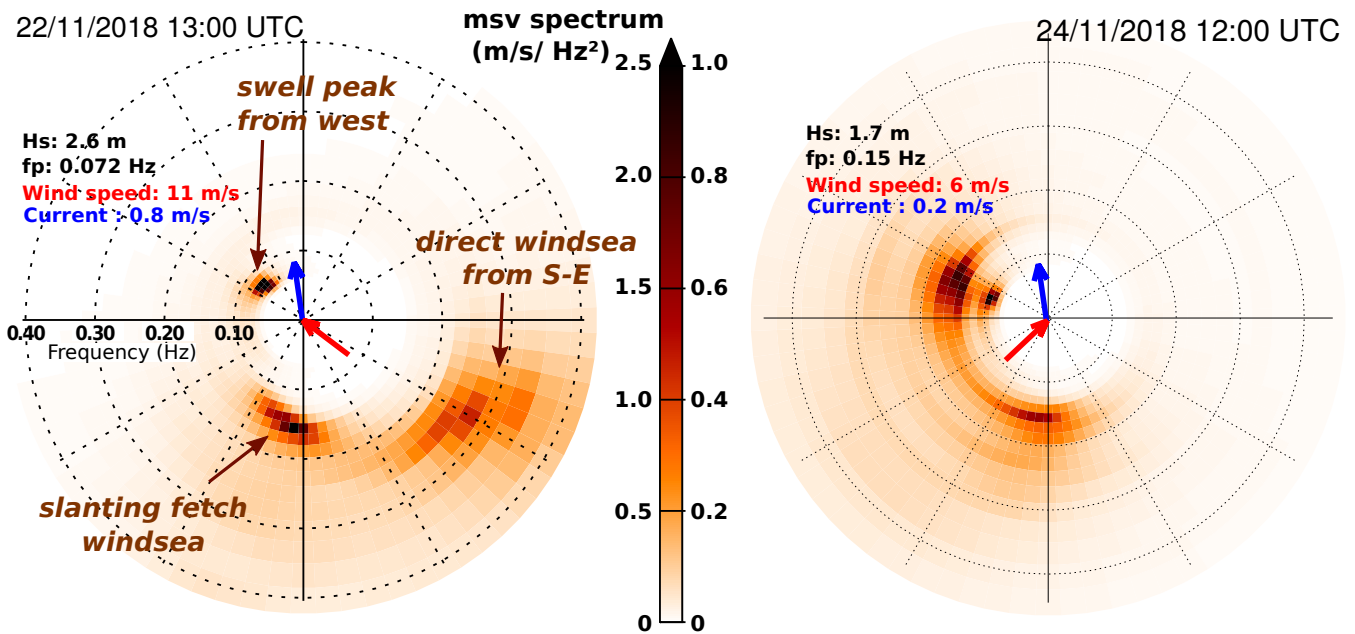


**Figure 8.** Directional wave spectra  $E(f_r, \theta)$ , where  $f_r$  is as functions of the relative wave frequency  $f_r$  and  $\theta$  is the incoming waves azimuth winds are coming from, estimated from the buoy motions of ~~Trefle~~ the Trèfle buoy on ~~22/11/22~~ at 13:00 UTC and Spotter buoy number 10 on ~~24/11/24~~ at 12:00 UTC. The measured directional moments were transformed with the Maximum Entropy Method (?), and Doppler shifted with  $f_r = f - \mathbf{k} \cdot \mathbf{U} / (2\pi)$  for the moored ~~Trefle~~ Trèfle buoy. The red and blue arrows represent the AROME wind and MARS2D surface current vectors directions, respectively.

540 The main environmental conditions at the time of these star-pattern flights ~~with a fixed antenna~~ are summarized in Table ??.

### 3.3 KuROS ~~set-up~~ instrument

KuROS is a Ku-Band (13.5 GHz) pulse pair Doppler radar with a dual antennae system and azimuthal scanning possibility, which was developed in the framework of the CFOSAT pre-launch studies. Of the two antennas, the Low Incidence (LI) antenna is nominally centered on 14° incidence angle, while the Medium Incidence antenna is nominally centered on 40° incidence angle. Only the LI antenna, which was the more relevant for SKIM, was used during the campaign. This antenna uses a HH polarization. A comprehensive description of the system can be found in ~~?~~ with an important modification consisting of a new antenna. A new antenna was used for the Drift4SKIM campaign, with characteristics given in Table 1.

550 The radar transmits a frequency-modulated pulse (chirp) with a 100 MHz ~~frequency-band~~ bandwidth, achieving a 1.5 m range resolution and an effective ~~resolution around ground-projected resolution of approximately~~ 7 m in elevation once projected on the ground m (at 12°). The 1-way 3-dB footprint in azimuth is 580 m wide at 12° and 3000 m flight altitude. The Pulse

**Table 3.** Velocities of current and Stokes drift measured or estimated near position [48.25-48°15' N, 5.255°15' W](#), in cm/s, and wind vector [components](#) in m/s. Please note that the Stokes drift is only integrated up to 0.5 Hz. Buoy data correspond to the [Trefle-Trefle](#) buoy for [22/11/22](#) and Spotter buoy number 10 for [24/11/24](#).

Time	CARTHE	SVP	HF-radar	buoy ( $U_s, V_s$ )	WW3 ( $U_s, V_s$ )	wind (ship)	wind (Arome)
<a href="#">21/11/21</a> 14:00	<a href="#">(21,73,18,72)</a>	(21,72)	<a href="#">(15,71,26,69)</a>	(0.69, 2.23)	(0.44,2.06)	<a href="#">(-3,3,8,0,0,0,7,3)</a>	(0.5,6.3)
<a href="#">21/11/21</a> 14:30	<a href="#">(17,59,58)</a>	(19,58)	<a href="#">(16,60,25,58)</a>	(0.88, 2.02)		<a href="#">(-2,3,6,8,4,3,6,9)</a>	-
<a href="#">21/11/21</a> 15:00	(15,45)	(16,49)	<a href="#">(12,39,17,41)</a>	(0.21 2.54)	(0.41,2.12)	<a href="#">(-4,4,5,2,4,5,5,0)</a>	(-1.1,5.8)
<a href="#">21/11/21</a> 15:30	<a href="#">(14,30,15,22)</a>	(15,21)	<a href="#">(11,31,16,26)</a>	(0.23, 1.97)		<a href="#">(-4,7,8,2,7,8)</a>	-
<a href="#">22/11/22</a> 12:00	<a href="#">(-5,107,2,73)</a>	(-3,81)	<a href="#">(-14,5,58)</a>	(-5.47,8.86)	(-7.38,11.55)	<a href="#">(-8,9,6,8,9,1,7,1)</a>	(-6.8,10.7)
<a href="#">22/11/22</a> 12:30	<a href="#">(-1,133,3,97)</a>	(4,84)	<a href="#">(-7,74,2,71)</a>	(-5.44,9.19)	(-7.42,11.37)	(-9,4,7,2)	-
<a href="#">22/11/22</a> 13:00	<a href="#">(3,97,6,102)</a>	(4,94)	<a href="#">(-5,89,7,84)</a>	(-4.72,8.37)	(-7.07,11.39)	<a href="#">(-8,5,7,9)</a>	(-5.2,10.0)
<a href="#">22/11/22</a> 13:30	<a href="#">(8,97,10,85)</a>	(12,89)	<a href="#">(3,91,14,88)</a>	(-4.75,8.02)	(-6.68,11.50)	<a href="#">(-4,4,9,2,4,5,9,1)</a>	-
<a href="#">22/11/22</a> 14:00	<a href="#">(12,94,9,82)</a>	(12,87)	<a href="#">(11,78,23,81)</a>	(-3.28,7.19)	(-6.35,11.66)	<a href="#">(-3,6,11,5,3,9,11,1)</a>	(-4.4,8.3)
<a href="#">22/11/22</a> 14:30	<a href="#">(11,87,10,78)</a>	(11,78)	<a href="#">(14,73,25,72)</a>	(-3.35,6.93)	(-5.82,11.76)	<a href="#">(-7,2,8,0,7,4,7,1)</a>	-
<a href="#">24/11/24</a> 11:30	<a href="#">(-8,-6,10,-2)</a>	(-11,-6)	-	(2.47,1.81)	-	<a href="#">(5,0,2,7,3,8,2,9)</a>	-
<a href="#">24/11/24</a> 12:00	<a href="#">(0,20,-6,19)</a>	(-7,16)	-	(2.49,1.20)	(0.75,2.92)	<a href="#">(4,0,3,9,3,8)</a>	(4.9,0.1)
<a href="#">24/11/24</a> 12:30	<a href="#">(1,44,-2,40)</a>	(-1,40)	-	(2.92,1.66)	(0.68,2.71)	<a href="#">(4,7,2,8,4,8,2,9)</a>	-
<a href="#">24/11/24</a> 13:00	<a href="#">(6,64,-1,60)</a>	(1,59)	-	(3.20,1.35)	(0.68,2.71)	<a href="#">(4,8,2,6,4,5,2,0)</a>	(3.5,-0.7)
<a href="#">24/11/24</a> 13:30	<a href="#">(8,82,-1,77)</a>	(2,78)	-	(2.73,1.29)	(0.70,2.60)	<a href="#">(3,3,3,4,2,8)</a>	-
<a href="#">26/11/26</a> 10:00	<a href="#">(-18,-86,-19,-83)</a>	(-20,-87)	<a href="#">(-11,-71,-25,-62)</a>	(0.46,-0.19)	(0.59,-0.64)	<a href="#">(-2,9,0,7,2,0,0,5)</a>	(-1.0,-0.6)
<a href="#">26/11/26</a> 10:30	<a href="#">(-23,-82,-22,-80)</a>	(-24,-84)	<a href="#">(-19,-71,-28,-63)</a>	(0.32,-0.23)	(0.59,-0.64)	<a href="#">(-0,7,-1,0,1,4)</a>	-
<a href="#">26/11/26</a> 11:00	<a href="#">(-25,-73,-20,-74)</a>	(-27,-74)	<a href="#">(-22,-77,-33,-66)</a>	(0.30,-0.20)	(0.59,-0.64)	(0.6,1.4)	(0.2,1.1)

Repetition Frequency (PRF=1/PRI) depends on the altitude, and is 23 kHz when the aircraft flies at 3000 m. The ambiguity on the Doppler velocity measurement (see section ?? in the [appendicesappendixes](#)) is about 126 m/s, which is much larger than expected from the measurements (below aircraft speed of 120 m/s).

555 [In order to reduce the thermal noise contribution, the range-resolved pulse-pair signal is coherently averaged in the instrument over 1 ms, corresponding to 22 pulse pairs per instrument sample. For the purpose of this article, this was further coherently averaged per blocks of 15 sample.](#)

As discussed in Appendix [????](#), accuracy requirements on observation geometry are much less stringent for cross-track than for up/down-track Doppler [velocity](#) observations. The Doppler [velocity](#) data discussed in this article were all collected with the KuROS antenna in the port-looking orientation. This configuration also ensures an overlap with the KaRADOC footprint.

560 ~~KuROS was operated with either a fixed antenna azimuth, looking left, or a rotating antenna which is the usual mode for wave spectrum measurement. For any given flight track, only one of these two modes of acquisition was used.~~

### 3.4 KaRADOc ~~sensor~~instrument

The Ka-band RADar for Ocean Current monitoring (KaRADOc) airborne radar sensor ~~has been~~was developed for the ~~DRIFT4SKIM~~Drift4SKIM campaign. KaRADOc is derived from the Still WAter Low Incidence Scattering (SWALIS) instrument, developed for the measurement of the NRCS of inland water surfaces in Ka-band. Further details on the system are given in Appendix ??.

KaRADOc was mounted under the ~~ATR42~~ATR-42 aircraft, in a port-looking configuration. The two-way 3 dB footprint from 3000 m altitude over a flat sea surface is an ellipse with diameters 45 and 60 m in the cross-track and along-track directions, respectively. The incidence angle is selected by varying the working frequency. Data ~~was~~were acquired at different incidence angles, from 6 to 14<sup>o</sup>, corresponding to a change of frequency from 32.5 to 38.2 GHz. ~~Here we only report on  $\theta = 12^{\circ}$  observations.~~This article focuses on the observations collected at  $\theta = 12^{\circ}$ , at 33.7 GHz.

~~This radar does not incorporate~~KaRADOc does not implement a range-resolution scheme: the transmitted pulses last several ~~ms~~ms, and the whole FOV is illuminated simultaneously. The demodulated return signal is sampled at 15 MHz and archived. It is essentially constant while the electromagnetic wave is actually interacting with the sea surface. The useful signal segment is selected and its average is computed in order to reduce the thermal noise contribution, yielding one complex amplitude for each pulse. Several hundred pulses are sent at 4 kHz PRF for each burst of measurements, with a burst repetition frequency of the order of 5 to 10 Hz, depending on the number of incidence angles in the scanning sequence. These parameters have been varied during the acquisitions. Though they have a strong impact on NRCS ~~estimates quality and Doppler estimates noise and~~DFS estimates quality, we have found the low-pass filtered ~~Doppler~~DFS signal to be robust.

The pulse pair complex signal is averaged for each burst, in order to reduce the effect of coherent speckle. One complex pulse-pair sample is thus obtained per burst. Even at the lowest burst repeat frequency of 5 Hz, the plane moves by less than a third of the FOV along-track extension between bursts.

The impact of the acquisition parameters on the KaRADOc measurements normalization is not yet fully understood, and the NRCS measurements could not be exploited in the scope of this study. The noise-filtered DFS measurements are however not affected by these normalization changes, and are valid.

## 4 Measurements

### 4.1 ~~Qualitative description of the KuROS data~~

#### 4.1 KuROS NRCS / DFS imagery

~~(A) and (C) Mosaic of radar intensity and Doppler acquired on November 22 with a fixed antenna relative to the aircraft, looking left. (B) overlay of the Doppler and intensity. Flight tracks are numbered 1 to 6, Black arrows indicate the flight direction and white arrow point into the radar look direction. The long dashed lines represent the apparent direction of swell crests. (D)-(E) are enlarged pieces of (A) and (C) for (D) and (E) a flight track that was now shown and (F)-(I) flight tracks 6~~



and 2. The 570 m scale bar applies to (E)-(H) and correspond to the 3-dB width of the radar beam at  $12^\circ$  incidence, i.e. near the middle of the swath.

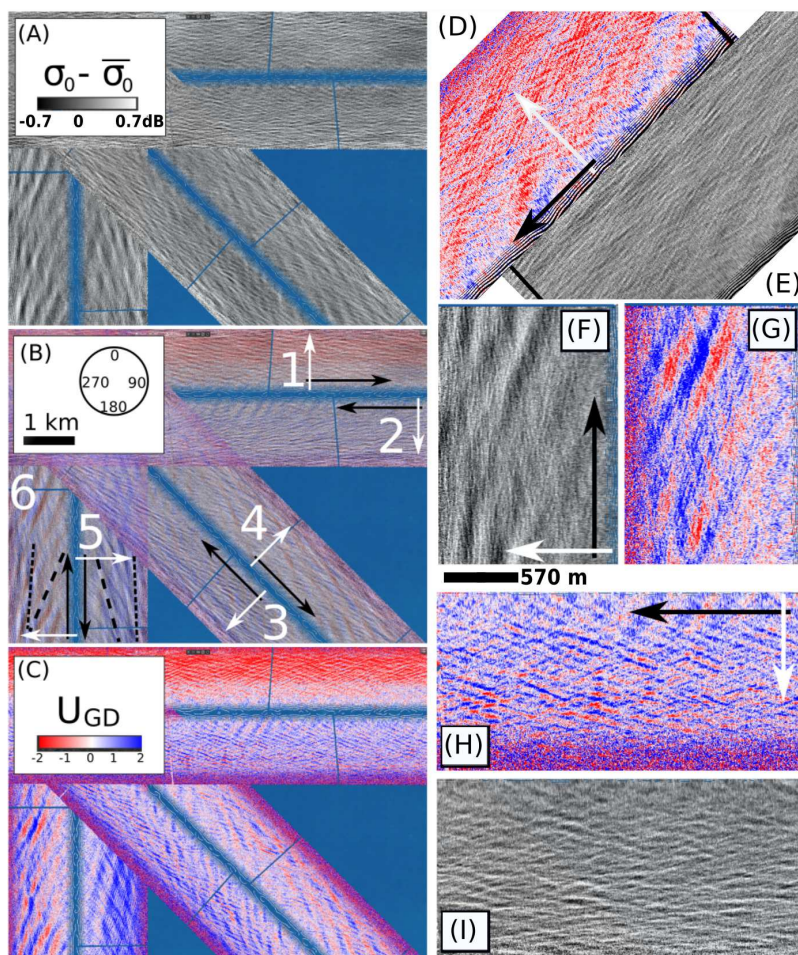


**Figure 9.** (A) and (C) Mosaics of KuROS backscattering intensity and Doppler velocity data acquired on November 22nd with fixed port-looking antenna. (B) overlay of the Doppler velocity and backscattering intensity. Flight tracks are numbered 1 to 6, black arrows indicate the flight direction and white arrows point in the radar look direction. The long dashed lines represent the apparent direction of swell crests. (D)-(I) are close-up views of selected tracks from (A) and (C). The tracks shown in (D) and (E) are out of the frame of (A) and (C). (F)-(I) show close-ups of flight tracks 6 and 2. The 570 m scale bar applies to (H)-(I) and correspond to the along-track 3-dB width of the radar beam at  $12^\circ$  incidence angle, i.e. near the middle of the swath. The mean trend of  $\sigma^0$  as a function of  $\theta$  has been removed from the  $\sigma^0$  data.

595 ~~We will start with the~~ The KuROS NRCS / DFS imagery reveals a host of interesting features, modulations and dependencies. An in-depth analysis of all these processes is clearly out of scope of this paper, and will be the subject of forthcoming contributions from the Drift4SKIM team. This section thus only provides a cursory description of a few segments of  $\sigma^0$

600 data because it is a more generally understood property of the sea surface and the analysis of its variation in azimuth  $\varphi$  and elevation  $\theta$  is necessary to interpret the Doppler mean value and modulations. However, it is interesting to first look at the rawest available data, which can be displayed as images of backscatter and Doppler.

Figure ?? shows pieces of the first few tracks acquired on November 22 and DV data collected on November 22nd, 2018, when the wind speed was around approximately 11 m/s, after removing the aircraft velocity (see Appendix B and C for details)  $\text{m.s}^{-1}$ , which are displayed in figure ??.

605 The first remark is that the back-scatter, after correcting for an incidence-varying mean trend, is smooth NRCS is smooth, with a typical amplitude of variation modulation depth of 1 dB after removing its mean trend as a function of incidence angle (Fig. ??A). This smoothness comes from is in part due to the large footprint and, but also shows that the radiometric quality of the data and the coherent averaging performed are sufficient to control the thermal noise. Speckle noise is however still present, with different statistics depending on the radar look direction and the variable considered (not shown). The cross-track observation geometry leads to the best speckle noise reduction for the NRCS, but to the worst-case speckle noise statistics for the DV.

610 The KuROS data clearly reveals the presence of the swell from the west, show a modulation, both in NRCS and  $U_{GD}$ , associated to the north-westerly swell observed by the Trèfle buoy with a peak frequency of 0.07 Hz, corresponding to a wavelength  $L = 320$  m (Fig. ??). This is particularly visible in on the north-south oriented flight tracks number 6 and numbered 5 and 6 in Fig. ??B and Fig (see also Figs. ??E-F-F-G for a zoom on track 6-6). The apparent swell crests direction (dashed lines in figure ??B) differs from its the true direction due to scanning distortion the scanning distortion effect (??), as the swell propagates during the measurement measurements at a phase speed of 22 m/s, combined with an aircraft speed of while the aircraft moves at 120 m/s.

620 Shorter waves, as The shorter waves measured by the TREFLE buoy (and also the Pierre Noire buoy, not shown), Trèfle buoy (Fig. ??) occupy a wide range of directions from a narrow windsea peak from the south at 0.16 Hz ( $L = 60$  m), to a broad directional distribution at 0.22 Hz ( $L = 30$  m) with a mean direction of  $130^\circ$  and a half width (spread) of  $45^\circ$ , hence covering directions from  $85^\circ$  to  $175^\circ$ . These shorter components are present in the data from flights tracks 5 and 6, in the form of very narrow stripes with orientations shown with the short dashed lines in ??B and Fig (see also Figs. ??E-F-F-G for a zoom on track 6-6). The "long-crested" appearance of the short waves in (D) and (E) is an artefact of due to the wavefront-matching observation geometry (?), with all other directions averaged out by the large azimuth width of the radar beam. If purely geophysical, the velocity associated to the Doppler shifts phase relationship between the DV and NRCS modulations is expected to give the wave propagation direction. For flight track 6 in (F) and (G), the long swell propagates towards the radar and the brighter slopes (white) correspond to eastward velocities toward the radar (blue). This will be discussed in further details below. Finally (H) and (I) exhibit chevron patterns with crests facing both north-east and north-west directions, whereas . Whereas the waves from the south-west are expected to be much longer than those from the south-east, which this is not apparent in the KuROS data.

#### 4.2 Ku-band backscatter NRCS

Given the expected large influence of the wind, wave and current directions, and the high noise on the aircraft measurement geometry estimation, data have been averaged along 30-s track portions. Data have been averaged in incidence angle (across track) every  $1^\circ$ . In this section we discuss the dependence of the Ku-band NRCS as a function of azimuth and incidence angle, for the November 22nd and November 24th cases. The fixed-antenna as well as the rotating-antenna data are presented. In order to reduce the dispersion introduced by the short-scale modulating processes discussed above, the data were averaged per  $1^\circ$  with one point every 30 s. As highlighted, incidence angle and azimuth bins. As mentioned before, full tracks are straight and relatively long (12 km) in a, and view a mainly homogeneous ocean region. Each track has a different aircraft heading. For the fixed-antenna observations, azimuthal diversity is obtained by performing tracks in different flight directions, forming a "star" pattern, sampling a wide range of azimuths "star" pattern.

The variation of  $\sigma^0$  in variations of the Ku-band is shown for 22 November  $\sigma^0$  are shown for November 22nd in Fig. ??, with one dot for each 30-s long record. These measurements follows the expected azimuthal modulation show the expected modulation of 0.8 to 0.9 dB with azimuth, with a downwind-crosswind contrast that increases from low to high with the incidence angle. This contrast is larger for the higher winds of 22 November. The Upwind-downwind November 22nd. The upwind-downwind asymmetry is expected from the wave asymmetry behavior of the surface slope probability density function (??). The exception are the  $\sigma^0$  values for the flight tracks with a fixed antenna around the azimuths 90 and 270 (Fig. ??A), which have anomalous normalized values between 1 and 1.3 instead of expected values much much closer to 1. We have no explanation yet for this anomaly, which is genuine. No such anomaly was found with the subsequent flight tracks of for the rotating antenna data collected later on the same day in which the antenna was rotated (Fig. ??B).

Discarding these azimuths azimuth ranges (shaded in grey in figure ??C), we fitted a functional variation of the the data could be well fitted with a functional form  $a_0 + a_1 \cos(\varphi - \varphi_{\sigma,1}) + a_2 \cos[2(\varphi - \varphi_{\sigma,2})]$ . As explained in section 2.1, ??, measuring this azimuthal variation is critical for the interpretation of the mean Doppler velocity due to the spurious azimuth gradient Doppler velocity contribution. As expected, the fitted directions  $\varphi_{\sigma,1}$  and  $\varphi_{\sigma,2}$  are very close to the wind direction, except for the lowest incidence angles for which the contrast is less than 0.05 dB.

On November 24th, the  $\sigma^0$  azimuthal contrast was much weaker (Fig. ??) was much more uniform with azimuths, due to the much lower wind speed, and was actually not aligned with the wind direction when the measurements were performed.

### 4.3 Mean Doppler Velocity from KaRADOC

We now discuss quantitatively the measured Doppler signal, and the main question is: do we understand the measurements? In other words: does the velocity signal, in order to assess the agreement of our theory of the wave-induced Doppler contribution  $U_{WD}$  agree with the measurements?

Starting with KaRADOC, This section is focused on the KaRADOC data, which are easier to interpret than KuROS thanks to its narrower beam, we first examine the consistency of all the data acquired at an incidence the KuROS data due to the narrower radar beam of the instrument.

We have presented in figure ?? the low-pass filtered  $U_{GD}$  estimates retrieved from the  $12^\circ$ . ~~Figure ?? contains all the mean Doppler measurements represented with an offset, with blue lines, from  $0^\circ$  incidence angle KaRADOC data collected on November 22nd between 12:13 and 12:59 (TU).~~

This representation is misleading, as much of the observed variability is in fact due to the effect of the flight track orientation. For instance, the largest contrast can be observed between the northeastward- and southwestward-directed flight tracks, even though to a first approximation a mere change in observation direction has occurred.

Another representation of the same data is proposed in figure ?. In this figure the  $U_{GD}$  data are represented as blue lines shifted to the right of the plane ground track (black lines). ~~If the Doppler were the radial projection of a fixed vector, then all the blue lines would be straight, crossing at a single point. For November 22 in black) by an amount proportional to the instantaneous low-pass filtered  $U_{GD}$  value. This representation removes the trivial effect of observation direction changes, and allows subtler effects to be better appreciated. For instance, noise-free observations of a constant vector  $U_{GD}$  would appear as straight lines parallel to the flight tracks, all crossing at the tip of the vector. Deviations from this behaviour, such as can be observed in figure ?, are indicative of measurement noise, of geophysical variability, or of geophysical phenomena not accounted for by our theory.~~

For November 22nd, 16 flight tracks are available, ~~and 17 for November 24, collected from 12:13 to 12:59 (TU), and for November 24th 17 tracks were collected from to 11:27 to 13:13 (TU). Some tracks were repeated (on November 22:  $10^\circ$ ,  $90^\circ$ ,  $130^\circ$ ,  $320^\circ$ ) with differences of the mean Doppler that are as large as 80 cm/s in the case of  $320^\circ$ .~~

Overall, the assumption of a constant vector is good to within 0.3 m/s. It is particularly striking that the three horizontal lines in figure ?.A are almost perfectly aligned, corresponding to 2 flight tracks looking into azimuth  $0^\circ$  and one flight into azimuth  $180^\circ$ . On November 22nd, the largest ~~uncertainty dispersion~~ is for the  $315^\circ$  and  $135^\circ$  azimuths for which a total of 4 tracks are available with very different values ~~that are, that are however~~ consistent along each track.

Now using the average ~~value for each track values from the different tracks~~, we compare the measured Doppler velocity to the forward model given by eq. equation (1), with  $U_{WD}$  estimated from the in situ wave buoy data using the ~~model of ? tools discussed in section ??.~~ The method combines the buoy spectrum up to 0.40.35 Hz and adds a high frequency tail based on ~~the ? spectrum, then computes numerically the integrals of equations (??) and (??) to obtain the DFS estimate. The TSCV contribution, as detailed in ?. The current contribution~~  $U_{CD}$ , is taken to be the drift velocity of the nearest CARTE drifter, which is uniform to within 3 cm/s in the Offshore ~~box (The following link provides an interactive animation area (Interactive animations~~ of all deployments and trajectories ~~can be found at~~ <https://odl.bzh/eVRHv1TE>).

Figure ? shows the measured mean Doppler ~~velocity~~ and standard deviation for each track ~~(the standard deviation is representative of the order of magnitude of the short-scale modulations due to waves, not of the error bar on the mean DV).~~ On November 22nd (Fig. ?.A), the current vector accounts for less than half of the observed magnitude of  $U_{GD}$  and it is interesting that the maximum Doppler velocity is from azimuth ~~144~~  $147^\circ$ , in between the wind direction ( $130^\circ$   $128^\circ$ ) and the ~~current direction (182<sup>o</sup> up-current direction (183<sup>o</sup>)).~~ The direction of the modeled and measured  $U_{GD}$  are within  $5^\circ$  of each other.

Compared to the relatively high wind condition on November 22<sup>nd</sup>, it is interesting to discuss the results for November 24<sup>th</sup> (Fig. ??B), with a wind speed of 65.5 m/s instead of 11 m/s. The amplitude of the Doppler velocity are is not much reduced, in spite of a more than halved current and Stokes drift. This is consistent with the expected near-constant value  $C_0$  of the wave Doppler velocity magnitude, and this is the main result of the present paper.

~~Looking in details, we find that the model gives larger values of  $U_{GD}$  than what is observed for both days. An ad hoc reduction of  $U_{WD}$  by 10% gives the best agreement between model and data. With such a reduction, the surface current vector is accurately inverted from the data, when  $U_{WD}$  is subtracted off the fitted  $U_{GD}$ , as shown in figure ??.~~

The reason for the 10% model overestimation is not clear, and it may be due to a particular processing of the airborne data or assumptions in the model. This second hypothesis was tested by varying the method for estimating  $U_{WD}$ . Table ?? gives a subset of model tests with varying the exact input spectrum. The process leading to the estimation of the constant  $C_0$  is however dependent on a number of assumptions: the directional wave spectrum must be evaluated from the buoy data, then matched to a parametric spectral shape before the necessary numerical integrations can be performed. The (?) spectral shape we have used depends on the wind speed and direction, but also on a wave age parameter,  $\Omega$ , equal to 0.84 for equilibrium seas.

Table ?? summarizes a subset of the extensive tests we have performed to check the sensitivities of this process. It is clear from this table that changing drastically the wind speed, as occurred between the two days, affects more the magnitude of the computed  $U_{WD}$  at Ku-band than Ka-band, but not in a catastrophic way, and that the wave age parameter  $\Omega$  can also be varied over its meaningful range quite freely. We have also checked that the transition frequency at which the spectral tail is matched to the observational data is not a very sensitive parameter, provided it is taken low enough for the buoy data to be of good quality where they are kept.

Extracting directional wave spectra from buoy data, however, is a quite intricate and subjective step. Several methods have been developed over the years to this end, each with pros and cons (see ?, for a review). Two of the best-established methods are the Maximum Entropy Method (MEM) and the Maximum Likelihood Method (MLM). The MEM is a parametric method which assumes a specific form of the directional spreading function. In each frequency band, the parameters of the spreading function are chosen such that the first moments of the azimuthal Fourier spectrum match the buoy-derived ones. The MLM is a non-parametric method akin to the Capon beamformer. In terms of directional moments measured by buoys, the MEM estimates provide spectra that fit exactly the measured moments, while the MLM produces spectra that have directional spreads larger than those obtained directly from the measured moments. However, it is not clear how they compare on other properties of the spectrum that may be relevant to the mean slope velocity. Comparing results obtained with these two methods was thus a convenient way to test the sensitivity of  $U_{WD}$  to the sea state directional spread.

The largest differences, of the order of 10%, were found when changing the transition frequency from 0.35 to 0.5 Hz with a general increase of the simulated  $U_{WD}$  values. This can be interpreted as the effect of the directional distribution in As table ?? shows, using one technique or the other to estimate the resolved part of the waves directional spectrum does induce significant differences in the simulated  $U_{WD}$  values, showing that the azimuthal width of the spectrum, which is currently not very well constrained observationally, is a sensitive factor. The values obtained using the broader MLM spectrum are consistently

**Table 4.** Modeled wave Doppler velocity amplitude  $M_{WD}$  and direction  $\varphi_{WD}$  at Ku- and Ka-band, using the same input directional wave spectra but varying the transition frequency  $f_t$  between the buoy spectrum and a ? spectrum for produced using the high frequencies Maximum Entropy or Maximum Likelihood Methods, and varying the wave age parameter  $\Omega$  for this of the ? high frequency spectrum frequencies spectral tail. Removing-In all cases the swell from transition frequency between the input wave data and the high-frequency spectrum was also tested. Default values use is  $f_t = 0.35$  Hz and  $\Omega = 0.83$ . All values are estimated for an incidence angle  $\theta = 12^\circ$   $\theta = 12^\circ$ .

	Ka-band	Ku-band
11/22, 12:00 UTC	$M_{WD}$ (m/s) / $\varphi_{WD}$ ( $^\circ$ )	
<del>wave spectrum band MEM, <math>\Omega = 0.84</math></del>	<del><math>M_{WD}</math> (m.2.21 / s) <math>\varphi_{WD}</math> default Ka 2.24 / 136.7<math>^\circ</math></del>	<del>128.8 2.83 / 136.7</del>
<del>MEM, <math>\Omega = 1.3</math></del>	<del>Ka 2.24 / 2.21 / 136.8<math>^\circ</math></del>	<del>128.8 2.83 / 137.1</del>
<del>MEM, <math>\Omega = 2.5</math></del>	<del>Ka 2.23 128.4 <math>f_t = 0.5</math> Hz Ka 2.43 127.5 <math>f_t = 0.5</math> Hz, no swell Ka 2.54 2.20 / 136.8<math>^\circ</math></del>	<del>127.5 2.79 / 137.1</del>
22/	$M_{WD}$ (m/s) / $\varphi_{WD}$ ( $^\circ$ )	
<del>default Ku MLM, <math>\Omega = 0.84</math></del>	<del>2.83 1.97 / 135.1<math>^\circ</math></del>	<del>128.7 2.54 / 135.1</del>
<del>MLM, <math>\Omega = 1.3</math></del>	<del>Ku 2.83 1.97 / 135.2<math>^\circ</math></del>	<del>128.5 2.53 / 135.2</del>
<del>MLM, <math>\Omega = 2.5</math></del>	<del>Ku 2.80 128.1 <math>f_t = 0.5</math> Hz Ku 2.97 129.2 <math>f_t = 0.5</math> Hz, no swell Ku 3.11 1.96 / 135.2<math>^\circ</math></del>	<del>129.2 2.51 / 135.2</del>
24/11/24, 12:00 UTC	$M_{WD}$ (m/s) / $\varphi_{WD}$ ( $^\circ$ )	
<del>default Ka MEM, <math>\Omega = 0.84</math></del>	<del>2.30 2.25 / 235.7</del>	<del>221.5 2.50 / 235.7</del>
<del><math>\Omega = 1.9</math> Ka MEM, <math>\Omega = 1.3</math></del>	<del>2.26 2.24 / 236.3</del>	<del>209.9 2.49 / 236.3</del>
<del>MEM, <math>\Omega = 2.5</math></del>	<del>Ka 2.21 208.8 <math>f_t = 0.5</math> Hz Ka 2.26 2.17 / 237.7</del>	<del>207.6 2.40 / 237.7</del>
<del>default Ku MLM, <math>\Omega = 0.84</math></del>	<del>2.56 2.07 / 234.3</del>	<del>211.4 2.29 / 234.3</del>
<del><math>\Omega = 1.9</math> Ku MLM, <math>\Omega = 1.3</math></del>	<del>2.51 2.05 / 234.8</del>	<del>209.5 2.28 / 234.8</del>
<del>MLM, <math>\Omega = 2.5</math></del>	<del>Ku 2.45 208.4 <math>f_t = 0.5</math> Hz Ku 2.51 1.99 / 236.2</del>	<del>207.6 2.19 / 236.2</del>

smaller than those obtained using the MEM spectrum. A broader azimuthal distribution only redistributes the weight between the different  $M_{ss}$  components, but reduces the contributions composing the  $m_{sv_0}$  vector.

735 The results obtained using both methods are shown in figure ?? as light green and dark green lines. It appears that the MLM processing of the buoy data gives the best fit to the radar  $U_{GD}$ , showing that the directional spread of the sea state should not be taken too low. The possibility that the directional distribution of the ? spectrum that is probably could be slightly too narrow for intermediate wavelengths 2-10 m. This effect was discussed for very was for instance discussed in specific cases by ? and it is. It is however not yet clear if it is specific to the very young wind seas they observed, although it could also explain some properties of L-band backscatter (?). Other effects, in particular the non-linearity of the waves (e.g. ??) may also contribute a  
740 few percent to the deviation of mean Doppler. The MLM was used to process the Trèfle data in the rest of this study.

While testing different model settings for  $U_{WD}$ , we also estimated the importance of the swell. Although the swell has a limited contribution to Conversely, figure ?? illustrates the use of the mean square slope, in the present case it contains 6% of the zonal Stokes drift component  $V_s$ . When projected on the Doppler velocity direction, this explains the increase by 4%

of  $U_{WD}$  when the swell is removed in table ?? because the swell contribution is in the direction opposite to the wind sea and thus reduces  $U_s$  and  $U_{WD}$  (see also ?). This is more easily understood by looking at the contribution of the different spectral components to  $U_s$ . In practice,  $U_s(\varphi)$  is the projection of the horizontal vector  $(U_s, V_s)$  in direction  $\varphi$  and can be obtained from the heave spectrum  $E(k)$  of the sea surface and the first directional moments  $a_1(k)$  and  $b_1(k)$ , or the associated mean direction  $\varphi_1(k)$  DV data for the retrieval of the surface current vector, by subtraction of  $U_{WD}$  from the fitted  $U_{GD}$ . The norm of the difference between the in-situ measured and remotely sensed  $U_{GD}$  vectors is less than 20 cm/s on both days, which is the direction of the vector  $(a_1(k), b_1(k))$  and spread  $\sigma_1(k)$  (?), that can be measured from drifting wave buoys,

$$\sigma_1(k) = \sqrt{2(1 - \sqrt{a_1^2(k) + b_1^2(k)})}$$

Using the dispersion relation for linear surface gravity waves in deep water,  $\sigma^2 = gk$  with  $g$  the acceleration of gravity, the Stokes drift contribution at each wavenumber is given by the following spectrum (?),

$$(F_x, F_y) = k\sqrt{k/g}(1 - 0.5\sigma_1^2)(\cos \varphi_1, \sin \varphi_1)E(k),$$

755 which integrates to

$$(U_s, V_s) = \int_0^\infty (F_x, F_y) dk.$$

significant, but quite satisfying at such an early stage of the technique, especially taking into account the fact that geophysical variability due to time variations of wind and tidal current occurred over the several hours of the flight.

760 Figure ?? shows example of these spectra in the case of November 22, with a 2-m swell from the west, giving positive contributions to  $F_x$  for frequencies under 0.1 Hz (wavelengths larger than 150 m), and a wind-sea from the south-east, giving positive contributions to  $F_y$  and negative contributions to  $F_x$ .

#### 4.4 Mean Doppler velocity from KuROS

Although the wind-sea energy is much less than that of the swell, its contribution, weighted by  $k^{1.5} \propto f^3$  is much larger.

#### 4.5 Mean Doppler from KuROS

765 Now looking at Due to the much broader radiation diagram of the KuROS antenna, analysing the Ku-band data from KUROS, it is necessary to compute the NRCS azimuth gradient Doppler spurious velocity  $U_{AGD}$  requires significantly more effort, as the  $U_{AGD}$  spurious velocity contribution due to the azimuthal variation of  $\sigma^0$  across the KuROS wide antenna beam, as given by eq. (??). In practice we use a bi-harmonic form of  $\sigma^0$  fitted to the measurements (Fig. ??) to compute  $U_{AGD}$ . As shown in Fig. ??, A,B, removing  $U_{AGD}$  reduces the maximum average velocities (from 4 to 3 m/s) that correspond to the red colors in Fig. ??, D. 30-s average Doppler velocity (red dots, grey bars are  $\pm 1$  standard deviation for a track) for the star-pattern flight of 770 22 November, (A) before correction of  $U_{AGD}$  for  $\theta = 12^\circ$ , (B) after correction of  $U_{AGD}$  for  $\theta = 12^\circ$  and (C) after correction of

$U_{AGD}$  for  $\theta = 18^\circ$ . For the lower two panels, two fits are shown with a single cosine function and with a cosine and harmonic, as well as the expected signature of the current vector measured with CARTHE drifters (dark blue), the theoretical signature of the waves (light blue), the sum of the two (light green) and the sum with a 10% reduced  $U_{WD}$  (dark green).

775 Still the measured Doppler velocities do not fit very well the forward model, in particular for the azimuths 210 to 300 degrees. The fit is still poor but relatively better at higher incidence angles, with  $18^\circ$  shown in Fig. ??C. Given the lower importance of antenna lobe effects for higher incidences, it is quite possible that the mean Doppler deviations from the model are partly due to errors in the antenna pattern.

780 Another issue is the general magnitude of the measured  $U_{GD}$  that is smaller with KuROS compared to KaRADOC, whereas theory would suggest the contrary. In particular, the wave Doppler, in a first approximation is ratio of the wave Stokes drift and the effective mean square slope  $mss_{shape}$  as defined by ?. With the known reduction of  $mss_{shape}$  from Ka to Ku band, this should lead to a higher value of  $U_{WD}$  and thus  $U_{GD}$ . The KuROS data thus appear anomalous.

785 As a result, any attempt to retrieve surface current vectors from KuROS is not very successful for most incidence angles, as shown in Figure ?? for  $\theta = 12^\circ$  FOV discussed in section ?? must be compensated for. The DV measurements, corrected for the  $U_{NG}$  platform motion contribution but not for the  $U_{AGD}$  contribution, are represented in figure ?? by the red dots, while the green line represents the projection along the line-of-sight azimuth of the sum of the TSCV and the MLM-derived  $U_{WD}$  vectors. The difference is clearly very large, reaching  $2 \text{ m.s}^{-1}$  in places, on November 22nd, and smaller on November 24th as the azimuthal modulation of the radar NRCS is much weaker.

790 The amplitude of the Doppler velocity are not much reduced, in spite of a more than halved current and Stokes drift. This is consistent with the expected near-constant value  $C_0$  of the wave Doppler magnitude. We also note that the upwind/downwind asymmetry of the Doppler is much reduced. Introducing the fits to the Ku-band NRCS data discussed in section ?? in equation (??) allows one to produce the corrected data represented by the magenta dots, which are in much better agreement with the green line (though a constant offset is apparent on the November 24th data, which is rejected by the cosine-fit procedure). Figure ?? summarizes then the  $U_{CD}$  retrieval operation in vector form (the magenta arrow represents only the first azimuthal harmonic component of the  $U_{AGD}$  correction). The norm of the difference between the in-situ (in grey) and remote-sensed (in blue) estimates of the TSCV is of the order of  $0.5 \text{ m.s}^{-1}$  on November 22nd, and of the order of  $0.2 \text{ m.s}^{-1}$  on November 24th. Again, these numbers, though admittedly not small, can be considered encouraging given the number of very large corrections applied to the data and the fact that the instrument had definitely not been designed for this purpose.

#### 4.5 Observed Doppler velocity modulations

800 A simplified vector interpretation of the measured Doppler is shown in Fig. ?. It shows large differences, of the order of 50 to 100 cm/s between the KuROS estimates and the in situ measurements.

#### 4.6 Observed Doppler modulations

In spite of issues related to the insufficient knowledge of the antenna pattern for a retrieval of the mean Doppler velocity, the KuROS measurement are very interesting. The range-resolution scheme implemented in KuROS makes it a very interesting



805 instrument for the analysis of ~~the small-scale velocity gradients~~ DFS and NRCS modulations. In particular, ~~?,~~ with a different antenna (slightly narrower beam) ~~had successfully used the cross-spectra of Doppler~~ have attempted to use the cross-spectrum of the DFS and NRCS to resolve the  $180^\circ$  ambiguity in the wave propagation direction. ~~Also, an alternative to the theoretical model for  $U_{WD}$  used above, it may be possible to use the resolved part of the~~ In the SKIM context, analysing the contribution of the resolved scales to the correlation between  $\sigma^0$  and ~~Doppler~~ the DFS could permit the development of empirical methods to estimate the unresolved part and ~~the full  $U_{GD}$~~  provide estimates of  $U_{WD}$ .

In practice ~~the Doppler modulations are,~~ with the antenna used for the Drift4SKIM flights, another contribution to the DFS modulations is also caused by the gradients of  $\sigma^0$  and the speed of the aircraft, just like the mean spurious  $U_{AGD}$  velocity. ~~These~~ Brighter areas in the field of view tend to influence strongly the DFS signal towards positive values if they are located to the front of the aircraft, and negative values if they are located aft of the aircraft.

815 As a test of this, simulations were performed with the Radar Sensing Satellite Simulator (?), which are illustrated in Figure ??. The amplitude of the spurious modulations are enhanced by 70% when the antenna ~~pattern diagram~~ is made 50% wider in azimuth, ~~as illustrated in Figure ??.~~ With typical variations of  $\sigma^0$  up to 1 dB over scales of the order of 1 km (e.g. Fig. ??), the variation of  $\sigma^0$  with azimuth  $\varphi$  is roughly proportional to  $1/\sin\theta$  giving a  $U_{AGD}$  that does not vary much with  $\theta$ , of the order of 1.5 m/s. This spurious velocity is larger than the 0.5 m/s significant orbital velocity of the swell. As a result the phase relation  
820 between ~~Doppler-DFS~~ and  $\sigma^0$  can change sign as a function of azimuth, due to the combination of two imaging mechanisms with comparable magnitudes and possibly opposite signs.

~~Qualitative validation of radar imaging mechanism in R3S simulations. Both the real data and simulation contain the geophysical modulation of velocities associated to surface velocities and slopes in the look direction (part of  $U_{GD}$ ) and aircraft velocities and slopes in the flight direction (part of  $U_{AGD}$ ). Note that the wave phases in the R3S simulation are random and cannot be expected to match those in the data or between the two simulations.~~ This effect will be weaker for shorter (wind sea) components as soon as the wavelength and crest length becomes much shorter than the KuROS footprint  $L_y$ , as given by eq. (??): for a given  $\sigma^0$  contrast, the gradient increases linearly as the scale  $L$  is reduced, but the  $U_{AGD}$  for a given gradient is reduced exponentially in  $-L_y/L$ .

## 5 Implications for SKIM

830 The use of two Doppler ~~radar~~ radars, in Ka and Ku band, using the same pulse-pair technique but ~~very different antenna patterns~~ antennas with very different radiation diagrams, has provided important insight for the preparation of the SKIM mission.

~~In terms of radar measurement, the DRIF4SKIM~~ Regarding radar measurements, the Drift4SKIM campaign clearly demonstrated the ~~robustness of the feasibility of the TSCV~~ retrieval approach proposed for SKIM (?), ~~with based on~~ the use of detailed the SKIM wave spectrum measurements (here replaced by in-situ buoy measurements) to estimate the wave Doppler  
835 velocity contribution  $U_{WD}$  ~~, associated to the wave associated with the waves~~ intrinsic phase speed ~~sensed through the surface slope spectrum. Accurate wave spectral measurements of.~~ Measuring the first directional moments ~~, such as provided by a buoy, (on which the buoy estimates are based)~~ is sufficient to estimate  $U_{WD}$  and resolving wavelengths of 15 m (a frequency

of 0.32 Hz) is ~~generally~~ sufficient to estimate the full spectral contribution, appending a parametric spectral shape ~~of~~ for the unresolved shorter waves. In fact it is most important to resolve the peak of the windsea, and a resolved wavelength of 30 m is typically enough for wind speeds higher than 7 m/s. As this article has shown, however, the angular distribution of the directional spectrum is a sensitive element, both in the resolved and parameterized wavelength ranges. Work is still needed to improve the spectral parameterization and to determine whether the accuracy of the sea state restitution algorithms intended for SKIM will be sufficient to solve this issue.

~~Subtracting off  $U_{WD}$  from the measured geophysical Doppler provides an estimate of the total surface current velocity  $U_{CD}$ . This velocity is expected to be representative of the top meter of the ocean as given by the depth of measurement for each monochromatic wave train (?), weighted by the slope spectrum. This velocity should contain most of R3S of (?), for the study of higher-order effects on the measured DFS. A subject of particular interest is for instance the effect of shear in the surface layer on the SKIM DFS, a key to the determination of the Stokes drift (??). As a result the velocity from any near-nadir Doppler Wave and Current Scatterometer, such as SKIM, is expected to give values between those of CARTE drifters and a 12-MHz HF radar, consistent with the results shown in figure ?? effective SKIM measurement depth.~~

The campaign also stressed the necessity of a very good knowledge of the measurement geometry, including antenna ~~pattern~~ radiation diagram, and the spatial and azimuthal variation of the radar cross-section. In this respect, the main characteristics of the ~~instruments used for the present campaign and of the planned SKIM satellite mission are recalled in table ??,~~ together with the value of the prefactor of the  $\sin(\varphi - \varphi_t) \partial_\varphi \log(\sigma^0)$  term in the expression (7) of  $U_{AGD}$  (as can be seen in figure ??,  $\partial_\varphi \log(\sigma^0)$  is typically  $0.1 \text{ rad}^{-1}$  at  $12^\circ$  incidence angle). As the apparent mispointing due to  $\sigma^0$  gradients in azimuth or space is proportional to the beam width squared, the non-geophysical velocities caused by this effect for SKIM, though non negligible, are actually much smaller than for KuROS, even at  $6^\circ$  incidence angle.

**Table 5.** Main differences between ~~airborne the~~ KaRADOC and KuROS ~~system as airborne radars~~ used in the present ~~paper~~ article, and the SKIM system as presented by ?. The factor  $\sigma_\varphi^2 \sin \theta V_p / 2 - \sigma_\varphi^2 V_p / 2$  is the ~~common factor that, multiplied by  $\sin \varphi \partial(\log(\sigma^0)) / \partial \varphi$  gives prefactor of  $\sin(\varphi - \varphi_t) \partial_\varphi \log(\sigma^0)$  in the spurious velocity  $U_{AGD}$ , given by eq expression of  $U_{AGD}$ .(??)~~

	KuROS $12^\circ$	KaRADOC $12^\circ$	SKIM $12^\circ$	SKIM $6^\circ$
Altitude (km)	3	3	832	832
platform velocity $V_p$ (m/s)	120	120	7000	7000
Beam width ( $\alpha_{-3dB}$ ) in degrees ( $^\circ$ )	15.0	1.85	0.65	0.58
half beam width on ground Gaussian fit parameter $\sigma_\varphi$ ( $^\circ$ )	30.6	3.8	1.32	2.35-2.36
$\sigma_\varphi^2 \sin \theta V_p / 2 - (\text{m/s} \sigma_\varphi^2 V_p / 2) (\text{m.s}^{-1} \cdot \text{rad})$	3.5-17	0.054-0.26	0.39-1.9	0.61-5.9

~~A true mispointing in azimuth  $\delta_\varphi$  gives a spurious velocity  $V_p \delta_\varphi \sin \varphi$ , and aircraft velocities lead to much less strict requirements than As discussed in section ??, due to the much reduced platform velocity, the pointing requirements for airborne systems are much easier to reach than for satellite systems for which a pointing accuracy of a few microradians cannot be achieved by attitude measurements alone (gyroscopes and star-trackers) but ~~uses must use~~ a separation of the geophysical and~~

non-geophysical patterns in the data (?). This data-driven approach is also used in airborne systems for correcting phase biases in the antenna ~~pattern (?; see also Appendix D) diagram (?)~~.

865 ~~The apparent mispointing due to  $\sigma^0$  gradients in azimuth or space is proportional to the beam width squared, and leads to larger non-geophysical velocities for KuROS at 12° incidence, than for SKIM, even at 6°. That effect however is practically negligible for KaRADOC at 12°, as shown in figure 2.~~

~~Finally~~ Finally, as discussed in section ??, we recall that the incidence angle is estimated from the range ~~measurement in the case~~ measurements in the cases of KuROS and ~~from SKIM, and directly from the platform attitude for the highly directive~~ antenna pattern for KaRADOC. Translated to SKIM, which uses range measurements like KuROS, it requires a knowledge of pencil-beam case of KaRADOC. In the spaceborne context, the local slope of the ocean ~~as the nearest ocean target for~~ has to be taken into account, as it can induce a mispointing of the nadir beam ~~is not exactly at nadir but slightly offset due to the geoid slope, of~~ up to 300 microradians (?) ~~and more importantly the sea surface height difference between the nadir and the oblique beams, and induce a correction in the elevation angle at the observation point.~~

875 Other radar system constraints or optimizations for satellite systems are discussed by ? and (? , chapter 5), with sampling issues further analyzed by ?.

## 6 Conclusions and perspectives

~~Although it was the first deployment of the KaRADOC instrument and only a limited dataset could be acquired due to the necessary adjustment process, the DRIF4SKIM-~~ The Drift4SKIM campaign clearly demonstrated that surface geophysical ~~velocities can be measured by a microwave Doppler radars implementing the pulse-pair method with a at~~ measuring at 12° ~~incidence.~~ incidence angle. The Ku-band measurements, though less easy to interpret due to the large antenna beamwidth of the instrument, also supported this view. The campaign data are consistent ~~, with a 10% bias,~~ with a Geophysical Model Function (GMF) that expresses the geophysical Doppler DFS as the sum of the range component of the Total Surface Current Velocity, and a Wave Doppler waves DFS that is a weakly varying function of the sea state, of the order of ~~2.5-2.0 m/s at~~ 2.4 m/s ~~. This wave Doppler is analogous to the Bragg velocity contribution in HF radars but it integrates at~~ Ku-band. This waves DFS integrates contributions of all wavenumbers and directions, weighted by the surface slope spectrum. It can be well estimated from the sea surface elevation directional spectrum using the Kirchhoff approximation framework.

~~For 11 m/s winds, the difference in drift velocity between CARTHE and SVP drifters and HF radar, of the order of 20 cm~~ The campaign highlighted the importance of a very good knowledge of the platform motion and orientation and of the ~~radar line-of-sight direction vector. The Ku-band NRCS/s, is not due to a large scale vertical shear, and may be associated to either a particular behaviour of CARTHE drifters in wave motions, or some shear in the top meter. This will be further investigated elsewhere using the 30 cm depth measurements of the Trèfle buoy (which capsized on November 21 in the present experiment)~~ DFS imagery, though not very successful in that respect, observed a large number of interesting modulation phenomena, which will be analyzed in more detail in forthcoming contributions.

895 In general, the robustness of the theoretical GMF and its possible empirical adaptation will require the acquisition of more data in a wider range of wind and wave conditions. An in-depth investigation of the angular width of the sea state directional spectrum in the short gravity waves regimes seems of particularly high interest in this respect. Also, obtaining a description of the scale-resolved statistics of sea surface slope skewness would open the path to a Kirchhoff approximation study of the upwind/downwind asymmetry of the radar NRCS and DFS, which is currently lacking.

900 Finally, the test of near-nadir satellite measurements is limited by the very different viewing geometry due to the difference in altitude. Airborne measurement footprints are at most 500 m or so, and thus cannot reproduce the averaging properties of ~~a the~~ much wider footprint ~~from a satellite of a satellite instrument~~. Still, this medium-sized footprint is comparable to the unfocused SAR resolution that will be obtained with SKIM and provides some practical application with a similar azimuthal averaging that has a limited directional resolution for swell spectrum measurement. ~~This limited azimuthal resolution is probably sufficient for estimating parameters such as the Stokes drift given by eq. (??) and does not require a full turn of the antenna to observe all waves, thereby making possible a higher spatial resolution of the Stokes drift vector.~~

905 Future airborne systems may ideally combine higher incidence angles such as used on DopplerScatt (?) and OSCAR/Wavemill (?), with near-nadir angles that allow unambiguous wave measurements. In that case, the ~~high azimuthal resolution large azimuthal footprint~~ of KuROS is probably not necessary, and a narrower beam like KaRADOC can be used, greatly simplifying the analysis ~~of antenna beam patterns~~.

*Code and data availability.* Data and numerical model results presented in this article are available via ftp at the following address: <http://tinyurl.com/SKIMftp>, and will become more easily accessible through the upcoming website of the ESA-funded IASCO project.

## Appendix A: ~~Pulse Pair~~ Doppler Scatterometry theory

915 This appendix proposes an extension of the theory of pencil-beam Doppler scatterometry exposed in (??) to the case of near-nadir fan-beam instruments such as SKaR and KuROS. It compiles a number of processing steps or concepts that had to be developed for the analysis of the Drift4SKIM KuROS data. In each section the differences and similarities with the spaceborne SKIM context are highlighted.

### A1 ~~Radar pulse-pair measurements~~ Pulse pair theory

#### A1.1 Radar pulse-pair measurements

920 A radar instrument works by sending microwave pulses into the environment, and recording the echo from its field of view. Usual scatterometers consider only the intensity of the return signal. Coherent instruments, such as SARs, measure both the amplitude of the return signal and its phase with respect to the transmitted carrier, as a function of range. Over the ocean, the phase of the return signal for a single pulse is random and uniformly distributed over the unit circle. The radar returns of successive pulses transmitted at short intervals are however correlated, and the time history of the phase can be used to

925 measure the relative motion of the radar and the scatterers. SARs make use of this property to refine the along-track resolution of backscattering cross-section measurements. SKIM and the other proposed Doppler missions aim to use it to obtain direct surface current measurements.

As explained by ?, Appendix A, the complex amplitude of the return signal of a pulse transmitted at time  $t_i$  can be expressed as

930 
$$E_i(t_i, r') = n(t_i, r') + \frac{A(r')}{r'^2} \times \int dS G(t_i, \mathbf{x}) \chi(r' - r(t_i, \mathbf{x})) \exp[-2ikr(t_i, \mathbf{x})] s(t_i, \mathbf{x}),$$

$$E_i(t_i, r') = n(t_i, r') + \frac{A(r')}{r'^2} \times \int dS G(t_i, \mathbf{x}) \chi(r' - r(t_i, \mathbf{x})) \exp[-2ikr(t_i, \mathbf{x})] s(t_i, \mathbf{x}), \quad (\text{A1})$$

where the integral is performed over the sea surface;  $A(r')$  is a time-independent weakly-dependent function of range, unimportant for our purposes here (corresponding in particular to the effects of transmitted signal amplitude, receiver and processing gain and attenuation losses);  $G(\mathbf{x})$  is the one-way antenna ~~pattern diagram~~;  $\chi(r)$  is the range point-target response of the instrument;  $r'$  is the nominal pixel range in the time sampled signal;  $k = 2\pi/\lambda$  is the radar wavenumber;  $r(t_i, \mathbf{x})$  is the range from the radar to the observation point  $\mathbf{x}$  at time  $t_i$ ;  $n(t_i, r')$  is the thermal noise contribution, and  $s(t_i, \mathbf{x})$  is the complex reflection coefficient of the sea surface at instant  $t_i$  and location  $\mathbf{x}$ .

940 As mentioned by ?, the thermal noise contribution, though it plays a major role in ~~setting~~ the quality of the measurements, ~~poses no great conceptual difficulty~~ is conceptually simple, and can be safely considered as  $\delta$ -correlated in time, and characterized by a single quantity, its average power  $N$ . The reflection coefficient  $s(t_i, \mathbf{x})$ , on the other hand, emerges from the interaction of the electromagnetic waves with the ocean surface, and has ~~a~~ much richer physics. It is affected by electromagnetic phenomena, by the geometry and kinematics of the sea surface itself, and its statistics are further complicated by the so-called

945 “speckle” phenomenon. As stated by ? the correlation function of this coefficient as a function of time and space separation, averaging averaged over speckle realizations, can be modelled as

$$\langle s(t, \mathbf{x}) s^*(t', \mathbf{x}') \rangle_S = \delta(\mathbf{x} - \mathbf{x}') \sigma^0(t, \mathbf{x}) \gamma_{TS}(|t - t'|), \quad (\text{A2})$$

with  $\sigma^0(t, \mathbf{x})$  the Normalized Radar backscattering Cross Section (NRCS) in the appropriate polarization, and  $\gamma_{TS}(|\tau|)$  a function describing its time decorrelation at a fixed location, due to the life history of individual scattering patches.

950 The so-called “Pulse-Pair” technique of (?) relies on the properties of the product of the return signals from consecutive radar pulses. Combining expressions (??) and (??) to compute the speckle-averaged product of the return signals for two ~~consecutive~~ radar pulses sent at  $t_1$  and  $t_2 = t_1 + \Delta t$ , with  $\Delta t$  the pulse repetition interval (PRI), one obtains

$$PP_{\Delta t}(t_1, r') = \langle E_2(t_2 = t_1 + \Delta t, r') E_1(t_1, r')^* \rangle_S$$

as:

955 
$$PP_{\Delta t}(t_1, r') = \langle E_2(t_2 = t_1 + \Delta t, r') E_1(t_1, r')^* \rangle_S \quad (\text{A3})$$

as

$$PP_{\Delta t}(t_1, r') = \frac{A^2(r')}{r'^4} \times \gamma_{TS}(|\Delta t|) \times \int \chi^2(r' - r(t_1, \mathbf{x})) G^2(t_1, \mathbf{x}) \sigma^0(t_1, \mathbf{x}) \times \exp[-2ik[r(t_1 + \Delta t, \mathbf{x}) - r(t_1, \mathbf{x})]] dS. \quad (\text{A4})$$

As can be seen in this equation, the phase of the pulse-pair signal contains a weighted average of the time rate-of-change of the distance separating the radar from the scattering elements in its instantaneous footprint. This rate of change can be interpreted as a velocity and this method is the so-called “Pulse-Pair” technique of ?.

## A2 Measurement geometry

### A1.1 Measurement geometry

Figures 1A and 1B summarize the acquisition geometry in the airborne and space-borne settings. The influence-of-the antenna radiation diagram  $G^2(t_1, \mathbf{x})$  is represented as a grey shading of the sea surface, while the influence-of-the range point-response function  $\chi^2(t_1, r' - r(t_1, \mathbf{x}))$  is represented as the grating-in-white-a white grating. In eq. (??), we have made the assumptions that  $G(t_1, \mathbf{x}) = G(t_2, \mathbf{x})$ , and  $\chi(r' - r(t_1, \mathbf{x})) = \chi(r' - r(t_2, \mathbf{x}))$ , neglecting the effect of the spatial translation of the beam illumination pattern and range-resolution weighting distribution on the sea surface.

This is a very good approximation for airborne pulse-pair radar observations, and a quite good one for spaceborne observations. For airborne instruments, the PRI is usually chosen such that the line-of-sight projection of the platform movement over a PRI is smaller than one-half carrier wavelength to avoid phase ambiguity. For space-borne instruments, avoiding ambiguity is not practical, due to the much larger platform velocity, but the PRI is constrained by other considerations, and the platform displacement over a PRI is much smaller than the characteristic scales of the antenna radiation diagram as well as of the range point-response.

### A1.2 Pulse-pair signal approximation

Returning to expression (??), we see that over the time interval separating the two radar pulses, the radar has moved from its original position  $\mathbf{x}_R(t_1)$  to  $\mathbf{x}_R(t_1) + \mathbf{V}_P \Delta t$ , and the scatterers originally located at  $\mathbf{x}$  have moved to  $\mathbf{x} + \mathbf{v}_s \Delta t$  (specifying the reference frame is not yet necessary since only relative separations are important at this stage). The radar-to-scatterers vector has thus changed by  $[\mathbf{v}_s(\mathbf{x}) - \mathbf{V}_P] \Delta t$ . The distance change can be approximated by

$$r(t_1 + \Delta t, \mathbf{x}) - r(t_1, \mathbf{x}) = \Delta t \frac{\mathbf{x} - \mathbf{x}_R(t_1)}{\|\mathbf{x} - \mathbf{x}_R(t_1)\|} \cdot (\mathbf{v}_s - \mathbf{V}_R), \quad (\text{A5})$$

where neglected- where the neglected terms are of the order of  $\Delta t^2 \|\mathbf{v}_s - \mathbf{v}_R\|^2 / \|\mathbf{x} - \mathbf{x}_R(t_1)\|^2$ . Introducing

$$\mathbf{e}(\mathbf{x}) = \frac{\mathbf{x} - \mathbf{x}_R(t_1)}{\|\mathbf{x} - \mathbf{x}_R(t_1)\|} \quad (\text{A6})$$

the unit vector pointing from the radar location at  $t_1$  to the observation point (choosing either time instant is equivalent, as the difference is of the same order of magnitude as the neglected terms), the pulse-pair signal can be expressed as

$$\underline{PP_{\Delta t}(t_1, r')} = \frac{A^2(r')}{r'^4} \times \gamma_{TS}(\Delta t) \times \int G^2(t_1, \mathbf{x}) \chi^2(r' - r(t_1, \mathbf{x})) \sigma^0(t_1, \mathbf{x}) \times \exp \left[ 2ik \Delta t \mathbf{e}(\underline{\mathbf{x}}) \cdot \left( \underline{\mathbf{V}}_R - \underline{\mathbf{v}}_s(\underline{\mathbf{x}}) \right) \right] dS. \quad (\text{A7})$$

985 This equation is not very practical, as the relative motion of the scatterers with respect to the radar enters as the argument of exponential contributions to an integral an exponential integrand. Obtaining an equivalent representation as the exponential of a sum of weighted integrals would be desirable. Introducing the effective illuminated surface

$$S(t_1, r') = \int G^2(t_1, \mathbf{x}) \chi^2(r' - r(t_1, \mathbf{x})) dS, \quad (\text{A8})$$

the normalized weighting function

$$990 \quad W(t_1, r', \mathbf{x}) = \frac{G^2(t_1, \mathbf{x}) \chi^2(r' - r(t_1, \mathbf{x}))}{S(t_1, r')}, \quad (\text{A9})$$

the average and fluctuating parts of the NRCS

$$\underline{\overline{\sigma^0}(t_1, r')} = \int W(t_1, r', \underline{\mathbf{x}}) \sigma^0(t_1, \underline{\mathbf{x}}) dS,$$

$$\underline{\widetilde{\sigma^0}(t_1, r')} = \frac{\sigma^0(t_1, \mathbf{x})}{\overline{\sigma^0}(t_1, r')},$$

995

$$\underline{\overline{\sigma^0}(t_1, r')} \equiv \int W(t_1, r', \underline{\mathbf{x}}) \sigma^0(t_1, \underline{\mathbf{x}}) dS, \quad (\text{A10})$$

$$\underline{\widetilde{\sigma^0}(t_1, r', \underline{\mathbf{x}})} \equiv \frac{\sigma^0(t_1, \mathbf{x})}{\overline{\sigma^0}(t_1, r')}, \quad (\text{A11})$$

and borrowing the algebraic technique of ‘‘cumulant expansion’’ from probability theory, it is possible to express  $PP_{\Delta t}$  as

$$1000 \quad \underline{PP_{\Delta t}(t_1, r')} = \frac{A^2(r')}{r'^4} \times \gamma_{TS}(\Delta t) \times \overline{\sigma^0}(t_1, r') \times S(t_1, r') \times \exp \left[ \sum_{n=1}^{\infty} \frac{(i2k\Delta t)^n}{n!} \kappa_n \right],$$

$$\underline{PP_{\Delta t}(t_1, r')} = \frac{A^2(r')}{r'^4} \times \gamma_{TS}(\Delta t) \times \overline{\sigma^0}(t_1, r') \times S(t_1, r') \times \exp \left[ \sum_{n=1}^{\infty} \frac{(i2k\Delta t)^n}{n!} \kappa_n \right], \quad (\text{A12})$$

with  $\kappa_n$  the successive ‘‘cumulants’’ of  $\mathbf{e}(\mathbf{x}) \cdot (\mathbf{V}_R - \mathbf{v}_s(\mathbf{x}))$  with respect to the ‘‘density distribution’’  $\widetilde{\sigma^0}(t_1, \mathbf{x}) W(t_1, r', \mathbf{x}) \widetilde{\sigma^0}(t_1, r', \mathbf{x}) W(t_1, r', \mathbf{x})$

As all the  $\kappa_n$  are real, we see that odd- $n$  terms contribute to the argument of the pulse-pair signal, while even- $n$  terms contribute

1005 to its magnitude. Keeping only the first two terms in the sum, one obtains:

$$\underline{PP_{\Delta t}(t_1, r')} = \frac{A^2(r')}{r'^4} \times \gamma_{TS}(\Delta t) \times \overline{\sigma^0}(t_1, r') \times S(t_1, r') \\ \times \exp \left[ i2k\Delta t\kappa_1 \right] \times \exp \left[ -2(k\Delta t)^2\kappa_2 \right].$$

$$\underline{PP_{\Delta t}(t_1, r')} = \frac{A^2(r')}{r'^4} \times \gamma_{TS}(\Delta t) \times \overline{\sigma^0}(t_1, r') \times S(t_1, r') \times \exp \left[ i2k\Delta t\kappa_1 \right] \times \exp \left[ -2(k\Delta t)^2\kappa_2 \right]. \quad (\text{A13})$$

1010 As expected, the expression of  $\kappa_1$ ,

$$\underline{\kappa_1(t_1, r')} \equiv \int \underline{W(t_1, r', \mathbf{x})} \underline{\widetilde{\sigma^0}(t_1, \mathbf{x})} \underline{\mathbf{e}(\mathbf{x})} \cdot \underline{\left( \mathbf{V}_R - \mathbf{v}_s(\mathbf{x}) \right)} dS$$

$$\kappa_1(t_1, r') = \int W(t_1, r', \mathbf{x}) \widetilde{\sigma^0}(t_1, r', \mathbf{x}) \mathbf{e}(\mathbf{x}) \cdot (\mathbf{V}_R - \mathbf{v}_s(\mathbf{x})) dS \quad (\text{A14})$$

1015 shows that to first order the argument of the pulse-pair signal gives access to the integral over the footprint of the relative velocity of the scatterers with respect to the radar. The expression of  $\kappa_2$ ,

$$\kappa_2(t_1, r') = \int W(t_1, r', \mathbf{x}) \widetilde{\sigma^0}(t_1, r', \mathbf{x}) [\mathbf{e}(\mathbf{x}) \cdot (\mathbf{V}_R - \mathbf{v}_s(\mathbf{x})) - \kappa_1]^2 dS, \quad (\text{A15})$$

is a description of the impact of the variability of  $\mathbf{e}(\mathbf{x})$ ,  $\widetilde{\sigma^0}$  and  $\mathbf{v}_s$  inside the footprint on the pulse-pair signal magnitude.

### A1.3 Pulse-pair signal phase approximation

1020 **Selecting a frame of reference** [Working now in the Earth-fixed referenced frame at the observation point](#), we define

$$V_{GD} = - \int W(t_1, r', \mathbf{x}) \widetilde{\sigma^0}(t_1, r', \mathbf{x}) \mathbf{e}(\mathbf{x}) \cdot \mathbf{v}_s(\mathbf{x}) dS \quad (\text{A16})$$

the (geophysically relevant) weighted projection of the scatterers velocity in that frame on the radar line-of-sight and

$$V_{NG}(t_1, r') = \mathbf{V}_R \cdot \int W(t_1, r', \mathbf{x}) \widetilde{\sigma^0}(t_1, r', \mathbf{x}) \mathbf{e}(\mathbf{x}) dS \quad (\text{A17})$$

1025 the (**geophysically irrelevant non-geophysical**) projection of the radar velocity. (Our conventions are such that  $V_{GD}$  is positive when the scatterers move towards the radar, and that  $V_{NG}$  is positive when the radar moves towards the footprint, in keeping with everyday intuition).

With these conventions, one sees that:

$$V_{GD}(t_1, r') = \kappa_1(t_1, r') - V_{NG}(t_1, r'). \quad (\text{A18})$$



Using equation (??), one can obtain  $\kappa_1$  approximately as  $1/(2k\Delta t)$  times the argument of the complex pulse-pair signal. ~~To~~  
 1030 ~~do so~~At this stage, one must however consider a bit carefully the ambiguity that is inherent in phase measurements. As the  
phase of a complex number is only known up to a multiple of  $2\pi$ ,  $\kappa_1$  is only obtained up to a multiple of  $\frac{\lambda}{2\Delta t}$ . This effect can  
be neglected as long as both  $V_{\text{NG}}$  and  $\kappa_1$  remain within the unambiguous interval  $[-\frac{\lambda}{4\Delta t}; \frac{\lambda}{4\Delta t}]$ . For larger platform velocities,  
care must be taken to add the right multiple of  $\frac{\lambda}{2\Delta t}$  to  $\kappa_1$  before subtracting  $V_{\text{NG}}$ . For airborne instruments it is usually feasible  
 1035 fixed reference frame, in which  $\mathbf{v}_s$  is small, and to work on the phase-migrated pulse pair signal

$$\widetilde{PP}_{\Delta t}(t_1, r') = \exp \left[ -i2k\Delta t V_{\text{NG}} \right] \times PP_{\Delta t}(t_1, r').$$

$$\widetilde{PP}_{\Delta t}(t_1, r') = \exp \left[ -i2k\Delta t V_{\text{NG}} \right] \times PP_{\Delta t}(t_1, r'). \quad (\text{A19})$$

It is easy to see that  $V_{\text{GD}}$  can be retrieved as

$$1040 \quad \widetilde{V}_{\text{GD}}(t_1, r') = \frac{1}{2k\Delta t} \arg \left( \widetilde{PP}_{\Delta t}(t_1, r') \right).$$

$$\widetilde{V}_{\text{GD}}(t_1, r') = \frac{1}{2k\Delta t} \arg \left( \widetilde{PP}_{\Delta t}(t_1, r') \right). \quad (\text{A20})$$

At this stage, even a coarse approximation of  $V_{\text{NG}}$  can be used, as long as it is sufficient to resolve the phase ambiguity.  
 This is important in particular for the onboard processors of satellite instruments, which have to rely on limited quality po-  
 1045 sition/velocity/pointing information and typically can not use the  $\widetilde{\sigma}^0$  distribution information ground segment processors can  
 retrieve from the signal. ~~Care must however be taken to take account of the~~ The correction applied by the onboard processor  
must however be accounted for in later processing stages.

## A2 Non-geophysical Doppler contribution $V_{\text{NG}}$

### A2.1 Overview

1050 ~~This section will describe the different contributions to Non-geophysical Doppler (The Non-Geophysical contribution  $V_{\text{NG}}$  ).~~  
~~At first order the signature is dominated by~~ must be estimated from the platform velocity and ~~its pointing knowledge.~~ A second  
~~point is the determination of the range knowledge which is directly linked to the timing and altitude accuracy. This point is~~  
~~critical for radar beam pointing.~~ For pulse-limited instruments ~~, such~~ as KuROS and SKaR, ~~for which the pointing is determined~~  
~~for the incidence angle is determined in~~ each range bin as a function of the altitude. The accuracies of the range resolution  
 1055 and altitude determination processes are then critical. Last, asymmetric ~~variation in NRCS within the antenna azimuth for~~  
~~azimuthal variation of the sea surface NRCS within~~ a given range bin ~~generate a bias in Doppler.~~ All these three elements need  
~~to be accurately corrected in order to have an accurate geophysical Doppler measurement~~ tend to bias the effective observation  
azimuth towards the brighter part of the instrument FOV. This section discusses these different aspects.

## A2.1 Pointing knowledge Beam pointing accuracy

1060 ~~At this point of the discussion, we will leave the general setting and will start orienting our convention choices towards the description of the airborne case of the Drift4SKIM campaign. Problems specific to the space-borne case, such as the need to work in global-scope reference frames or to account for Earth rotation and sphericity, or structural details such as the parabolic reflector featured by the SKaR instrument, do not change the deep nature of the issues, but do introduce a heavy notational burden which tends to obscure the discussion.~~

1065 From now on, we ~~will~~ work in the simplified setting of the flat-Earth approximation, in which the elevation and incidence angles  $\gamma$  and  $\theta$  are equal. We ~~will~~ use a platform-fixed reference frame, the origin of which is located at the antenna phase center of the instrument, with  $x$ -vector pointing to the geometric front of the platform,  $y$ -vector pointing to starboard, and  $z$ -vector pointing to the floor, and a local geographic North/East/Down reference frame, the origin of which is fixed to the solid Earth and located at a suitable point of the campaign area.

1070 The orientation of the platform-fixed reference frame with respect to the local geographic frame is provided by the platform IMU as (Roll, Pitch, Heading) Euler angles, from which one can construct the Direction Cosine Matrix  $\dagger$

$$\text{DCM} = \begin{bmatrix} c_p \cdot c_h & s_r \cdot s_p \cdot c_h - c_r \cdot s_h & c_r \cdot s_p \cdot c_h + s_r \cdot s_h \\ c_p \cdot s_h & s_r \cdot s_p \cdot s_h + c_r \cdot c_h & c_r \cdot s_p \cdot s_h - s_r \cdot c_h \\ -s_p & s_r \cdot c_p & c_r \cdot c_p \end{bmatrix} \quad (\text{A21})$$

allowing one to express the components of a vector in the  $(N, E, D)$  frame from its  $(x, y, z)$  components in the platform-fixed frame. The two reference frames are consistent in the sense that the frame vectors coincide when the platform is in **level**  
 1075 constant altitude flight towards the North. In the above expression we have used the transparent notation  $c_p \rightarrow \cos(\text{pitch})$ ,  $s_r \rightarrow \sin(\text{roll})$ ,  $c_h \rightarrow \cos(\text{heading})$ , etc... Other quantities worth introducing are the course  $c$  and glide angle  $g$  such that the plane velocity vector in the NED frame is

$$\mathbf{V}_R = V_R [\cos(g) \cos(c) \mathbf{N} + \cos(g) \sin(c) \mathbf{E} + \sin(g) \mathbf{D}]. \quad (\text{A22})$$

In the NED frame, the pointing vector  $\mathbf{e}$  can be expressed as

$$1080 \quad \mathbf{e} = \sin(\theta) [\cos(\varphi) \mathbf{N} + \sin(\varphi) \mathbf{E}] + \cos(\theta) \mathbf{D}. \quad (\text{A23})$$

Its components in the platform-fixed frame can be determined using the fact that  $\text{DCM}^{-1} = \text{DCM}^T$ . The corresponding antenna azimuth and elevation angles  $\varphi$  and  $\gamma$ , in terms of which the radiation diagram is specified, can then be expressed using the platform-fixed to antenna-fixed reference frame transformation matrix.

With these notations, and using eq. (??), one can express  $V_{NG}$  as

$$1085 \quad \underline{V_{NG}(t_1, r')} = V_R \int \underline{W(t_1, r', \mathbf{x})} \underline{\tilde{\sigma}^0(t_1, r', \mathbf{x})} [\cos(g) \sin(\theta) \cos(\varphi - c) + \sin(g) \cos(\theta)] dS. \quad (\text{A24})$$

Constant altitude flight corresponds to  $g \simeq 0$ . We thus concentrate on the impact of errors in the first term of the RHS of this equation. Quite clearly, the impact of errors in  $\sin(\theta)$  is largest when the instrument views the area where  $\cos(\varphi - c)$  is large,

*i.e.* in the up/down-track directions, while the impact of errors in the azimuthal direction is largest when the instrument looks cross-track (*i.e.* where the derivative of  $\cos(\varphi - c)$  is close to 1).

1090 Leaving aside for the moment the effects of uncertainties on  $W(t_1, r', \mathbf{x})$  and  $\widetilde{\sigma}^0(t_1, \mathbf{x})$ , one sees that at  $12^\circ$  incidence [angle](#), and for a platform velocity of 7000 m/s (space-borne instrument), the SKIM ~~1-40~~ cm/s error budget on horizontal velocity measurements translates to pointing accuracies of ~~0.3 and 1.4~~ [4.5 and 21](#) microradians in incidence [angle](#) and azimuth, respectively (~~these figures are obtained by allowing each of the pointing errors to consume the full error allocation. As the two terms reach their maximal amplitudes in different parts of the swath, this is not unreasonable~~[see the discussion in](#)

1095 [section ??](#)). In the airborne case at 120 m/s platform velocity and 3000 m altitude, the corresponding numbers are ~~18 and 85~~ [0.26 and 1.25](#) milliradians for incidence [angle](#) and azimuth pointing accuracy for KuROS, respectively. In the cross-track viewing geometry of KaRADOC, only the comparatively mild (but still quite demanding) ~~85~~ [1.25](#) milliradians azimuth pointing accuracy requirement applies.

Figure (??).A) shows the measurement geometry, seen from above. One can see that uncertainties on the viewing azimuth and incidence [angle](#) have different origins:

- the uncertainty in azimuth can be due to an imperfect knowledge of the weighting corresponding to the  ~~$W(t_1, r', \mathbf{x}) \widetilde{\sigma}^0(t_1, \mathbf{x})$~~  [term in eq. \(??\)](#). This can of course come from imperfect platform attitude or antenna orientation information, but also from an imperfect characterization of the antenna radiation diagram or of the distribution of  $\sigma^0$  on the sea surface.
- 1105 – the uncertainty in incidence [angle](#) is due to an imperfect knowledge of the radial position of the range resolution bins (yellow striping of the footprint ~~if in~~ [fig. ??](#).A). This can be due to an imperfect timing accuracy, or to an imperfect knowledge of the vertical separation between [the](#) instrument and sea surface.

## A2.2 Timing and altitude accuracy

For this brief discussion of the effects of timing and altitude accuracy on incidence angle estimation, we consider a single range

1110 bin whose “true” range from the radar is  $r$ , whose altitude with respect to the radar is  $H$ , and where the incidence angle is  $\theta$ . In this case  $\theta = \arccos(H/r)$ . If now the radar suffers from a timing error  $\delta r$ , the instrument will detect a false altitude  $H - \delta r$ , but will ascribe to range bin  $r - \delta r$  the signal coming from  $r$ . In the meantime, we consider that the surface-tracking algorithm suffers from an error  $\delta h$ , and detects the surface at range  $H - \delta r - \delta h$ . The data from this range bin will thus be processed using an angle of incidence

$$1115 \quad \theta + \delta_\theta \theta = \arccos\left(\frac{H - \delta r - \delta h}{r - \delta r}\right), \quad (\text{A25})$$

different from the correct value by

$$\delta_\theta \theta \simeq \frac{1}{\tan(\theta)} \frac{1}{H \tan(\theta)} \left[ \frac{\delta h}{H} \cos(\theta) \delta h + \frac{\delta r}{H} \delta r [1 - \cos(\theta)] \right]. \quad (\text{A26})$$

Considering  $\delta h$  and  $\delta r$  as independent, we see that at  $12^\circ$  ~~incidence the incidence~~ the incidence angle knowledge requirements expressed above for SKIM and KuROS translate respectively to timing accuracy requirements of ~~2.4 m and 0.5~~ 36.8 m and 7.7  
 1120 m, and to surface-tracking accuracy requirements of ~~5.480.4 cm and 1.14~~ 16.9 cm.

The timing accuracy requirements are easily met in the spaceborne context, but can be challenging in the cost-constrained context of an airborne instrument.

The surface-tracking algorithm, however, does not benefit from the error-compensation that exists for the timing error. The requirement for SKIM is ~~stringent, but the SKIM mission comprises a state-of-the-art Ka-band nadir-looking altimeter capable~~  
 1125 ~~of reaching this goal. The 1.14~~ easily met by the nadir altimeter payload of SKIM. The 80.4 cm altitude tracking requirement is ~~clearly~~ out of reach of the KuROS airborne instrument. Our analysis of its ~~Doppler DFS~~ data will thus be restricted to the side-looking configurations for which, as per eq. (??), the pointing requirements are much milder.

### A2.3 Effective pointing / Azimuth Gradient ~~Doppler DFS~~

1130 As expressed in eq. (??), for each range resolution cell  $V_{NG}$  results from an integral over azimuth with a weight that depends on the product of the antenna radiation diagram and the sea surface NRCS, which varies as a function of the horizontal position  $(x, y)$  due to the presence of waves, varying winds, currents, surfactants, sea ice and all the physical properties of the sea surface.

1135 Even with a perfect knowledge of the platform attitude and velocity, NRCS variations can thus make the effective pointing of the measurements deviate from the pure geometric estimates. Valuable insight into this effect can be gained by considering the saddle-point approximation of eq. (??) in the limit of a very narrow antenna diagram (which is clearly applicable for SKIM and KaRADOc, less so for KuROS).

Considering first the case of an antenna pointing towards azimuth  ~~$\varphi_A$~~   $\varphi_b$  with an infinitely narrow radiation diagram, we see that the product  $W(t_1, r', \varphi) \widetilde{\sigma}^0(t_1, r', \varphi)$  is well approximated by the Dirac distribution  ~~$\delta(\varphi - \varphi_A)$~~   $\delta(\varphi - \varphi_b)$ . In this limit

$$1140 \quad V_{NG}(t_1, r') = V_R \left[ \cos(g) \sin(\theta) \cos(\varphi_{Ab} - c) + \sin(g) \cos(\theta) \right]. \quad (\text{A27})$$

We recognize in this expression  $V_{geo}$ , the estimate of  $V_{NG}$  one would have derived using direct geometric arguments.

The essence of the argument is that the sharpest factor in the integral is the beam radiation diagram. If it is now not infinitely sharp, we see that the effect of a gradient of  $\widetilde{\sigma}^0$  is to shift the peak of the distribution by an angle

$$\delta \varphi = - \frac{\left. \frac{\partial \varphi \log(\widetilde{\sigma}^0)}{\partial \varphi} \right|_{\varphi_A}}{\left. \frac{\partial \varphi \log(W)}{\partial \varphi} \right|_{\varphi_A}} \frac{\left. \frac{\partial \varphi \log(\widetilde{\sigma}^0)}{\partial \varphi} \right|_{\varphi_b}}{\left. \frac{\partial \varphi \log(W)}{\partial \varphi} \right|_{\varphi_b}}. \quad (\text{A28})$$

1145 Assuming for  $W(t_1, t', \varphi)$  a Gaussian approximation

$$W(t_1, r', \varphi) = \frac{1}{\sqrt{\pi} \sigma_\varphi(r')} \exp \left[ - \frac{(\varphi - \varphi_A)^2}{\sigma_\varphi^2(r')} - \frac{(\varphi - \varphi_b)^2}{\sigma_\varphi^2(r')} \right] \quad (\text{A29})$$

in which  $\sigma_\varphi(r')$  is a parameter describing the width of the antenna diagram at the working incidence angle, one obtains

$$\underline{V_{NG}(t_1, r') = V_R [\cos(g) \sin(\theta) \cos(\varphi_A - c + \delta\varphi) + \sin(g) \cos(\theta)].}$$

1150 ~~with~~

$$\underline{V_{NG}(t_1, r') = V_R [\cos(g) \sin(\theta) \cos(\varphi_b - c + \delta\varphi) + \sin(g) \cos(\theta)].} \quad (\text{A30})$$

with

$$\delta\varphi = \frac{\sigma_\varphi^2(r')}{2} \partial_\varphi \log(\widetilde{\sigma^0}). \quad (\text{A31})$$

Alternatively, one can choose to express  $V_{NG}$  as the sum of  $V_{geo}$ , the geometric approximation, plus an Azimuth Gradient

1155 Doppler velocity contribution

$$V_{NG}(t_1, r') = V_{geo}(t_1, r') + V_{AGD}(t_1, r'), \quad (\text{A32})$$

with

$$V_{geo}(t_1, r') = V_R \left[ \cos(g) \sin(\theta) \cos(\varphi_{Ab} - c) + \sin(g) \cos(\theta) \right] \quad (\text{A33})$$

and

$$\underline{V_{AGD}(t_1, r') = -V_R \cos(g) \sin(\theta) \sin(\varphi_A - c) \times \frac{\sigma_\varphi^2(r')}{2} \partial_\varphi \log(\widetilde{\sigma^0}).}$$

$$\underline{V_{AGD}(t_1, r') = -V_R \cos(g) \sin(\theta) \sin(\varphi_b - c) \frac{\sigma_\varphi^2(r')}{2} \partial_\varphi \log(\widetilde{\sigma^0}).} \quad (\text{A34})$$

One can see from these expressions that for a given azimuthal variation of the NRCS the order of magnitude of  $V_{AGD}$  is set by  
 1165 the width of the antenna radiation diagram: instruments with a thin diagram, such as SKIM and KaRADOC, are less affected than instruments with a broader pattern diagram, such as KuROS. Also, one sees that  $V_{AGD}$  is largest when the instrument looks in the cross-track direction, and is zero in the up/down track viewing directions. Finally, one sees that  $V_{AGD}$  is equivalent to the line-of-sight projection of a spurious horizontal velocity  $U_{AGD}$ , which varies with incidence angle only through the variations of  $\widetilde{\sigma^0}$  and  $\sigma_\varphi$ :

$$1170 \quad U_{AGD}(t_1, r') = -V_R \sin(\varphi_{Ab} - c) \frac{\sigma_\varphi^2(r')}{2} \partial_\varphi \log(\widetilde{\sigma^0}). \quad (\text{A35})$$

At small scales, spatial gradients add to the azimuthal gradient and also induce a spurious velocity with the same expression as a function of  $\tilde{\sigma}^0$ . Using the simple case of a single Fourier component  $\tilde{\sigma}^0 = \varepsilon \sin[\nu(\varphi - \varphi_b)]$  allows one to evaluate the importance of different scales. The azimuthal shift can be obtained as

$$\delta\varphi = \varepsilon \exp\left(-\frac{(\nu^2 + 1)\sigma_\varphi^2}{4}\right) \sinh\left(\frac{\nu\sigma_\varphi^2}{2}\right). \quad (\text{A36})$$

1175 In the slow-variation limit  $\nu, \sigma_\varphi \rightarrow 0$ , and eq. (??) this expression coincides with eq. (??). For faster variations, one sees that the largest disturbance is obtained when  $\nu \sim \sqrt{2}/\sigma_\varphi$ . This azimuthal wavenumber is such that the footprint can host a bright and a dark patch, one on either side of the look direction. This configuration creates the largest disturbance for a given value of the brightness contrast  $\varepsilon$ .  $\delta\varphi$  in this case is given by

$$\delta\varphi_{\max} = \varepsilon\sigma_\varphi e^{-1/2}/\sqrt{2}. \quad (\text{A37})$$

## 1180 Appendix B: KuROS antenna ~~pattern~~-~~diagram~~ determination

A precise determination of the antenna ~~pattern~~-~~diagram~~ is necessary for any Doppler application, given the possibly large contribution of pointing errors  $\varphi_b - \tilde{\varphi}$  in the estimation of the non-geophysical ~~Doppler~~-~~DFS~~, and the effect of the antenna beamwidth in the spurious Azimuth Gradient velocity  $U_{\text{AGD}}$ . A comprehensive strategy has thus been developed for estimating the 1-way antenna ~~pattern~~-~~G~~( $\alpha, \beta$ )-~~diagram~~ in amplitude and phase, combining anechoic chamber measurements and  
 1185 verification using the campaign data, and final adjustment of systematic phase shifts in the data. (In this section  $\alpha$  and  $\beta$  are ~~the azimuth and elevation relative to~~ respectively the latitude and longitude of a set of spherical coordinates centered on the antenna, respectively), and such that the main lobe extends in a longitudinal sector on the equator  $\alpha = 0^\circ$ , and the rotation axis of the antenna turntable points towards  $\alpha = 0^\circ, \beta = 0^\circ$ . With this choice of coordinates the antenna diagram has separable Gaussian dependencies on  $\alpha$  and  $\beta$ . In constant altitude flight, when the antenna points towards  $\varphi_b$ ,  $\sin(\alpha) = \sin(\theta)\sin(\varphi - \varphi_b)$ ,  
 1190  $\tan(\beta) = \tan(\theta)\cos(\varphi - \varphi_b)$ ).

### B1 Fixed antenna NRCS correction

The anechoic chamber measurements are very accurate for the antenna alone. However, once integrated into the plane, the antenna ~~pattern~~-~~diagram~~ is perturbed. This is for instance particularly noticeable in the NRCS measurements in rotating mode, where a spurious azimuthal pattern could clearly be seen, or for fixed-antenna ~~Doppler~~-~~DFS~~ observations, where a ~~striping~~  
 1195 ~~pattern~~-“striping” pattern as a function of incidence angle is obvious. We have thus developed a complementary method that relies on the variations of the plane attitude during maneuvers. Using the plane IMU, we identify the angular coordinates  $\alpha$  and  $\beta$  of the nadir, and use the measured power to map the antenna ~~pattern~~-~~diagram~~ (using as a reference point the ~~level flight constant altitude~~ return power values for each data segment, to account for geophysical nadir NRCS variations). The combination of all the flights during the campaign gives the distribution of measured power as a function of  $\alpha$  and  $\beta$  that is  
 1200 shown in Figs. ?? and ??.

The measured distribution is well approximated by a Gaussian shape

$$G(\alpha, \beta) = \exp \left[ -\frac{\alpha^2}{2\sigma_\alpha^2} - \frac{(\beta - \beta_0)^2}{2\sigma_\beta^2} \right]. \quad (\text{B1})$$

Another expression for  $G(\alpha, \beta)$ , more suitable for use with the half-power beamwidths  $\alpha_{-3\text{dB}}$  and  $\beta_{-3\text{dB}}$  obtained from anechoic chamber measurements, is:

$$1205 \quad G(\alpha, \beta) = 2 \left[ -\frac{4\alpha^2}{\alpha_{-3\text{dB}}^2} - \frac{4(\beta - \beta_0)^2}{\beta_{-3\text{dB}}^2} \right]. \quad (\text{B2})$$

The width parameters in these equations are linked by

$$\sigma_\alpha = \alpha_{-3\text{dB}} / \sqrt{8 \log(2)}, \quad \sigma_\beta = \beta_{-3\text{dB}} / \sqrt{8 \log(2)} \quad (\text{B3})$$

The parameter values used in this study are collected in table 1.

1210 One cautionary remark is that the illuminated patch at nadir is not infinitely sharp. The measured distribution is thus the convolution of the true antenna diagram by the power distribution at the nadir patch (which depends on the altitude tracking error as well as the sea state (?)). Assuming Gaussian shapes, the squares of the width parameters add, leading to

$$\sigma_{\text{observed}} \simeq \sigma_{\text{true}} \left[ 1 + \frac{\sigma_{\text{patch}}^2}{2\sigma_{\text{true}}^2} \right].$$

$$\sigma_{\text{observed}} \simeq \sigma_{\text{true}} \left[ 1 + \frac{\sigma_{\text{patch}}^2}{2\sigma_{\text{true}}^2} \right]. \quad (\text{B4})$$

1215 The broadening of the diagram due to finite nadir patch size is thus a small correction provided the scale of the nadir patch remains smaller than the antenna diagram scales. For reasonable orders of magnitude of the altitude tracking error and significant wave height, the patch -3 dB width is of the order of  $3^\circ$  when viewed from 3000 m height. This corresponds to a 3% correction on the value of  $\sigma_\alpha$ . We have chosen to neglect this correction. The values summarized in table 1 are the parameters of the Gaussian fits to the observed distributions.

## 1220 **B2 Rotating antenna NRCS correction**

Using these parameters as a starting point, we have then constructed corrections for the rotating antenna measurements of NRCS, by allowing the boresight elevation  $\beta_0$  to vary as a function of antenna orientation within the plane. The variation law was determined by minimizing the dependence of the rotating-antenna NRCS measurements as a function of flight direction over the ~~Offshore box~~ “offshore” area for each day.

### 1225 B3 Fixed antenna ~~Doppler-DFS~~ correction

In a similar way, we have observed that the KuROS antenna diagram is slightly “wrinkled”, in that the beam boresight azimuth changes as a function of elevation. This azimuthal mispointing transposes immediately into a striping modulation of the  $U_{GD}$  estimates. A correction was introduced by allowing the boresight azimuth  $\alpha_0$  to vary as a function of  $\beta$ . The variation law of  $\alpha_0$  was determined by minimizing the average  $U_{GD}$  over all flights for each value of  $\beta$ . As the variation of this quantity with respect to  $\alpha_0(\beta)$  is not trivial, this required constructing, regularizing and inverting the observation matrix.

### Appendix C: KaRADOc system

KaRADOc is built around an Agilent PNA-X ~~vector~~ network analyzer, complemented by a TX power amplifier, a T/R switch, a RX low-noise amplifier, and a high-gain purpose-built slotted waveguide antenna (shown in Fig. ??). ~~The antenna radiation diagram is very narrow, with a beamwidth less than 1.5° in the H-plane (ie in elevation) and less than 2° in the E-plane (ie in azimuth) (see Fig. ??).~~

The beam can be steered in elevation by changing the instrument working frequency (see Fig. ??A), and the antenna is usually mounted on a pitch/roll stabilization platform. For the Drift4SKIM experiment, however, the antenna was rigidly mounted in a port-looking configuration, centered on 10° incidence angle, with a 2° backward-looking tilt to compensate for the aircraft pitch in level flight. ~~Observations at 12° constant altitude flight. Plane attitude variations were accounted for in the data processing. Observations~~ were collected at 33.7 GHz, corresponding to 12° nominal incidence angle. Other angles were also scanned, but RF leakage from the TX to the RX subsystems was too strong at the corresponding frequencies, making the signal harder to analyze.

~~Mainlobe beamwidth in E- and H-plane. Port 2 was used in the Drift4SKIM deployment. The scan mode is obtained thanks to a slotted waveguide antenna~~ The antenna radiation diagram is very narrow, with a beamwidth less than 1.5° in elevation and less than 2° in azimuth (see Fig. ~~??~~) by tuning the frequency to the desired incidence angle. ??B. Figures ??A and ??B represent sections across the KaRADOc main lobe in the azimuth and elevation direction, at 33.7 GHz.





---

**Figure 11.** Same as Figure ??C but using port-looking antenna data collected on 24-November 24th, 11:22 → 13:03 (UTC).

Plots of the Ka-band Doppler signal on (top) 2018/11/22 and (bottom) 2018/11/24. The flight tracks are marked as thin black lines. For each flight track, a thick blue line shifted to the right of the flight path by an amount proportional to the instantaneous Doppler represents the projection of the  $U_{GD}$  vector along the instrument line-of-sight. At the beginning of each track data were discarded until the plane stabilized. The green arrow represents the maximum-likelihood estimate of the  $U_{GD}$  vector using the whole data set. The 1-standard deviation error ellipse on the maximum-likelihood estimate is represented in green.

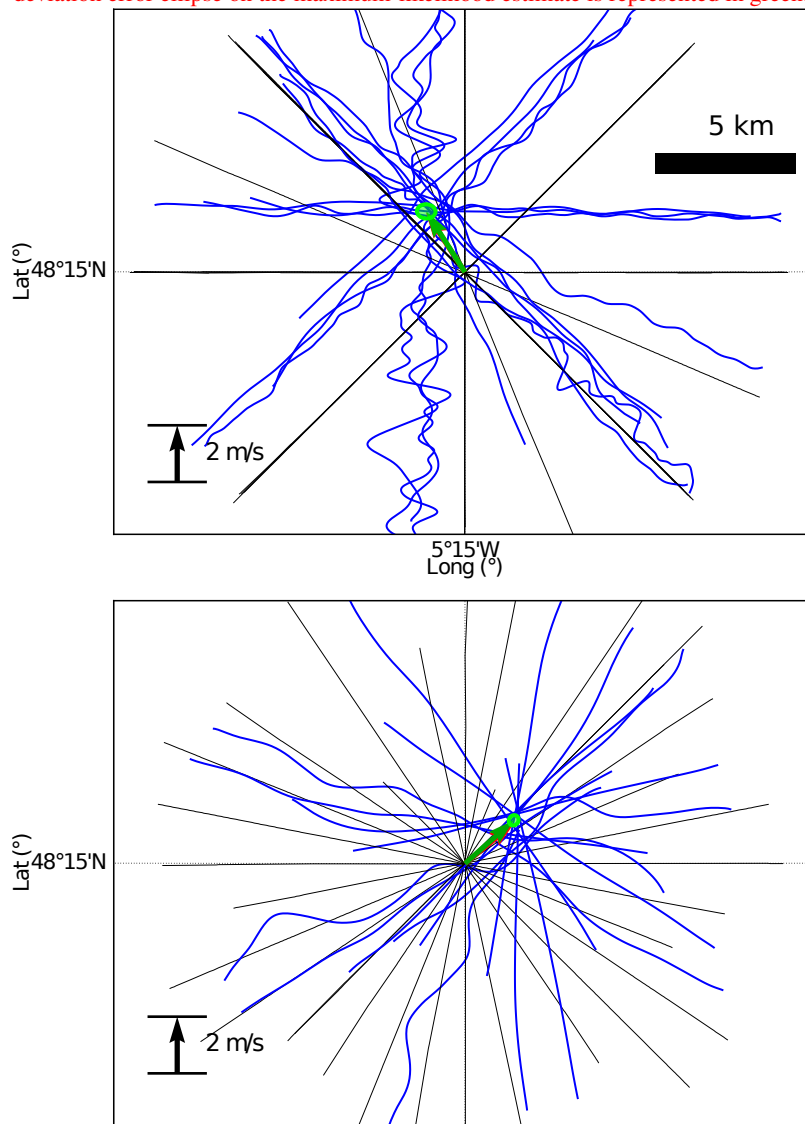
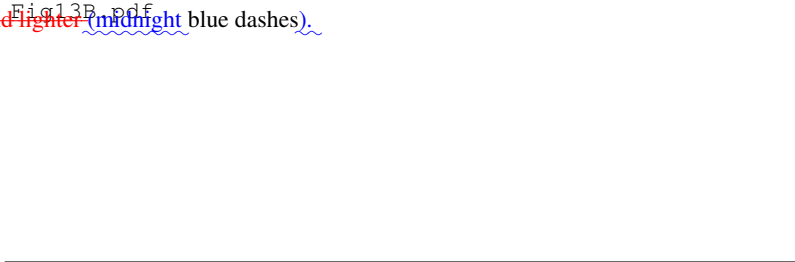


**Figure 12.** Plots of the Ka-band Doppler velocity signal on (top) 2018/11/22 and (bottom) 2018/11/24. The flight tracks are marked as thin black lines. For each flight track, a thick blue line shifted to the right of the flight path by an amount proportional to the instantaneous Doppler velocity represents the projection of the  $U_{GD}$  vector along the instrument line-of-sight. At the beginning of each track data were discarded until the plane stabilized. The green arrow represents the maximum-likelihood estimate of the  $U_{GD}$  vector using the whole data set. The red arrow shows the result of the least-squares sinusoidal fits shown in figures ??A and ??B. The 1-standard deviation error ellipse on the maximum-likelihood estimate is represented in green.

## forward model: $U_{GD} = U_{CD} + U_{WD}$



**Figure 13.** KaRADOC Doppler velocity (red circles) for the star-pattern flight of (TopA) 22 November 22nd and (BottomB) 24 November 24th. Cosine function fit fits to the data (red lines) that would be consistent with the radial projection of a vector. These are compared to modeled geophysical Doppler velocity  $U_{GD}$  and an adjusted  $U'_{GD}$  in green, where using the adjustment is a constant factor 10% reduction MEM (resp. MLM) estimate of  $U_{WD}$  the directional wave spectrum (green, resp. darker green). The modeled  $U_{GD}$  is the sum of the CARTHE drifter velocity  $U_{CD}$  in short dashed dark blue (blue) and the wave Doppler velocity estimated from the measured spectra,  $U_{WD}$ , in longer and lighter (midnight blue dashes).



Retrieval of surface current vector  $U_{CD}$  in blue obtained, compared to in situ measurements by HF-radar, CARTHE and SVP drifter (three shades of grey).

retrieval:  $U_{CD} = U_{GD} - U_{WD}$



## forward model: $U_{GD} - U_{AGD} = U_{CD} + U_{WD}$

Fig16A.pdf

**Figure 15.** Spectra  $F_y$  Ku-band Doppler measurements performed on (A) November 22nd and  $F_x$  (B) November 24th with the KuROS radar in the port-looking antenna configuration at  $\theta = 12^\circ$  incidence angle. The graphical conventions are identical for the two plots. The red dots and error bars represent the average and  $\pm 1$  standard deviation interval of south-north the platform-motion-corrected DV measurements along the different tracks. The magenta dots mark the mean values after correction of the  $U_{AGD}$  contribution. The magenta dotted line is the cosine fit to the corrected data. The blue and west-east Stokes drift components estimated midnight blue lines represent respectively the projection along the line-of-sight azimuth of the CARTHE current measurements and the  $U_{WD}$  vector computed from Trèfle the MLM-processed Trèfle buoy (solid data. The green line ), on November 22, from 12:00 to 14:00 UTC represents the sum of these two contributions, and modeled using WAVEWATCH III (red symbols) should agree with the magenta dotted line.

## retrieval: $U_{CD} = (U_{GD} + U_{AGD}) - U_{AGD} - U_{WD}$

**Figure 16.** Same as Fig. ??B Comparison of KuROS-derived Doppler velocity, corrected for November 24, the  $U_{AGD}$  and  $U_{WD}$  wave contributions, with in situ (CARTHE, SVP drifters and HF radar) current measurements.

Fig17A.pdf

Fig17B.pdf

Comparison of KuROS-derived Doppler velocity, in situ (CARTHE, SVP drifters and HF radar) current measurements, and theoretical wave contribution  $U_{GD}$  including an *ad-hoc* reduction of  $U_{WD}$  10%.

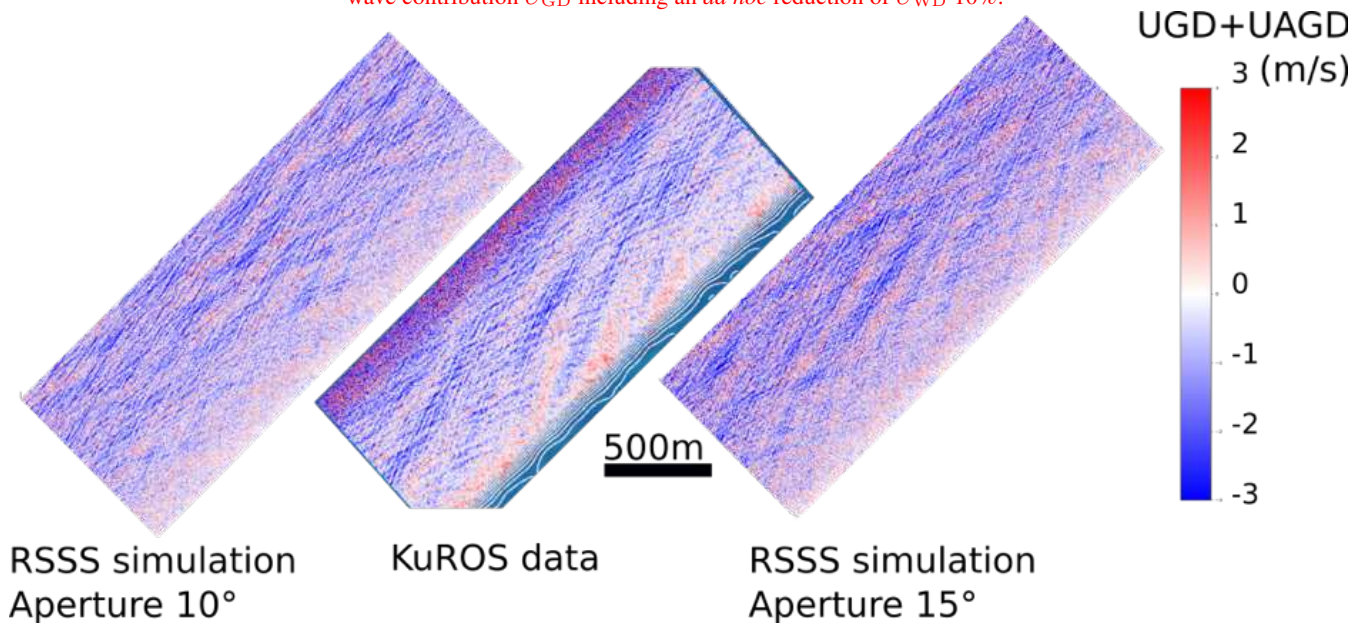


**Figure 17.** Qualitative validation of the R3S simulations of the radar imaging mechanism (?). Both the real data and simulation contain the geophysical modulation of velocities associated to surface velocities and slopes in the look direction (part of  $U_{GD}$ ) and aircraft velocities and slopes in the flight direction (part of  $U_{AGD}$ ). Note that the wave phases in the R3S simulation are random and cannot be expected to match those in the data or between the two simulations.

FIGURE\_NOTE\_ATTITUDE\_vert\_v2.pdf

**Figure A1.** (A) True pointing. The attitude drift changes the antenna footprint direction and shifts the ~~Doppler-DFS~~ centroid. Here  $(\gamma, \varphi)$  are the expected coordinate of the antenna gain ground projection while  $(\tilde{\gamma}, \tilde{\varphi})$  are the shifted version of these coordinates by the attitude mis-knowledge  $\tilde{\alpha}$  (adapted from Delouis ~~et al.~~). (B) Apparent pointing  $\varphi_a$  for the SKIM geometry. Examples of 2-way antenna gain  $G$  as a function of azimuth and distortions (exaggerated 100 times) induced by  $\sigma^0$  gradients on the power integrated by the radar in the azimuth direction across the antenna ~~pattern diagram~~ (grey curve). Three examples of ~~asymmetric~~ distortions are given: a sine function with  $\nu = \sin \theta / \sigma_\alpha$ , a 3-times faster varying sine function, and a linear trend. ~~If the azimuth  $\varphi$  correlates with the geometrical Doppler, then the distortion produces an apparent velocity error  $V_s$  which corresponds to.~~ Such distortions induce an apparent mispointing indicated by of the ~~vertical lines~~ beam  $\delta\varphi$ , and a correction to the geometrical line-of-sight relative velocity estimate.



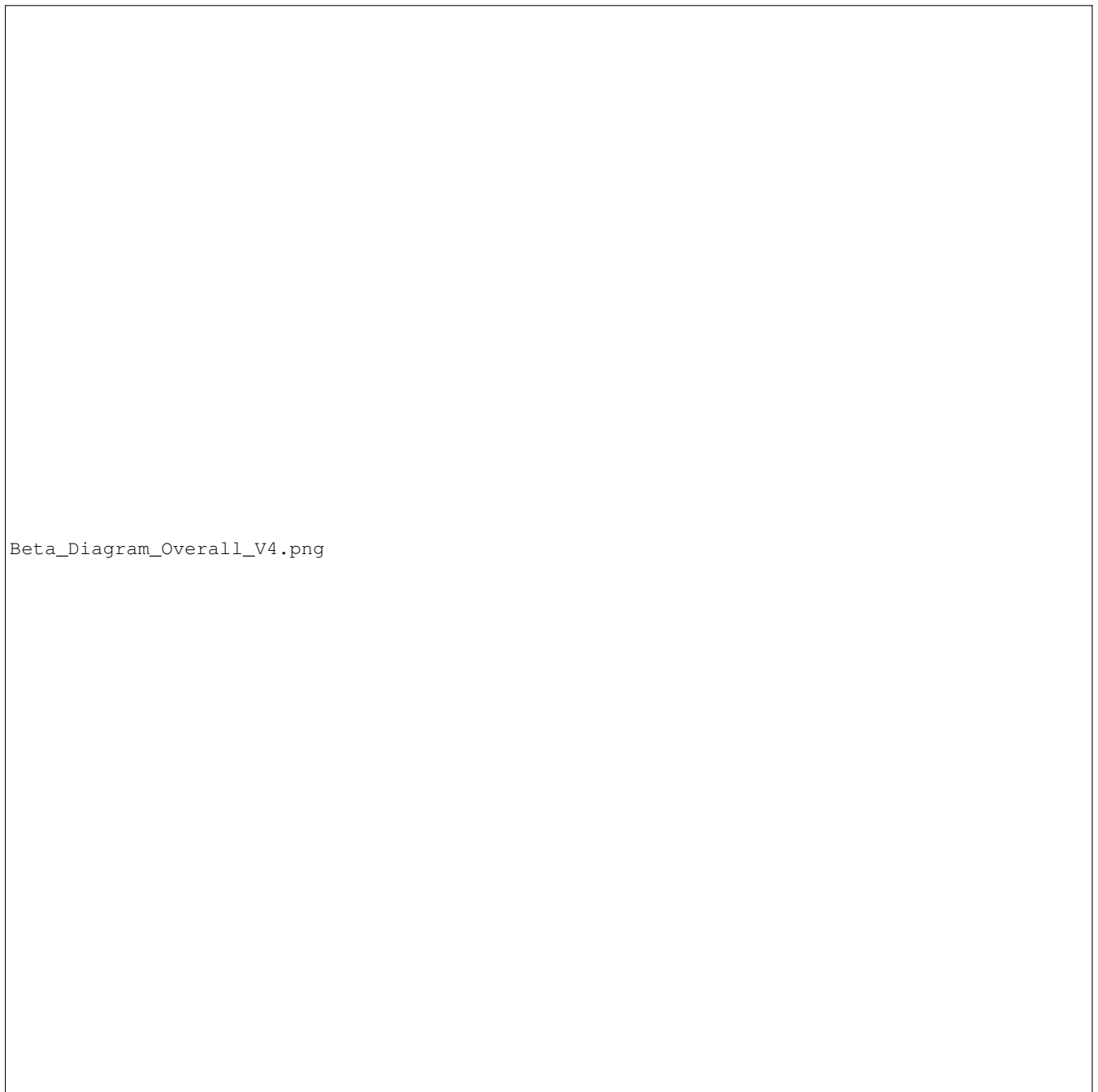


**Figure B1.** Reconstructed  $\alpha, \beta$  dependence of the 2-way KuROS antenna diagram. For each 30 s data segment, the [level-flight-constant altitude](#) values, for which the nadir is at  $\alpha = 0, \beta = 0$ , have been used as reference level to account for geophysical variations in nadir NRCS.



**Figure B2.** Reconstructed azimuth dependence of nadir return power for different incidence angles. For each incidence angle, the  $\alpha = 0$

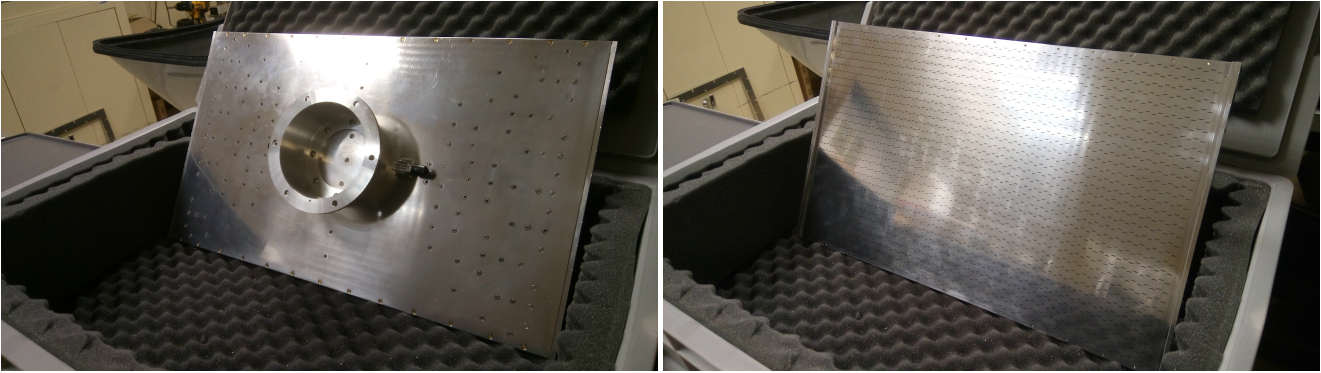


Figure C1. The back (on the left) and the front (on the right) of the antenna

Port2\_tilt.pdf

Port2\_hpbw.pdf

Figure C2. The back (on the left) Frequency dependence of the KaRADOC main lobe azimuth and elevation boresight angles (A) and the front half-power beamwidths (on the right B) of the antenna.

Coupe\_Azimuth.pdf

Coupe\_Elevation.pdf

Figure C3. Radiation pattern of the antenna for the frequency of KaRADOC radiation diagram at 33.7 GHz as a function of (A) azimuth at 2.09° elevation and (B) elevation at -0.05° azimuth.

*Author contributions.* All authors have contributed to the writing of the paper..

*Competing interests.* The authors declare that they have no conflict of interest.

1250 *Disclaimer.* The views and opinions expressed in this publication can in no way be taken to reflect the official opinion of the European Space Agency.

*Acknowledgements.* This study was supported by the KuROS4SKIM~~and~~ DRIFT4SKIM and IASCO contracts from the European Space Agency, made possible by the unflagging determination of Erik de Witte. The in situ measurements owe much to the dedication of the R/V Thalia crew. Airborne data ~~was~~ were obtained using the aircraft managed by Safire, the French facility for airborne research, an infrastructure of the French National Center for Scientific Research (CNRS), Météo-France and the French National Center for Space Studies (CNES). Many people at LOPS and OceanDataLab also contributed to the preparation, deployment and recovery of the instruments, including ~~Peter Sutherland~~, Mickael Accensi, Sylvain Herledan, Gilles Guitton, Lucile Gaultier, Michel Hamon, Olivier Péden, Stéphane Leizour, Pierre ~~Brannelee~~ Branellec. Many people at IETR are involved in the KaRADOC developments: Cécile Leconte, Mohamed Himdi, Paul ~~leroy~~ Leroy, Eric Pottier and especially Guy Grunfelder and Mor Diamo Lo who have made possible the measurement campaign during November, 2018.

1260 Operation of KuROS during the experiment would not have been possible without the dedication of Christophe Le Gac, Nicolas Pauwels and Christophe Dufour, from CNRS/LATMOS.

—  
—The required pointing knowledge is on the apparent pointing of the radar beam, which depends on the NRCS of the ocean surface  $\sigma^0(x, y, \theta, \varphi)$ . This NRCS is a property of the ocean surface that varies as a function of the horizontal position  $(x, y)$  due to the presence of waves, varying winds, currents, surfactants, sea ice and all the physical properties of the sea surface. The NRCS also varies with the viewing geometry, in particular, within a radar range gate, the azimuth change  $\varphi$  can be large enough to have a large impact on the Doppler. Both effects give apparent mispointings in elevation  $\epsilon$  and azimuth  $\delta$ ,

—  
that can also be written as an additional "Azimuth Gradient Doppler" velocity component  $U_{AGD}$ ,  
—